Resonant Microbeam High Resolution Vibrotactile Haptic Display

by

Daehan Wi

A Dissertation Presented in Partial Fulfillment
of the Requirements for the Degree
Doctor of Philosophy

Approved April 2019 by the
Graduate Supervisory Committee:

Angela Sodemann, Chair
Sangram Redkar
Troy McDaniel

ARIZONA STATE UNIVERSITY

May 2019

ABSTRACT

One type of assistive device for the blind has attempted to convert visual information into information that can be perceived through another sense, such as touch or hearing. A vibrotactile haptic display assistive device consists of an array of vibrating elements placed against the skin, allowing the blind individual to receive visual information through touch. However, these approaches have two significant technical challenges: large vibration element size and the number of microcontroller pins required for vibration control, both causing excessively low resolution of the device. Here, I propose and investigate a type of high-resolution vibrotactile haptic display which overcomes these challenges by utilizing a 'microbeam' as the vibrating element. These microbeams can then be actuated using only one microcontroller pin connected to a speaker or surface transducer. This approach could solve the low-resolution problem currently present in all haptic displays. In this paper, the results of an investigation into the manufacturability of such a device, simulation of the vibrational characteristics, and prototyping and experimental validation of the device concept are presented. The possible reasons of the frequency shift between the result of the forced or free response of beams and the frequency calculated based on a lumped mass approximation are investigated. It is found that one of the important reasons for the frequency shift is the size effect, the dependency of the elastic modulus on the size and kind of material. This size effect on A2 tool steel for Micro-Meso scale cantilever beams for the proposed system is investigated.

DEDICATION

This dissertation is dedicated to my beloved family. Without the love and support of my beloved wife, Sunyoung Kim, I could not have graduated with a Doctor of Philosophy degree. A special feeling of gratitude to my loving parents, In-gi Wi and Seonsook Lee whose words of encouragement and pray for all my life. My sister Hyeji Wi has always been on my side. I also dedicate this dissertation to all my church members who have praied for me throughout the process. I dedicate this work and give special thanks to my wonderful boy Rohan Wi for being there for me.

ACKNOWLEDGMENTS

I would like to express the deepest appreciation to my committee chair Assistant Professor, Dr. Angela Sodemann, who has the attitude and the substance of a genius and also kind and warm heart: she has continually and convincingly conveyed a spirit of adventure in regard to research, and an excitement in regard to teaching. Without her guidance and persistent help as my teacher and mentor, this dissertation would not have been possible.

I would like to thank one of my committee members, Associate Professor Dr. Sangram Redkar, whose advice regarding to the nonlinear vibrational model for my proposed system and device. In addition, a thank another committee member to Assistant Professor Dr. Troy McDaniel, who introduced me to a guidance for the experiment using haptic display device and tactile substitution system. Each of the members of my Dissertation Committee has provided me extensive personal and professional guidance and taught me a great deal about both scientific research and life in general.

I am especially indebted to Dr. Bradley Rogers, Associate Director for the Polytechnic school, who has accepted my program transfer request and has been supportive of my academic goals.

TABLE OF CONTENTS

LIST OF TABLES

LIST OF FIGURES

CHAPTER 1: INTRODUCTION

1.1 Research Overview

Impaired vision is a significant cause of reduced quality of life for millions of individuals. According to a UN report, around 15 percent of the world's population live with a disability, and about 25 percent of them are visually impaired ("Factsheet on Persons with Disabilities | United Nations Enable" n.d.; "Vision Impairment and Blindness" n.d.). Much research has been invested into the development of assistive methods and devices for the visually impaired, utilizing technology in many areas such as robotics, computer vision, neuroscience, haptics and artificial intelligence (Bhowmick and Hazarika 2017). The research for the visually impaired can be largely divided into four sections: (1) the Eye surgery to recover their sight or implant the artificial eye, (2) the invention of the living assistance device, which can help them to live independently, such as 'self-driving car' (3) the auditory substitution system, which is the conversion of visual information to sound, (4) the tactile substitution system, which is the conversion of visual information to touch. These four research types are shown in Fig. 1.

One of the popular assistive devices is using visual prosthesis including artificial retinal devices, called 'Bionic eye' (Ong and da Cruz 2012). There are several kinds of 'Bionic eye' devices, but the basic concept and mechanism is the same: (1) The image is captured by a camera, and then processed by a computer algorithm. (2) The image is converted to electrical signals. (3) The signals are transmitted to an implant in the retina. (4) Implanted electrodes stimulate the retina and send signals to the brain (Luo and da Cruz 2014). The visually impaired can really see using this method, but there are still several drawbacks. Electrode arrays stimulate more cells than the ones they are targeting,

so the maximum resolution is lower than 1500 pixels (approximately 38x38 pixels). It is also limited by the range of cell types in the retina, and totally-blind people cannot use this method. Moreover, considering that around 80 percent of persons with disabilities live in developing countries, the $150,000 cost of implant surgery cannot be a popular solution for the visually impaired.
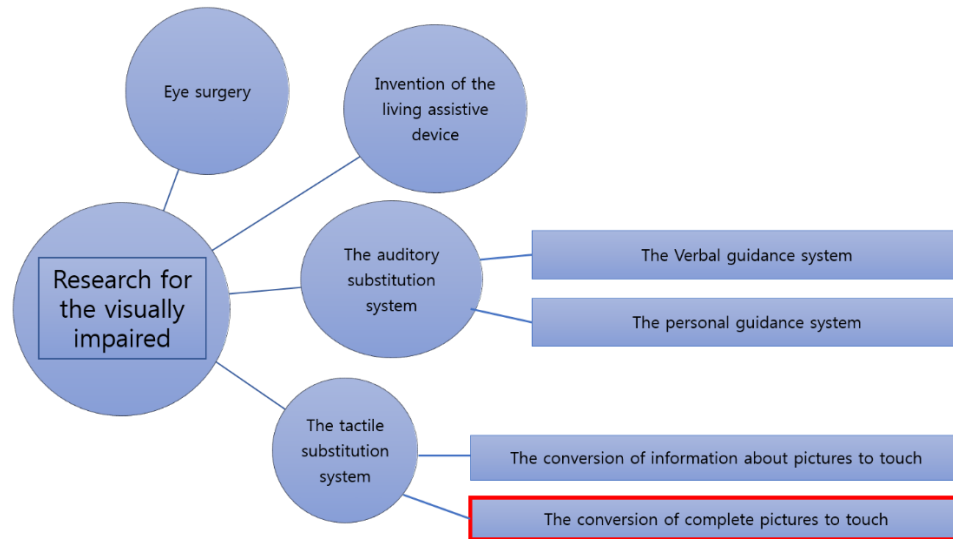
Fig. 1. The research types for the visually impaired and my research highlighted in red.

There is also a lot of research for the inventive device to make the life of visually impaired better and more convenient. Among them, the 'self-driving car' is the most popular one. It has a lot of state of the art technologies such as GPS and Laser radar systems to make a specific 3D map of the environment surrounding the 'car' and drive automatically (Hee Lee, Faundorfer, and Pollefeys 2013; Kim et al. 2013; Lee, Fraundorfer, and Pollefeys 2013). It has been tested for a long time, and has come close to commercialization, but has been delayed because of a fatal accident in 2016. The main problem of this kind of devices is that device can work as only secondary functions, and the blind cannot obtain the sight to do the self-directed activity.

The other assistive device is using an auditory display. This auditory substitution system can be classified into two large groups: verbal guidance systems and personal guidance systems. Verbal guidance systems take the approach of interpreting visual images and then reporting information about the images in words to the user, such as using GPS to assist blind people with navigation (Bourbakis and Kavraki 2001). This approach is similar to the traditional navigation system, which has been developed for a long time from the concept of the 'cane' and 'guide dog'. Nowadays, the visually impaired not only obtain the guidance information but also the information about objects around them (Du Buf et al. 2011). The information about pictures around them can be changed to a voice via their phone, and it has been recently developed with the help of innovations in artificial intelligence and smart phone technology. Today's smart phones have a lot of functions, especially computation, sensing and communications (Campbell and Choudhury 2012). Using AI in smart phones, the technology of giving the blind the information of what is happening in front of them has already been developed. It can read people's gender (Ng, Tay, and Goi 2015), facial expression (Lisetti and Schiano 2000) and text in front of the subject (Ezaki et al. 2005). It can make the lives of blind people more convenient, but it cannot provide 'vision' to them. Personal guidance systems attempt to provide 'vision' by directly converting pixel values of images to sound. J. M. Loomis et al (Loomis, Golledge, and Klatzky 1998) revealed that the personal guidance system using spatialized sound is more effective and faster than the verbal guidance system to navigate, because the blind can actively determine their own way. One of the recent personal guidance systems, 'The vOICe' (Auvray, Hanneton, and O'Regan 2007; Brown, Macpherson, and Ward 2011), which can theoretically have up to 10,000 pixels,

which could be higher resolution than 'Bionic' [14]. The problems, however, are that it has too much noise since visual images are changed to extremely complex sounds, and it takes quite a long time to decode the complex sound as meaningful vision and make it very clear.

The last part of the main research for the blind is the tactile substitution system. Even though the assistive devices explained previously have their own advantages, because of some serious problems such as high cost, noisiness and giving only limited information, the research using 'haptic displays' is taking center stage for the visually impaired. For a long time, using haptics like braille has been one of the very popular ways for them to communicate with the world. Given almost all visually impaired have a very sensitive sense of touch (Nari Kim et al. 2013), this area of research has a lot of potential to make progress.

1.2 Tactile Substitution System

Using 'haptic display' is one type of assistive device that has been extensively researched and shown initially good promise. A haptic display is a type of assistive device that converts a visual image into an image that can be perceived through touch.

The area of conversion of words to touch is the most traditional way of using 'haptics'. It can allow the blind to read by touching a haptic display such as braille. In the past, the visually impaired had just used this way to read a book, but the development of high level technology has allowed them to use many advanced products, even tablet PCs or laptop computers (Park, Jung, and Cho 2016; Ramstein 1996; Romero et al. 2011; Xu et al. 2011). 'Dot watch' ("Dot Incorporation" n.d.) and 'Blitab' ("BLITAB® – Feelings

Get Visible" n.d.) are two innovative products, which the visually impaired can use to receive any text information and use social networks by touching magnetically controlled braille keypads.

Recently, more complex haptic displays that can convert complete visual images into touch have made significant progress. This 'haptic display' area of research can be divided into two possible approaches: (1) conversion of information about pictures to touch, or (2) conversion of complete pictures to touch.

The first approach is conversion of information about pictures to touch. In this approach, an image is first processed by a computer to determine information about the image, such as distance to the nearest object, then vibration or other tactile signal is used to convey this information to the user (Ruspini, Kolarov, and Khatib 1997). Haptic face recognition (Kilgour, de Gelder, and Lederman 2004) is one example of this approach, including the approach of conveying emotion information using vibration motors (ur Réhman 2010),(McDaniel et al. 2014). Another example is the human-computer interface system that is studied by D. Hong et al (D'Angio 2012), and the blind can drive themselves using tactile gloves.

The second approach to haptic display is the conversion of complete pictures to touch. This approach has the significant benefit of potentially giving the user an effective replacement for vision. This area of research relies upon an assumption that the brain is capable of a type of plasticity known as 'sensory substitution', in which information provided via one sense can be interpreted by the brain as information from a different sense. Bach-y-Rita et al (P. Bach-y-Rita 1970; Bach-Y-Rita et al. 1969; Bach-y-rita 1983) have provided significant fundamental research to support this assumption. One

important device in this area is Brainport, a device which consists of a video camera mounted on a sunglass and an electrode array (Grant et al. 2016; Danilov and Tyler 2005; Nau, Bach, and Fisher 2013). The image captured by the camera is converted to a black and white image in software, and pixels from the camera are felt on the tongue via an electrode array (Paul Bach-y-Rita and W. Kercel 2003). However, due to the limit of tongue area and the size of electrodes, its resolution is not enough to obtain clear vision (max. 400 pixels). Fig. 2 illustrates the pixel resolution available with the BrainPort device. While using the device the blind also cannot speak to communicate or eat.

Fig. 2. Illustration of Brainport and its resolution.

While Brainport uses electrodes as the tactile device, other haptic displays use vibration motors. While the electrode approach is typically limited to placement on the tongue due to its wetness and, thus, high conductivity, vibration motor devices can be placed on any area of skin. This approach commonly uses vibration motors, camera, and a processing unit (Wacker et al. 2016),(Dakopoulos and Bourbakis 2009). The image captured by the camera is processed in a processing unit into a vibration level for an array of vibration motors corresponding to the image.

This approach, however, has the same two drawbacks as the electrode approach: low resolution and the requirement to have one I/O pin per vibrating element. The low resolution is due to the limit of our body area, the size of the vibration motors, and the

number of single I/O pins on the microcontroller (Borst and Cavanaugh 2004). Each vibration motor requires one I/O pin and pulse-width modulation (PWM) signal from the microcontroller to control its vibration amplitude and frequency, and a typical microcontroller has about 16 PWM generators. Given this, in order to achieve high resolution such as 640x480, a very large number of vibration motors and I/O pins will be needed. All of the vibration motor arrays found in the literature for this study reported (Borst and Cavanaugh 2004; Mann et al. 2011) using less than 200 vibration motors, and most used less than 20 (Dakopoulos, Boddhu, and Bourbakis 2007; Dakopoulos and Bourbakis 2010). Fig. 3 illustrates the resolution achieved by one of the higher-resolution vibration motor studies reviewed by this study.
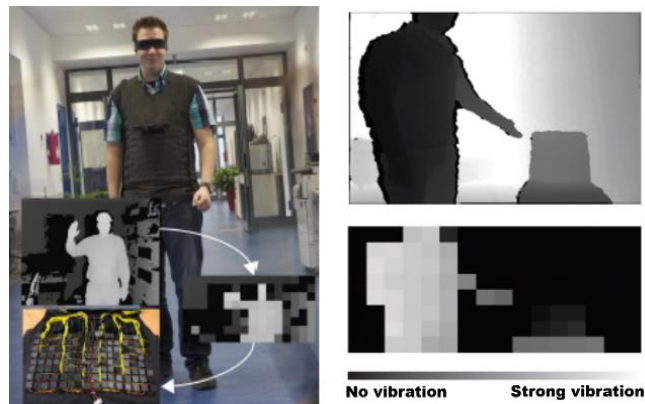
Fig. 3. Illustration of Vibrovision and its resolution (Wacker et al. 2016).

1.3 Microbeam Vibrotactile Array Approach for the Tactile Substitution System

The current two approaches of tactile substitution system to convert complete pictures to touch have a strong advantage in that the complete in-formation contained in an image is conveyed to the brain of the user. However, all existing devices which take this approach have the major disadvantage of low resolution caused by the limited area of tongue or the one I/O pin per vibrating element problem.

Fig. 4 shows the effect of image resolution. The resolution of BrainPort is a little better than the 4th picture showing 256 pixels, and it is noticed that it is definitely not enough for the visually impaired to live independently in daily life. Using the vibration motor method has even lower resolution than the BrainPort. Because of the low-resolution problem, some small objects could not be recognized by those approaches. Moreover, some large objects in only static state could be recognized, which means they are not an appropriate method to an environment in which people should make their decision fast such as driving.
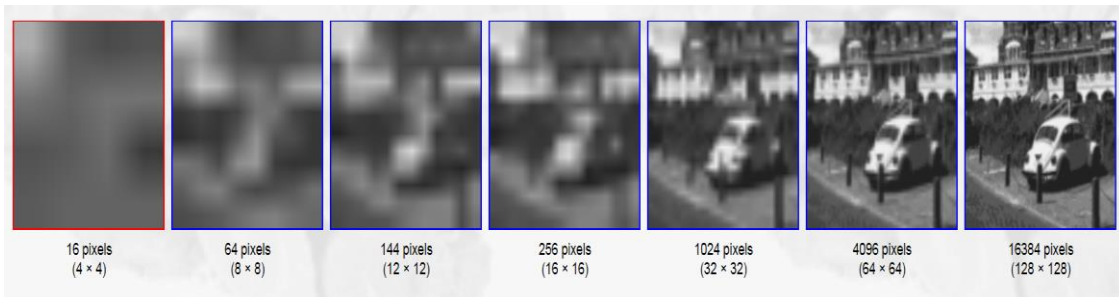
Fig. 4. The effect of image resolution ("Bionic Vision for the Blind - Retinal Implant? Eye Surgery?" n.d.).

To solve this problem and make a high-resolution vibratory display such as 640x480 for the visually impaired, an array of micro-cantilever beams which can be actuated using the concept of resonance has been proposed (D. Wi, Sodemann, and Chicci 2017; Daehan Wi and Sodemann 2018). Resonance is a phenomenon in which an external oscillating force drives a system to oscillate with greater amplitude at a specific frequency, termed its 'resonant frequency'. In the proposed system, each beam is manufactured with a different length and/or cross-sectional area, so that each beam has a unique natural frequency. The beam array can then be actuated by a speaker or surface transducer connected to a single analog pin of a microcontroller.

Previous research has investigated the use of microbeams in tactile device applications, although this research does not use resonance for actuation of the beams but requires an independent voltage signal to be applied to the base of each beam. Konyo et al (Konyo, Tadokoro, and Takamori 2000; Konyo et al. 2005) have proposed a ciliary device using soft high polymer gel actuators, ICPF (Ionic Conducting Polymer gel Film). ICPF is a composite of a PFS (PerFluoroSulfonic acid) membrane and thin platinum surface layers, which makes a bending motion. This device has been used to generate various distributed stimuli to human sense receptors, including vibration causing a tapping against the skin, and static bending causing a pressure sensation against the skin. However, the device has not been used to convey complete pictures as touch.

CHAPTER 2: RESONANT MICROBEAM VIBROTACTILE ARRAY CONCEPT

A new approach for the vibration array component of a visual system that can achieve a much higher resolution by using the concept of resonance is proposed. Fig. 5 shows the amplitude of a responding vibratory system as it is actuated by the vibration of another system. A high amplitude peak is seen at the resonant frequency of the system. The amplitude of the peak depends upon the damping ratio, with a larger peak occurring in materials with lower damping ratios.
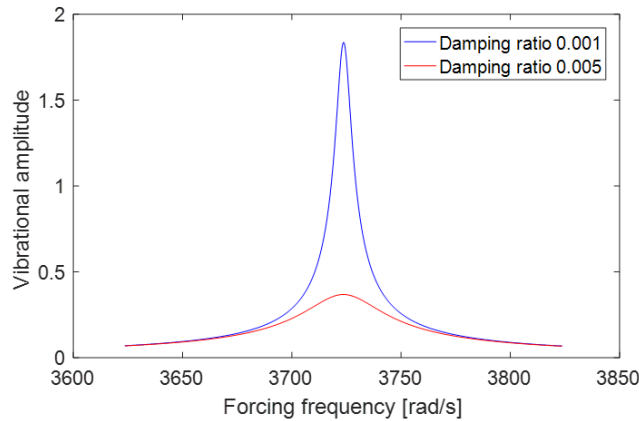
Fig. 5. Amplitude difference depending on damping ratio.

In the proposed system, each micro-cantilever beam is designed to have a unique resonant frequency. The resonant frequency of a micro-cantilever beam depends upon length and cross-sectional area. So, an array of beams all with unique natural frequencies can be made by varying the length and cross-sectional area of each beam.

In the proposed system, a speaker or surface transducer is placed near to or in contact with a side surface of the beam array. The speaker or surface transducer is connected to an amplifier, which is connected to a microcontroller. When the frequency of the sound or vibration coming from the speaker or surface transducer is equal to the resonant frequency of a beam, that beam will vibrate with a large amplitude, while other

beams will vibrate with a much smaller amplitude. Since many frequencies can be

produced simultaneously by a single speaker or surface transducer, any combination of

beams can be made to vibrate at specified amplitudes with a single speaker or surface

transducer. Fig. 6 illustrates how one speaker or surface transducer can be made to

actuate multiple beams simultaneously by producing a single wave that is the sum of

many individual waves.

$$w(t) = 200 \sin(1000t) + 200 \sin(2000t)$$
$$+ 200 \sin(3000t) + 100 \sin(4000t) + 100\sin(5000t)$$
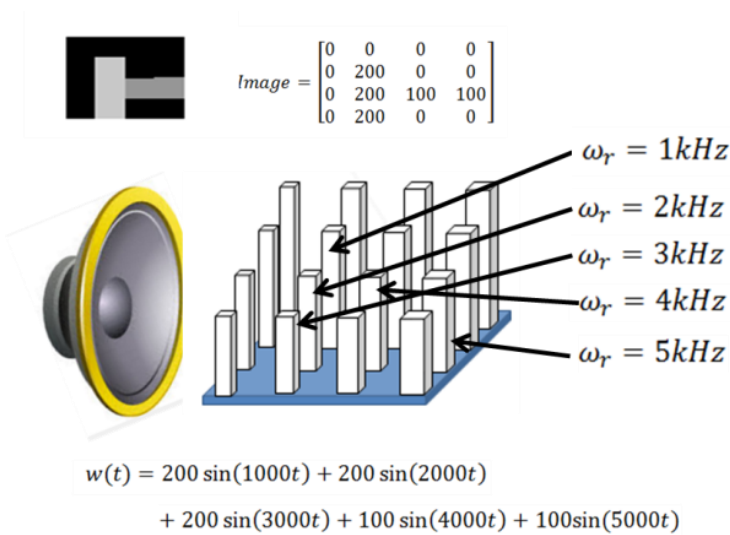
Fig. 6. A speaker produces a wave *w(t)* equal to the sum of individual amplitudes and
frequencies for each beam. In this example, five beams are being actuated; three beams
at an amplitude of 200 and two beams at an amplitude of 100.

In order to use the proposed beam array to represent an image, a color image will

be first converted to grayscale at a resolution equal to the resolution of the beam array.

Then, each pixel location corresponds to a wave frequency equal to the resonant

frequency of the beam that is in the corresponding location. Each pixel value, represented

as a single number between 0 and 255 (for 8-bit depth), determines the amplitude of the

wave. After all individual waves, one wave for each pixel, are defined, the waves are

superposed, and the resultant wave is played by the speaker or surface transducer,

resulting in a vibration of the beam array which corresponds to the original grayscale

image. Finally, the user perceives the vibration of the beam array, and it is converted to an image within their brain. Fig. 7 illustrates this process.
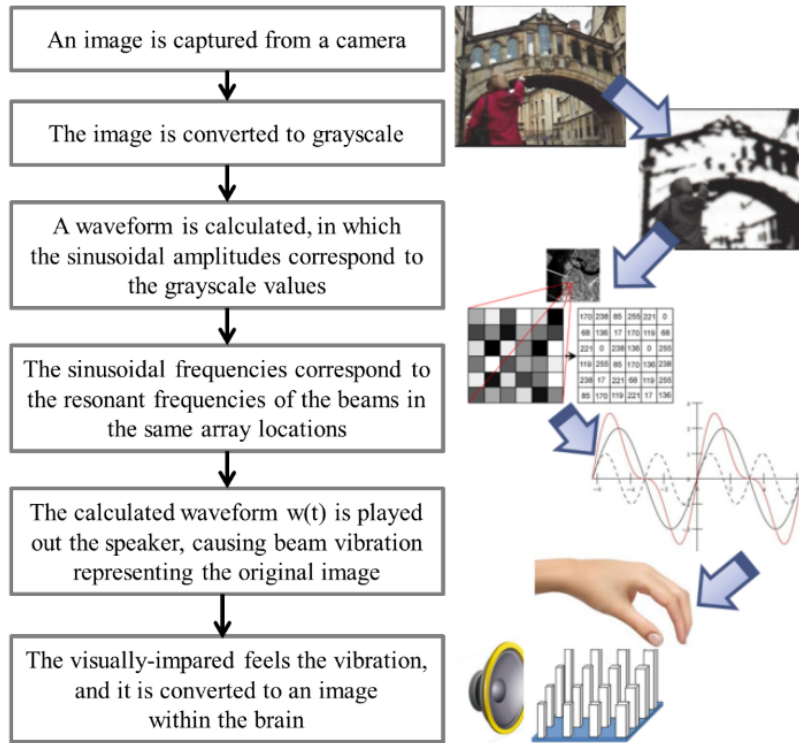
Fig. 7. Illustration of the process of the proposed vibrotactile display.

Utilizing recent advances in micro scale manufacturing, it is possible to produce a beam array with small cross-sectional dimension of around 100μm. Manufacturing processes can also allow some control over the material properties (modulus of elasticity and material density), as well as the geometric properties (cross-sectional area, length, and bending moment of inertia). Due to the mechanical simplicity of each vibratory element and by recent advances in manufacturing processes, a large number of micro-beams can be placed in a small space, thus allowing for a high resolution of the vibratory display. With current manufacturing technologies, each beam can be produced with a width/thickness dimension around 0.1mm. Allowing for a space between beams equal to the beam width, a 640x480 resolution can be achieved in a space of 12.8x9.6 cm, a size

which is easily portable and able to be placed against the forearm, back, or other generally unobtrusive segment of the skin. A resolution of 400x400 beams can be placed within the palm of the hand.

      In this study, the goal is to proof the concept of the proposed system, analytically evaluate the feasibility, prototype the system, experimentally evaluate the functionality of a vibration device of the type proposed, and produce a preliminary experimental validation of the effectiveness of the system for its proposed use. In chapter 3 of this document, an analysis of single-beam vibration using the lumped-mass approximation and analysis of beam vibration of an array of beams as in the proposed system are proposed. Chapter 4 presents an analysis of manufacturing considerations and the results of prototyping efforts. Chapter 5 gives the experimental setup and results of both free and forced vibration experiments on the prototype devices, and chapter 6 gives an overview of Ansys simulations of the device vibrations. Chapter 7 introduces the proposed experimentation for evaluating the use of the device. Chapter 8 presents the reason of the resonant frequency difference between the one calculated based on the lumped mass approximation and the one from the free or forced response experiment, and the size effect on stiffness, elastic modulus and damping ratio. Chapter 9 gives conclusions and discussion, including a timeline for completion of the research.

CHAPTER 3: VIBRATION ANALYSIS

  Much previous research has been undertaken to understand micro-scale vibration effects on beams, such as the size effect. Other higher-order continuum mechanics theories such as the strain gradient and modified couple stress have been investigated, which introduce additional material length scale parameters in order to analyze the nonlinear behavior of microscale continuous elements (Ghayesh, Farokhi, and Amabili 2014), (Farokhi, Ghayesh, and Hussain 2016), (Delgado-Velázquez 2007). However, it has been shown that the size effect and other non-linear effects of microbeam vibration is intrinsic to certain materials with non-homogenous microstructures by many experimental results (Kong et al. 2009), (Farokhi and Ghayesh 2015). The largest size of beams that have shown these nonlinear effects is 170μm (Barari et al. 2011), (Akgöz and Civalek 2013), (Ghayesh and Farokhi 2015), (Lam et al. 2003). Compared to the smallest beam size of my model, which is 330μm up to the 2nd metal prototype, it is estimated that the beams in the proposed model are much less subject to the size effect and other nonlinearities of microscale elements. Moreover, the beam design in the proposed method is homogenous. For these reasons, the conventional classical couple stress elasticity theory is used for this research. Here, the equations governing the functionality of such a device is developed.

3.1 Vibration Analysis for Single Beam Model

  In order to design a beam array of the type proposed, many parameters and design variables must be considered: the dimensions and cross-sectional shape of each beam in the array, beam material, sound amplitude and frequency range, minimum

frequency distance between beams, number of beams controlled by a single speaker or surface transducer, minimum beam size for human perception of vibration, and others. To determine these parameters, the natural frequency and amplitude of each beam are the most important considerations. This is because many beams having unique natural frequency is needed for this proposed system, and bigger amplitude of beam vibration is needed to make people perceive the beam vibration easily.

The governing equation of a cantilever beam as I shown in Eq. (1), where E is the modulus of elasticity of the beam material, I is the bending moment of inertia, m is mass, L is length of the beam, x is the distance from the origin in x direction (length direction), y is the deflection of the beam in the z direction, and t is a time variable ("Structural Dynamics - Beams" n.d.).

$$-EI\frac{\partial^4 y}{\partial x^4} = \frac{m}{L}\frac{\partial^2 y}{\partial t^2} \qquad (1)$$

Then, the natural frequency ω_n of a fixed-free beam is shown in Eq. (2), where βn is the mode number.

$$\omega_n = \beta_n^2 \sqrt{\frac{EI}{m/L}} \qquad (2)$$

The highest-amplitude and lowest-frequency mode will be the first mode. This mode is the most interesting, since human ability to perceive vibration is greater at lower frequencies and the higher amplitudes via the conjunction of four channel of tactile mechanoreceptors (Bolanowski Jr et al. 1988). In the proposed system, the user should perceive beam vibrations which involve motion of the tip of the beam moving past the user's skin to obtain the visual information. This means a combination of dynamic and static touches will be applied in the system. In general, the perceivable frequency range is

known from 10 Hz to 500 Hz. Even though there have been several researches on the

non-linearity of perceptual characteristics in high frequency amplitude-modulated

vibration such as higher than 1 kHz, which multi vibrators are used to excite people skin

in the research, this could be used in multiple beams vibration to increase the efficiency

of the proposed system, not in single beam vibration. Since the motion of single beam

vibration is dominated by the first mode, it is expected that this mode will be dominant in

the user's perception. The first mode of vibration for the cantilever beam is given in Eq.

(3).

$$\omega_1 = \left(\frac{1.8751}{L}\right)^2 \sqrt{\frac{EI}{m/L}} \qquad (3)$$

The area moment of inertia, I, is different depending on the shape of cross-

sectional area. Fig. 8 shows the cross-sectional shape of ellipse and rectangular. For

ellipse, the area moment inertia along x direction, I_x, can be expressed as $\frac{\pi ab^3}{4}$, and the

one along y direction, I_y, can be expressed as $\frac{\pi ba^3}{4}$, where a is the radius along x

direction, and b is the radius along y direction. For rectangular, the area moment inertia

along x direction, I_x, can be expressed as $\frac{bh^3}{12}$, and the one along y direction, I_y, can be

expressed as $\frac{b^3h}{12}$, where b is the dimension along x direction, and h is the dimension

along y direction. Along the direction, I can be different even in the same object, and this

is very important since the frequency can also be different. In the result, I can be a

constant only for a symmetrical cross-sectional shape such as circle.
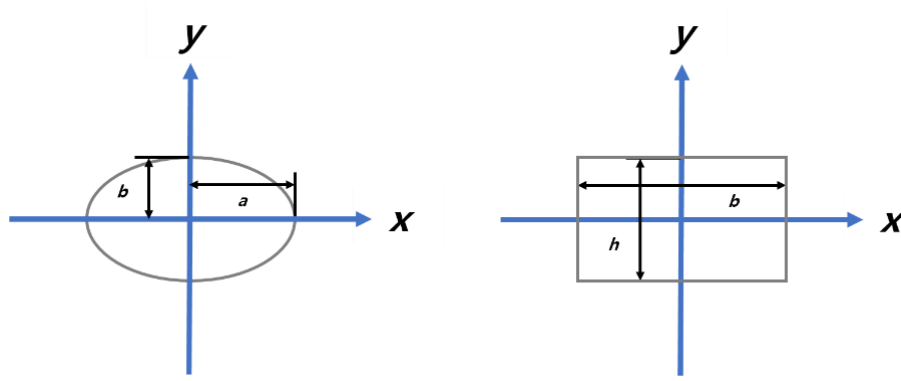
Fig. 8. The area moment of inertia of ellipse and rectangular shape.

In the proposed system, the beam array model can be considered as a fixed-free beam subjected to base excitation. In this case, the governing equation is as shown in Eq. (4) (Sun et al. 2013), where w is the displacement of the beam base and y is the displacement of a point x on the beam at time t. Since the size of the beams are at the larger end of the scale considered to be 'micro-beams', it is expected that nonlinear microscale effects will not be dominant in this case and are left out here.

$$EI\frac{\partial^4 y}{\partial x^4} + \rho\frac{\partial^2 y}{\partial t^2} = -\rho\frac{\partial^2 w}{\partial t^2} \qquad (4)$$

The relative displacement, $Y(x,\omega)$, in the steady-state solution is then as shown in Eq. (7) and Eq. (8), where $Y_n(X)$ is independent of position and $T_n(t)$ is independent of time.

$$Z_n(\omega) = \int_{-\infty}^{\infty} T_n(t)\, exp(-j\omega t)\, dt \qquad (5)$$

$$\ddot{W}(\omega) = \int_{-\infty}^{\infty} \ddot{w}(t)\, exp(-j\omega t)\, dt \qquad (6)$$

$$Y(x,\omega) = \sum_{n=1}^{m} Y_n(X)Z_n(\omega) \qquad (7)$$

$$Y(x,\omega) = \ddot{W}(\omega)\sum_{n=1}^{m}\frac{-F_n Y_n(X)}{[(\omega_n^2 - \omega^2) + j2\zeta_n \omega_n \omega]} \qquad (8)$$

The frequency response function relating the relative displacement to the base acceleration, then, is as shown in Eq. (9).

1 7

$$H_{rd}(x, \omega) = \frac{Y(x,\omega)}{\ddot{W}(\omega)} = \sum_{n=1}^{m} \frac{-F_n Y_n(X)}{[(\omega_n^2 - \omega^2) + j2\zeta_n \omega_n \omega]} \tag{9}$$

In order to narrow down the possible beam design options, a lumped-mass model can be used for initial analysis of beam vibration. In the lumped-mass model, the cantilever beam can be considered as a massless beam and a tip mass, as shown in Fig. 9.
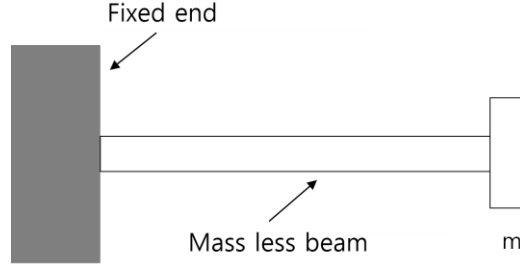
Fig. 9. The lumped-mass model of a cantilever beam.

If the material contains damping that is not negligible, then the resonant frequency ω_r of the beam is as shown in Eq. (10).

$$\omega_r = \omega_n \sqrt{1 - 2\zeta^2} \tag{10}$$

The amplitude of vibration depends upon the beam 'equivalent mass' and 'equivalent stiffness'. Rayleigh's method is used to calculate the equivalent mass ("Effective Mass - Serendipedia" n.d.). The equivalent mass of the beam m_{eq} depends only upon the actual beam mass m_b as in Eq. (11).

$$m_{eq} = \frac{33}{140} m_b \tag{11}$$

The equivalent stiffness k depends upon both the material of the beam by way of the modulus of elasticity E, and the beam dimensions by way of the moment of inertial I and the beam length L, as shown in Eq. (12).

$$k = \frac{3EI}{L^3} \tag{12}$$

As a result, the first mode of vibration for the cantilever beam in the lumped-

mass model can be described, as shown in Eq. (13).

$$\omega_1 = \sqrt{\frac{K}{m_{eq}}} = \sqrt{\frac{3EI}{m_{eq}L^3}} \tag{13}$$

Eq. (3) is the equation for the natural frequency of a cantilever beam derived

from the eigen value method. Comparing Eq. (3) to the lumped-mass method in Eq. (13),

there is only a constant number difference between them, which is $(1.8751)^2 \approx \sqrt{\frac{3*140}{33}}$.

Therefore, if the correction coefficient 0.985555741 is multiplied by the resonant

frequency calculated by the lumped-mass model, the resonant frequency from the

eigenvalue method can be calculated.

The amplitude of vibration of the beam shown in Eq. (14) and Eq. (15) can be

found from the steady-state solution to a forced harmonic oscillator, where F and ω are

the amplitude and frequency of the force applied due to the sound.

$$A = \frac{F}{mZ\omega} \tag{14}$$

$$Z = \sqrt{(2\omega_n\zeta)^2 + \frac{(\omega_n^2-\omega^2)^2}{\omega^2}} \tag{15}$$

3.2 Vibration Analysis for Multi Degree of Freedom Base Excitation Model

The analysis presented in Section 3-1 considers only a single beam in isolation.

However, the proposed system consists of an array of beams on a single base, and

therefore the interaction of the vibration of the beams should be considered. Based on this

single beam vibration model using a lumped-mass method, multi beams vibration model

is developed for the proposed system. Later experiments performed on prototypes of this

system suggest that it may be beneficial to attach a compliant material such as silicone

rubber to the tips of the beams in order to aid user perception of the vibration. Therefore, this analysis considers both the beams and the compliant material attached to beam tips. If two metal beams and two silicone rubber beams are considered, the vibration model is described like below, as shown in Fig. 10.
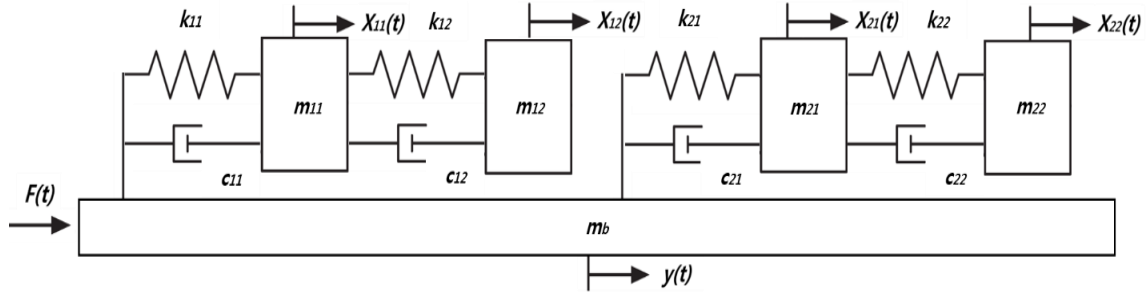
Fig. 10. The vibration model of 2 metal beams and 2 silicone rubber beams.

This model can be represented by general equations as shown in Eq. (16) ~ (20), where m_{11} and m_{21} are the masses of the 1st and 2nd metal beam, m_{12} and m_{22} are the masses of the 1st and 2nd silicone rubber beams, k_{11} and k_{21} are the spring constants of the 1st and 2nd metal beam, k_{12} and k_{22} are the spring constants of the 1st and 2nd silicone rubber beams, c_{11} and c_{21} are the damping coefficients of the 1st and 2nd metal beam, c_{12} and c_{22} are the damping coefficients of the 1st and 2nd silicone rubber beams. X_{11} and X_{21} are the displacements of the 1st and 2nd metal beam, and X_{12} and X_{22} are the displacements of the 1st and 2nd silicone rubber beams. $\dot{X}_{11}$, $\dot{X}_{21}$, $\dot{X}_{12}$, and $\dot{X}_{22}$ are the first derivations of X_{11}, X_{21}, X_{12}, and X_{22}. $\ddot{X}_{11}$, $\ddot{X}_{21}$, $\ddot{X}_{12}$, and $\ddot{X}_{22}$ are the second derivations of X_{11}, X_{21}, X_{12}, and X_{22}. $F(t)$ is the forcing function coming from a speaker or surface transducer, $y(t)$ is the displacement of a beam base, and m_b is the mass of the beam base.

$$m_{11}\ddot{X}_{11}(t) = k_{12}(X_{12}(t) - X_{11}(t)) + k_{11}(y(t) - X_{11}(t)) + c_{12}(\dot{X}_{12}(t) - \dot{X}_{11}(t)) +$$

$$c_{11}(\dot{y}(t) - \dot{X}_{11}(t)) \tag{16}$$

$$m_{12}\ddot{X}_{12}(t) = k_{12}(X_{11}(t) - X_{12}(t)) + c_{12}(\dot{X}_{11}(t) - \dot{X}_{12}(t)) \tag{17}$$

$$m_{21}\ddot{X}_{21}(t) = k_{22}(X_{22}(t) - X_{21}(t)) + k_{21}(y(t) - X_{21}(t)) + c_{22}(\dot{X}_{22}(t) - \dot{X}_{21}(t)) +$$

$$c_{21}(\dot{y}(t) - \dot{X}_{21}(t)) \tag{18}$$

$$m_{22}\ddot{X}_{22}(t) = k_{22}(X_{21}(t) - X_{22}(t)) + c_{22}(\dot{X}_{21}(t) - \dot{X}_{22}(t)) \tag{19}$$

$$m_b\ddot{y}(t) = F(t) + k_{11}(X_{11}(t) - y(t)) + k_{21}(X_{21}(t) - y(t)) + c_{11}(\dot{X}_{11}(t) - \dot{y}(t)) +$$

$$c_{21}(\dot{X}_{21}(t) - \dot{y}(t)) \tag{20}$$

These equations above can be changed to Eq. (21) ~ (25) by applying Laplace transform, and all the initial condition are assumed to be zero due to the startup conditions that are no initial movement and no initial velocity.

$$m_{11}s^2X_{11}(s) = k_{12}(X_{12}(s) - X_{11}(s)) + k_{11}(y(s) - X_{11}(s)) + c_{12}(sX_{12}(s) -$$

$$sX_{11}(s)) + c_{11}(sy(s) - sX_{11}(s)) \tag{21}$$

$$m_{12}s^2X_{12}(s) = k_{12}(X_{11}(s) - X_{12}(s)) + c_{12}(sX_{11}(s) - sX_{12}(s)) \tag{22}$$

$$m_{21}s^2X_{21}(s) = k_{22}(X_{22}(s) - X_{21}(s)) + k_{21}(y(s) - X_{21}(s)) + c_{22}(sX_{22}(s) -$$

$$sX_{21}(s)) + c_{21}(sy(s) - sX_{21}(s)) \tag{23}$$

$$m_{22}s^2X_{22}(s) = k_{22}(X_{21}(s) - X_{22}(s)) + c_{22}(sX_{21}(s) - sX_{22}(s)) \tag{24}$$

$$m_bs^2y(s) = F(s) + k_{11}(X_{11}(s) - y(s)) + k_{21}(X_{21}(s) - y(s)) + c_{11}(sX_{11}(s) -$$

$$sy(s)) + c_{21}(sX_{21}(s) - sy(s)) \tag{25}$$

Eq. (21) ~ (25) can be re-organized by displacement, as shown in Eq. (26) ~ (30).

$$X_{11}(s)[m_{11}s^2 + k_{12} + k_{11} + c_{12}s + c_{11}s] = X_{12}(s)[k_{12} + c_{12}s] + y(s)[k_{11} + c_{11}s] \tag{26}$$

$$X_{12}(s)[m_{12}s^2 + k_{12} + c_{12}s] = X_{11}(s)[k_{12} + c_{12}s] \tag{27}$$

$$X_{21}(s)[m_{21}s^2 + k_{22} + k_{21} + c_{22}s + c_{21}s] = X_{22}(s)[k_{22} + c_{22}s] + y(s)[k_{21} + c_{21}s]$$

$$(28)$$

$$X_{22}(s)[m_{22}s^2 + k_{22} + c_{22}s] = X_{21}(s)[k_{22} + c_{22}s] \qquad (29)$$

$$y(s)[m_b s^2 + k_{11} + k_{21} + c_{11}s + c_{21}s] = F(s) + X_{11}(s)[k_{11} + c_{11}s] + X_{21}(s)[k_{21} +$$

$$c_{21}s] \qquad (30)$$

To simplify equations, let $G1 = m_{12}s^2 + k_{12} + c_{12}s$, $G2 = k_{12} + c_{12}s$, $G3 =$

$m_{11}s^2 + k_{12} + k_{11} + c_{12}s + c_{11}s$, $G4 = k_{11} + c_{11}s$, $G5 = m_{22}s^2 + k_{22} + c_{22}s$, $G6 =$

$k_{22} + c_{22}s$, $G7 = m_b s^2 + k_{11} + k_{21} + c_{11}s + c_{21}s$, $G8 = k_{21} + c_{21}s$, $G9 = m_b s^2 +$

$k_{11} + k_{21} + c_{11}s + c_{21}s$

Then, Eq. (26) ~ (30) can be expressed, as shown in Eq. (31) ~ (35).

$$X_{11}(s)G3 = X_{12}(s)G2 + y(s)G4 \qquad (31)$$

$$X_{12}(s)G1 = X_{11}(s)G2 \qquad (32)$$

$$X_{21}(s)G7 = X_{22}(s)G6 + y(s)G8 \qquad (33)$$

$$X_{22}(s)G5 = X_{21}(s)G6 \qquad (34)$$

$$y(s)G9 = F(s) + X_{11}(s)G4 + X_{21}(s)G8 \qquad (35)$$

Eq. (32) can be expressed for X_{11} or X_{12}, as shown in Eq. (36).

$$X_{11}(s) = X_{12}(s)\frac{G1}{G2} \text{ or } X_{12}(s) = X_{11}(s)\frac{G2}{G1} \qquad (36)$$

Eq. (34) can be expressed for X_{21} or X_{22}, as shown in Eq. (37).

$$X_{21}(s) = X_{22}(s)\frac{G5}{G6} \text{ or } X_{22}(s) = X_{21}(s)\frac{G6}{G5} \qquad (37)$$

Eq. (36) is substituted into Eq. (31), and the equation can be expressed as the

relationship of the displacement of 1st metal beam and the displacement of beam base, as

shown in Eq. (38).

$$X_{11}(s) = \left[\frac{G4}{G3-\frac{G2G2}{G1}}\right] y(s) \qquad (38)$$

Eq. (37) is substituted into Eq. (33), and the equation can be expressed as the relationship of the displacement of 2nd metal beam and the displacement of beam base, as shown in Eq. (39).

$$X_{21}(s) = \left[\frac{G8}{G7-\frac{G6G6}{G5}}\right] y(s) \qquad (39)$$

To obtain the relationship between the displacement of 1st silicone rubber beam and the displacement of beam base, substituting Eq. (36) into Eq. (31), and the equation is described as shown in Eq. (40).

$$X_{12}(s) = \left[\frac{G4}{\frac{G1G3}{G2}-G2}\right] y(s) \qquad (40)$$

The relationship between the displacement of 2nd silicone rubber beam and the displacement of beam base can be obtained by substituting Eq. (36) into Eq. (31), as shown in Eq. (41).

$$X_{22}(s) = \left[\frac{G8}{\frac{G7G5}{G6}-G6}\right] y(s) \qquad (41)$$

By substituting Eq. (38) and (39) into Eq. (35), the relationship between the displacement of beam base and the force function can be obtained, as shown in Eq. (42).

Let A be equal to $\left[G9 - \frac{G4G4}{G3-\frac{G2G2}{G1}} - \frac{G8G8}{G7-\frac{G6G6}{G5}}\right]$.

$$F(s) = \left[G9 - \frac{G4G4}{G3-\frac{G2G2}{G1}} - \frac{G8G8}{G7-\frac{G6G6}{G5}}\right] y(s) = Ay(s) \qquad (42)$$

Eq. (42) is substituted into Eq. (38), and then finally the relationship between the displacement of 1st metal beam and the force function can be obtained, as shown in Eq.

(43).

$$X_{11}(s) = \left[\frac{G4}{G3 - \frac{G2G2}{G1}}\right]\frac{F(s)}{A} \tag{43}$$

The relationship between the displacement of 2nd metal beam and the force function can be also obtained by substituting Eq. (42) into Eq. (39), as shown in Eq. (44).

$$X_{21}(s) = \left[\frac{G8}{G7 - \frac{G6G6}{G5}}\right]\frac{F(s)}{A} \tag{44}$$

The relationship between the displacement of 1st silicone rubber beam and the force function can be also obtained by substituting Eq. (42) into Eq. (40), as shown in Eq. (45).

$$X_{12}(s) = \left[\frac{G4}{\frac{G1G3}{G2} - G2}\right]\frac{F(s)}{A} \tag{45}$$

The relationship between the displacement of 2nd silicone rubber beam and the force function can be also obtained by substituting Eq. (42) into Eq. (41), as shown in Eq. (46).

$$X_{21}(s) = \left[\frac{G8}{\frac{G7G5}{G6} - G6}\right]\frac{F(s)}{A} \tag{46}$$

Now the relationship of each metal beam or silicone rubber beam and the force function coming from a speaker or a surface transducer is known. These equations can be used to design dimensions for prototype beam arrays that are predicted to work as intended. So, now it can be moved on to the prototyping stage.

CHAPTER 4: MANUFACTURING AND PROTOTYPING

This Chapter first presents an analysis of potential manufacturing methods for the proposed device, then gives a summary of the prototyping efforts made to date. The manufacturing method analysis consists of an evaluation of the potential resolutions possible with different potential manufacturing methods, considering both the limitations of the manufacturing methods and the requirements of the proposed device. The prototyping efforts are divided into two Sections: Prototyping using plastic materials and prototyping using metal materials. A summary of the outcome of each prototyping attempt is given.

4.1 Manufacturing Analysis

There are many parameters that must be considered for the proposed method. To make proper prototypes and to conduct experiments with them, important parameters must be analyzed. First, beam dimension is one of the fundamental parameters that affects beam vibration. Beam dimensions must be chosen to meet a number of criteria including the following:

(1) Each beam must have a unique natural frequency

(2) The beams must be able to be manufactured with a current manufacturing method

(3) The difference in resonant frequency between any two beams must be greater than one bandwidth, in order to minimize crosstalk between the beams

(4) The natural frequency of every beam must be within the range of frequencies that can be produced by a single speaker or surface transducer

(5) The number of beams should be maximized

(6) The vibrational amplitude of the beams should be maximized

These 6 criteria are used to develop a simulation tool using Matlab to design beam dimensions. Complete arrays of vibratory beams are designed using the damping ratio calculated in the impulse response test. The optimization simulation tool runs an algorithm that proceeds as follows:

(1) Input the minimum and maximum manufacturable beam dimensions and lengths

(2) Input the manufacturing resolutions in the X/Y plane and in the Z direction

(3) Input the material properties

(4) Generate a list of all possible beam dimension combinations of widths, heights and lengths

(5) Calculate the resonant frequency, the maximum amplitude of vibration, and the bandwidth for all beams

(6) Eliminate all beams with a resonant frequency lower than 20Hz or higher than 20kHz

(7) (a) Select the beam with the lowest resonant frequency

or

(7) (b) Select the beam with the highest amplitude

(8) Eliminate from the list the selected beam and all beams with a resonant frequency within n bandwidths of the selected beam, where n≥1

(9) Go back to step 7 and continue until all beams have been eliminated

The simulation tool calculates the natural frequencies and amplitudes of all of the beams. The optimization algorithm either chooses the beam with the lowest frequency or

2 6

the beam with the maximum amplitude and removes the selected beam from the list of all

beams possible. The beam is added to the list of chosen beams. Then, the algorithm

calculates the bandwidth of that beam, given the damping ratio. The algorithm also

removes any beam having a resonant frequency within the bandwidth of the selected

beam, in order to reduce crosstalk between beams. This continues until no more beam can

be selected. Since a human experiment has not been conducted yet at the present stage of

research, it is unknown which algorithm using either the lowest frequency or the

maximum amplitude would be better to be applied for the proposed system. After

conducting the human experiment, one of the algorithms will be selected.

Another important parameter, material, is also considered in the optimization

algorithm since elastic modulus and damping ratio, which have a significant effect on

beams' natural frequency and bandwidth, is dependent on the material. Here, both

polymers and metals are considered. Some polymer materials under consideration include

PLA (Polylactic Acid), ABS (Acrylonitrile butadiene styrene) material, Photopolymer

Resin, and Verowhiteplus RGD 835 material. These polymer materials are initially under

consideration because of their ease of manufacturing using additive methods. In order to

consider PLA, an impulse test is performed on a test PLA beam, which will be discussed

in the section 5, Vibration Experimentation; in this way, it is determined that the damping

ratio of PLA is about 0.01. Metal materials in consideration for beam manufacture

include stainless steel, brass, aluminum, and tungsten carbide. Table 1 reports the initially

known material properties for the materials under consideration.

Table 1. Materials under consideration for a microbeam array, along with relevant
material properties.

Material	E [GPa]	ρ [kg/m^3]	ζ

PLA	3.59	1250	0.01
ABS	1.4~3.1	1057	Unknown
Photopolymer Resin	1.6	1120	Unknown
RGD 835	2.5	1170	Unknown
Stainless Steel	210	7800	0.006
Brass	110	8400	0.00095
Aluminum 6061	69	2720	0.0004
Tungsten Carbide	600	15600	0.001

Only materials which are feasible with manufacturing methods under consideration are considered. There are several manufacturing methods that can make small objects such as microbeam. However, in the proposed system, many small beams should be placed with small space between each beam. This tiny space has only allowed few manufacturing methods. For example, the micro milling, which is one of popular methods for small object manufacture, cannot be used for the system since micro milling tool is not enough long to cut the small beams. Here, three methods of manufacture are initially considered: FDM (finite deposition modeling) 3D printing, Metal sintering 3D printing, and wire EDM (electric discharge machining).

FDM 3D printing is an inexpensive and easily-accessible manufacturing method that can be used to quickly iterate beam designs. However, this method can only be used to manufacture with thermoplastics, which have much higher damping ratios than metals. This is important since fewer beams can be allowed to manufacture by this method due to the high damping ratio. This is explained more specifically in the explanation of bandwidth below.

Metal sintering 3D printing has the advantage of being able to manufacture very high aspect-ratio beams. It also allows to make a circular beam cross-section so that inertia moment of area, I, is same in any direction. However, this method is very

expensive and also has a relatively low X/Y plane resolution due to the particle size of the metal powders used in the sintering process. This particle size of the metal powers also results in the print having non-clear and non-uniform surface as shown in Fig. 11, which shows a beam array made by metal sintering 3D printer pictured by a microscope. This non-clear surface causes the difficulty of dimension measurement, and it is hard to predict the resonant frequency of the print. Additionally, it is also found that metal 3D printing cannot make a perfect circular beam cross-section in micro scale due to metal powder size.

(a)   (b)
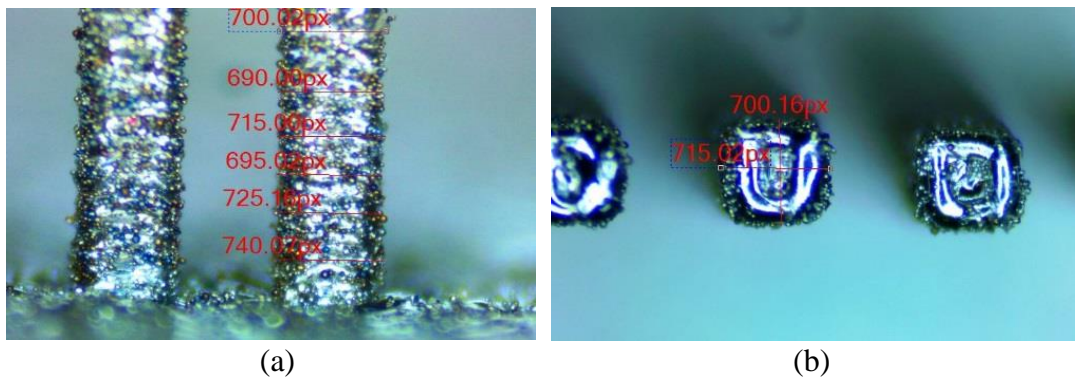
Fig. 11. Microscope images of the beam array manufactured by metal 3D printing. (a) Manufactured beam from the side view. (b) Manufactured beam from the top view.

Wire EDM has the benefit of low-cost manufacture compared to metal 3D printing and very high X/Y plane resolution. Since it is cutting manufacture method, it also allows to make the object having very clear surface. However, internal stresses in the material will be released during manufacture, deforming beams of high aspect-ratio; thus, the smallest diameter of beam that can be made with wire EDM is larger than what can be produced with metal 3D printing. Additionally, wire EDM can only be used to manufacture beams with square cross-sectional shape, as opposed to the round cross-sectional shapes possible with FDM and metal 3D printing methods. Fig. 12 shows the

manufacture failure due to the internal stress in wire EDM manufacturing, and Table 2

summarizes the pros and cons of the manufacturing methods considered in this

prototyping effort.
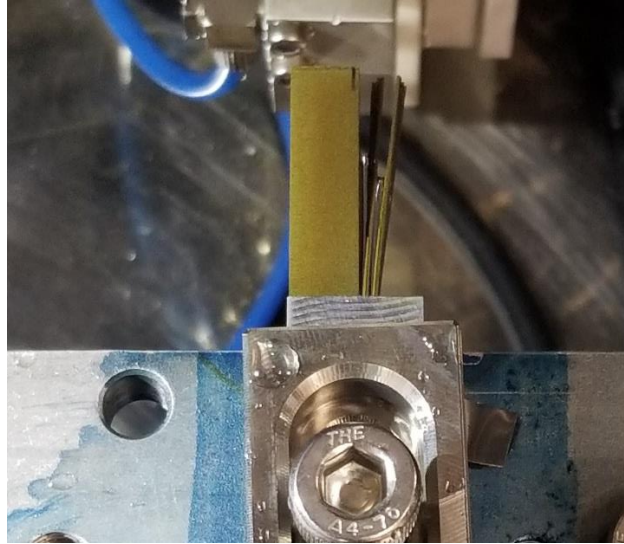
Fig. 12. The manufacture failure due to the internal stress in wire EDM manufacturing.

Table 2. Pros and cons of the manufacturing methods considered in this research.

Manufacturing Method	Pros	Cons
FDM	Inexpensive, short design iteration time, circular beam cross-section	Thermoplastics have high damping ratio, can only produce diameters as small as 1mm, inaccurate dimensions
Metal 3D printing	Can make beam diameters as small as 0.1mm, accurate dimensions, circular cross-sections, metals have low damping ratio, high aspect-ratios	Expensive, low manufacturing X/Y resolution
Wire EDM	high manufacturing X/Y resolution, accurate dimensions, metals have low damping ratio	Less expensive than metal 3D printing, square beam cross-sections, limited aspect ratios

The bandwidth of each beam is also taken into account to obtain the maximum

number of beams. The Bandwidth means the width of a frequency band. In order to

obtain high resolution, many beams are required for the system, which is individually

controlled by a certain resonant frequency. If the bandwidth of a beam is too broad, there would be crosstalk between beams, which means two or more beams could vibrate at a certain frequency simultaneously. This crosstalk can hinder people to recognize the targeted beam vibration. The good vibrational model with less crosstalk is described in the Fig. 13.
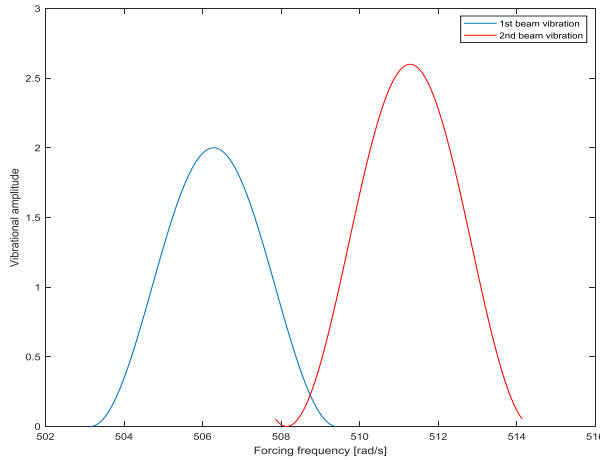
Fig. 13. Bandwidth of two beams.

The bandwidth, Δf, can be calculated as in Eq. (47), where fn is the natural frequency of a beam and Q is a quality factor. The quality factor can be calculated by Eq. (48), where ζ is the damping ratio of the material.

$$\Delta f = \frac{fn}{Q} \qquad (47)$$

$$Q = \frac{1}{2\zeta} \qquad (48)$$

The design simulation algorithm is run with several sets of conditions explained above to determine the maximum number of beams that could be produced under the specified conditions, which is mentioned above in 9 steps. Table 3 reports the optimization results in the frequency range from 20 to 20kHz.

Table 3. Results of beam dimensions design optimization algorithm for reasonable

conditions for the three manufacturing methods under consideration.

Material	Mfg. Method	Cross-Sectional Shape	Allowable Diameters [mm]	Allowable Lengths [mm]	n	Number of Beams
PLA	FDM	Circle	1:0.1:1.5	20:0.1:25	1	30
Stainless Steel	Sintering	Circle	0.1:0.1:1.0	10:0.01:30	1	8,982
A2 Tool Steel	EDM	Square	0.4:0.01:1.0	10:0.01:30	1	12,961

Table 3 shows that the number of beams that can be connected to a single speaker or surface transducer is much higher for sintering and wire EDM methods than for FDM, but that the number of beams in sintering and EDM are comparable. Each prototype is made by Sintering and EDM, and they are analyzed by forced response vibration experiment. As a result, for plastic material manufacture, FDM is selected, and for metal material manufacture, wire EDM is selected. Even though the minimum diameter of beam that can be made with wire EDM is larger than what can be produced with metal 3D printing due to limited aspect ratio, the total number of beams that can be made with wire EDM is bigger due to high X/Y resolution, which is 10 times bigger than metal sintering method. The ability to make more beam is important to achieve higher resolution. The more detailed reason is described in chapter 5, Vibration and Experimentation.

4.2 Prototyping

4.2.1 Plastic Material Prototyping
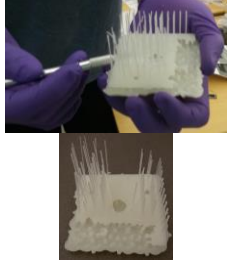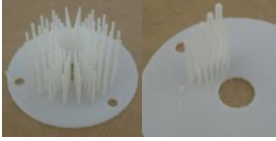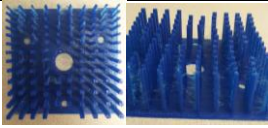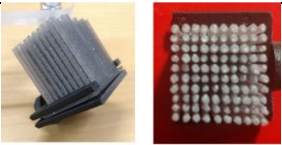
In order to proof the concept proposed, it is necessary to produce a prototype of the beam array.

Since the beams must be able to be manufactured with a current manufacturing

method, several kinds of 3D printers in Arizona State University are used. For this first prototyping effort, an FDM method is used to create the beams out of a PLA (Polylactic Acid) material, an ABS (Acrylonitrile butadiene styrene) material, Photopolymer Resin, or RGD 835 material. Prototype manufacturing is divided into 3 large phases: 1. Proof of concept stage 2. Beam manufacture improvement stage 3. Vibration model refinement stage. A simple array of beams is manufactured using in-house 3D printers at ASU, and images of those prototypes are shown in Table 4.

Table 4. Plastic prototypes and their research questions.

Prototype #		Picture	Goal/Research question	Parameters	Results
Phase 1; Proof of Concept Stage	1		Vertical beams made by 3D printer	Lulzbot, PLA material, 20 beams, 2mm thick circular base, w=1mm, L=20mm-0.2mm	Unclear surface. Many strings.
	2		Beam base thickness and low resolution	Same condition as the 1st, 1mm thick base, Bigger distance between beams	Most beams vibration.
Phase 2; Beam Manufacture Improvement Stage	3		More accurate model made by other 3D printers	Objet, ABS material, 100 beams, 1mm thick base, w=1mm+0.1mm L=20mm-0.2mm	Manufacture failure. Water pressure.
	4		More accurate model made by other 3D printers	Fortus, ABS material, 100 beams, 1mm thick base, w=1mm+0.1mm L=20mm-0.2mm	Only 2 beams vibration. Found that thicker beam size than the designed.

	5		More accurate model made by other 3D printers	form 1+, Photopolymer Resin, 13x11 beams, 1mm thick rectangular base, W=0.7+0.04mm, L=40mm-(15degree)	Manufacture failure. Bent beams. Broken beam base.
	6		More accurate model made by other 3D printers	objet, RGD 835, 100 beams, 1mm thick base, w=1mm+0.1mm L=20mm-0.2mm	No beam vibration. No string.
Phase 3; Vibration Model Refinement Stage	7		The range of speaker and beam vibration	Lulzbot, PLA material, 13x11 beams, 1mm thick base, W=1mm+0.1mm, L=20mm-0.2mm	One beam vibration. Too thick and short beams. Many strings.
	8		More accurate model made having same frequency by other 3D printers considering the spec. of printers.	form 1+, Photopolymer Resin, 5x3 beams, 1mm thick base, smallest=0.31mm W and 11.14mm L, largest=1.55mm W and 24.9mm L	Manufacture failure. Hard to cut the supporting part.
	9		More accurate model made having certain angle by other 3D printers considering the spec. of printers.	form 1+, Photopolymer Resin, 5x3 beams, 1mm thick base, W=0.7+0.04mm, L=40mm-(15degree), 60 degrees angle	Manufacture failure.
Final Prototype of PLA	10		Isolate beam control	Lulzbot, PLA material, 10 x 10 beams, 2mm thick base, w=1mm, L=20mm-0.2mm	Succeed. Some strings. Not uniform surface.

Every prototype is tested with simple experiment setup to solve each experiment goal, and the details on the experiment and result will be discussed in chapter 5 Vibration Experimentation. Here, every plastic prototype mentioned above is explained, and the

detailed description for plastic material prototypes is described in Appendix A.

4.2.1.1 Proof of Concept Stage in Plastic Material Prototyping

The 1st phase, proof of concept stage, includes 1st and 2nd prototype. In this stage, simple beams are designed without the consideration of many design parameters. The goal to see if beams having different dimension have different resonant frequency, and to see if the frequency of sound wave coming from a speaker can resonate a beam having same frequency.

For the 1st prototype, PLA material and Lulzbot 3D printer are used. Total 20 beams are made in a circular pattern on a 2mm thick base. All beams are designed to have a square cross section with 1mm on each side. After beam manufacture, it is found that there are many surplus materials like strings, which are connected between each beam since FDM is the method that some amount of molten plastic is squeezed from the nozzle to be added to a targeted point. It seems to need a better Lulzbot 3D printer setup to obtain more accurate model without the surplus material.

For the 2nd prototype, the same conditions as the 1st prototypes are used, and only beam base thickness is changed. The 2nd prototype also has unclear surface of beams and many strings between them.

After testing the 1st and 2nd prototypes, the 1st high speed camera experiment is conducted to prove my research concept. The details on the experiment and result will be discussed in chapter 5 Vibration Experimentation.

4.2.1.2 Beam Manufacture Improvement Stage in Plastic Material Prototyping

The 2nd phase, beam manufacture improvement stage, includes 3rd, 4th, 5th, and 6th prototype. In this stage, other diverse 3D printers and materials are used to make the

better beam array having clearer surface and more accurate dimension.

For the 3rd prototype, ABS material and Objet 3D printer are used. Total 100 beams are made in 5 circular patterns on a 1mm thick base. Each circular pattern has 20 beams. The Objet 3D printer utilizes 'support material', that encases the targeted model after manufacture, and it must be removed by water jet. However, since the beams are very thin and long, even the water jet with the lowest water pressure has destroyed the beam array.

For the 4th prototype, the same conditions as the 3rd prototype are used in different 3D printer, Fortus 3D printer. Since ABS is a softer material, the actual dimension of beam array is larger than the designed dimensions. The cross-sectional shape of beams also exhibits poor squareness.

For the 5th prototype, form 1+ 3D printer and its material, Photopolymer Resin, are used. This printer has better accuracy in manufacture than the previously-used 3D printers such as the Lulzbot. The Form 1+, however, is an SLA (stereolithography) model, which uses a liquid resin material which solidifies under exposure to lasers light. How it works is described specifically in Appendix A. A total of 143 beams are attempted in a 13 x 11 rectangular pattern on a 1mm thick base. All beams are designed to have a rectangular cross section. However, the half of beam base is made, and another half is completely failed, as shown in Table 4. Some beams are also detached or broken from the beam array when washing them in a sealable tub filled with isopropyl alcohol since they are thin and long. Even the beam made successfully does not have good quality.

For the 6th prototype, Objet 24 3D printer and its material, VeroWhitePlus (RGD835), are used. There are 2 type of material options; which are glossy and matte.

The printing method for glossy type is as similar as the previously-used Lulzbot 3D printer, and the printing method for matte type is as similar as the Object 3D printer. 2 type options are both tried to make 2 models having different beam dimension and number of beams. Every model is designed based on the calculation considering printer specification and the aspect ratio of beam length to thickness. The models are manufactured successfully in both glossy and matte type. The matte type, however, has a support material wrapping the model, and the model is broken when washing it due to high water pressure as same as prototype 3.

4.2.1.3 Vibration Model Refinement Stage in Plastic Material Prototyping

The 3rd phase, vibration model refinement stage, includes 7th, 8th, and 9th prototype. In this stage, design specification such as the ratio of beam length to thickness is considered to make the beam array successfully. Based on the result of manufacture failure in the 2nd phase, each printer's real design limit for small and thin structure like beams is also considered to improve manufacture quality.

For the 7th prototype, Total 143 beams of PLA, 13 x 11 beams, are made in a rectangular pattern on a 1mm thick base. The rectangular shape is selected for the beam base this time. Since the speaker used for the experiment has circular shape, it needs to be known if the beams located out of the range of speaker could be excited. After manufacturing, it is found that every beam dimension of actual model is thicker than the designed dimension.

For the 8th prototype, the same material and 3D printer as the 6th prototype are used. This time the specification of the printers and the ratio of beam length and thickness are considered to improve manufacturing. Base on the test result of the 5th prototype, the

45 degree of initial angle for making the print is also considered. However, beams in the first column, which are smallest beams, are not made at all, and other beams made successfully have relatively thin thickness and are bent. Despite of consideration of the specification of the printer, it could not make the beam array. It seems this printer is not good option to make the model having thin and long dimension.

For the 9h prototype, every set up is the same as the one of the 7th prototype to make tilted beams. Since the finger touch to the beam tip could hinder beam vibration, the tilted beams are considered for beam vibration model. Similar to the result of 7th prototype, some beams are not made, and some are bent. The beam base is even broken.

After manufacture models in the phase 3, the 2nd high speed camera experiment, impulse response test, is conducted to find various design variables of PLA material. In order to create a device like the one suggested, especially the damping ratio of the material is one critical parameter that needs to be investigated. The details on the experiment and result will be discussed in chapter 5 Vibration Experimentation.

4.2.1.4 Final Plastic Material Prototype

For the 10th prototype, the final plastic prototype, a 10 x10 array of vibratory beams is designed using the damping ratio calculated in impulse response test in the chapter 5, Vibration Experimentation. A set of beam dimensions which satisfies the five requirements that was discussed above is estimated. The beam array consists of beams between 1mm and 1.4mm in diameter, at 0.1mm increments, and lengths between 20mm and 25mm, in 0.1mm increments, as shown in Table 4.
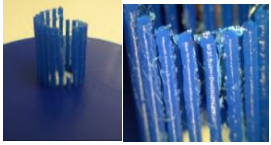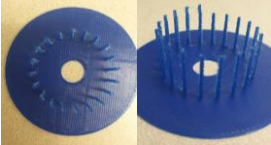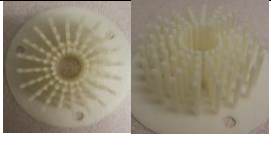
4.2.1.5 Conclusion in Plastic Material Prototyping

Total 10 plastic prototypes are created and evaluated by the simple vibration

experiment described in chapter 5 Vibration Experimentation. Every detailed description for each prototype is explained in Appendix A. The method using Lulzbot 3D printer could make the beam array successfully, and many beams' vibration in the beam array are observed. One material option of Object 3D printer could make the beam array, but no beam vibration is observed at all. In the prototype made by Fortus 3D printer, only 2 beams vibration are observed. The method using form 1+ 3D printer fails entirely to make the beam array even under consideration of the specification of the printer. For these reasons, the most promising methods tested for plastic material is Lulzbot 3D printer. The better printing setup for Lulzbot is found to remove the surplus material 'strings', and it is used to make the final PLA prototype. The final prototype is able to be used in a preliminary experiment to determine the damping ratio of PLA and is successfully used to proof the concept of the proposed system.

4.2.2 Metal Material Prototyping

After the later experiments with the plastic prototypes in Chapter 5, it is found that plastic materials such as PLA have higher damping ratios, which cause broader bandwidth and more crosstalk between each beam. For this reason, diverse metal materials are considered to manufacture new beam arrays made of a metal material, as shown in Table 1.

For the manufacture of metal prototypes, wire EDM and metal sintering 3D printing are considered. To decide the better manufacturing method for the beam array, the same beam array is manufactured by both methods. Wire EDM is then selected to manufacture new prototypes for human experiment in Chapter 7. Table 5 shows the image, research goal, parameters, and results of each metal prototype.

Table 5. Metal prototypes and their research questions.

Prototype #	Picture	Goal/Research Question	Parameters	Result
1		9 beams in a row made by wire EDM. Comparison of manufacture method.	Wire EDM. A2 tool steel. w & h=0.4mm. L=12.05mm-0.05mm except the 3rd beam.	Similar width dimensions. Smaller height dimensions. Good X/Y resolution.
2		9 beams in a row made by metal sintering 3D printer. Comparison of manufacture method.	Sintering 3D printing. Stainless steel. Same designed dimension with the 1st metal prototype.	Larger width dimensions. Larger height dimensions. Poor X/Y resolution.
3		Making 25 beams of a beam array with lower frequency range.	Wire EDM. A2 tool steel. w & h=0.44mm. L=29.84mm~30.00mm.	Bending beams due to internal stress of the material and water jet of wire EDM.
		Making a contact plate for lack of perception problem.	Micromilling. Aluminum. 25 rectangular holes.	Successfully manufactured.
4		Making 12 beams in a row of a beam array with lower frequency range.	Wire EDM. A2 tool steel. h=1.2mm. W=0.5~1.1mm. L=30.00mm.	Similar height dimensions. Little larger width dimensions. L=29.6mm. Good X/Y resolution.
5		Making 400 beams for human experiment	Sintering 3D printing. CO-538-1 material. w=0.1~1.5mm. h=w+0.1mm. L=30.0~59.8mm.	Successfully manufactured. Some thin beams broken or bended.

4.2.2.1 The 1st Metal Prototyping using Wire EDM

It is found with PLA prototypes experiments that another material having lower damping ratio than PLA material is needed to reduce the bandwidth. As shown in Table 1, diverse metal materials are considered to find a proper metal material having low damping ratio, and A2 tool steel has been selected.

To investigate the proposed microbeam array concept, 9 beams are selected as the 1st metal prototype from the set of beam dimensions generated by the optimization algorithm for wire EDM. These 9 beams are selected to be close in resonant frequency and also close in dimensions, for ease of manufacture and ease of testing. Table 6 reports the dimensions of the 9 beams selected for wire EDM manufacturing.

Table 6. List of the 9 beams selected for testing from the complete set of beams output by the optimization algorithm.

Beam Number	Diameter [mm]	Length [mm]	Calculated Resonant Frequency [Hz]
1	0.4	12.05	2309
2	0.4	12.00	2328
3	0.4	11.90	2367
4	0.4	11.85	2387
5	0.4	11.80	2408
6	0.4	11.75	2428
7	0.4	11.70	2449
8	0.4	11.65	2470
9	0.4	11.60	2491

The 9-beam row is manufactured on a Fanuc wire EDM at Arizona State University. Fig. 14 shows pictures of the manufactured beams from the side and top views.

(a)   (b)
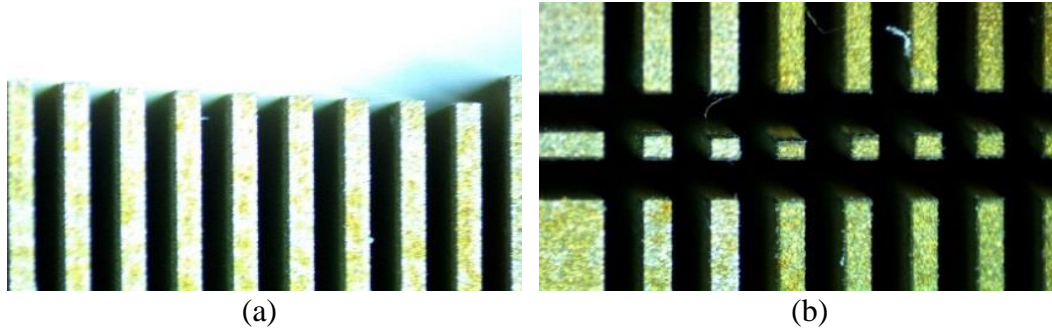
Fig. 14. Images of the 9 test beams manufactured by wire EDM. (a) Manufactured beam from the side view. (b) Manufactured beam from the top view.

After the part is manufactured, microscope imaging is used to measure the actual produced dimensions of the beams. Table 7 reports the actual measured beam dimensions. Note that one pixel in the measuring image corresponds to approximately 1.17 micron.

Table 7. List of the actual dimensions of the 9 beams made by wire EDM.

Beam Number	Actual Width [mm]	Actual Height [mm]	Dimension between Each Beam [mm]
1	0.3953	0.3605	0.5407
2	0.3953	0.3372	0.5407
3	0.3895	0.2849	0.5407
4	0.3895	0.3721	0.5465
5	0.3895	0.3837	0.5465
6	0.3895	0.3837	0.5407
7	0.3837	0.3837	0.5407
8	0.3895	0.3837	0.5465
9	0.3837	0.3779	-

Compared to the design dimension as shown in Table 6, the actual dimension of the 9 beams made by wire EDM is around 4% smaller in width and around 9% smaller in height. This may be because wire EDM is a subtractive, rather than additive, manufacturing method, so the manufactured remaining part could have a little bit smaller dimension than intended. The 3rd beam shows a significantly smaller height, and this

could be due to the internal stress released during wire EDM manufacturing, causing the beam to bend during cutting. Considering the dimension between each beam, wire EDM can achieve very good and consistent X/Y plane resolution.

4.2.2.2 The 2nd Metal Prototyping using Metal Sintering 3D Printer

To make a prototype using metal material, there are two possible manufacturing methods available at Arizona State University: wire EDM and metal sintering 3D printing. In order to compare the abilities of the two methods to accurately produce the required structures, the same prototypes are made using both wire EDM and metal sintering 3D printer. The same set of beam dimensions, as shown in Table 6, are generated by the optimization algorithm, and these 9 beams are selected to be close in resonant frequency and also close in dimensions, for ease of manufacture and ease of testing.

The 9-beam row is manufactured on a metal sintering 3D printer in Startup lab at Arizona State University. Fig. 15 shows images of the 9 test beams manufactured by the metal 3D printer.
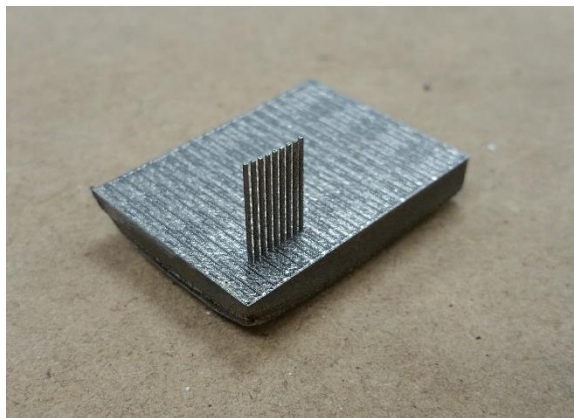
Fig. 15. Images of the 9 test beams manufactured by metal 3D printer.

After the part is manufactured, microscope imaging is used to measure the actual

produced dimensions of the beams. Since the metal 3D printer has low X/Y plane resolution due to the particle size of metal powder as shown in Fig. 11, the actual dimension of the produced beams varies along the length of the beams. For this reason, the average value of measured dimensions is selected to calculate the resonant frequency of each beam. Table 8 reports the actual measured beam dimensions. Note that one pixel in the measuring image corresponds to approximately 0.704 micron, the longest beam is beam number 1, and the shortest beam is beam number 9. As shown in Fig. 15, since all beam are in a row, the widths of each beam can be measured along the length of the beams, but the heights cannot be measured along the length. For this reason, the widths of each beam are measured several times along the length on the side view, but the heights are measured once on the top view.

Table 8. List of the actual dimensions of the 9 beams made by metal 3D printer.

Beam Number	Actual Width [mm]	Actual Height [mm]	Dimension between Each Beam [mm]
1	0.4913±0.004546	0.4860	0.4284
2	0.5053±0.024518	0.5000	0.4284
3	0.5070±0.003514	0.5035	0.4389
4	0.4983±0.007118	0.5035	0.4214
5	0.4983±0.007219	0.5000	0.4301
6	0.4930±0.004959	0.4860	0.4301
7	0.5000±0.006424	0.4895	0.4284
8	0.4983±0.003870	0.4860	0.4301
9	0.4965±0.012385	0.4895	-

Compared to the design dimension as shown in Table 6, the actual dimension of the 9 beams made by wire EDM is much bigger. This may be because metal sintering 3D printer is an additive, rather than subtractive, manufacturing method. It is found that wire EDM can manufacture the beam array with more accurate dimensions than metal

sintering 3D printing.

4.2.2.3 The 3rd Metal Prototyping using Wire EDM

4.2.2.3.1 Metal Beam Array Prototyping

Based on the experiment result using the 1st metal prototype made by wire EDM and the 2nd metal prototype made by metal sintering 3D printer, wire EDM is selected to make further metal prototypes. The detailed reason is described in Chapter 5, Vibration and Experiment.

In the previous prototyping and experiment, it is found that the frequency of each beam is greater than 2000 Hz. For the resonant vibration cantilever beam system, it is desirable to minimize beam natural frequency. Minimizing natural frequency is important considering that the perceivable frequency range with static touch is generally known to be from 10 Hz to 500 Hz (Bolanowski Jr et al. 1988). The perceivable frequency range with dynamic touch is currently unknown, although it is generally assumed that lower frequencies are more perceivable than higher frequencies. There are two possible ways to reduce the resonant frequency of a beam: decreasing the cross-sectional area or increasing the beam length. Decreasing the area of the cross-section may not be successful since previous prototypes have shown that smaller (thinner) beams are often damaged during manufacture by wire EDM. As a result, in this 3rd prototype, a beam array having longer beams is made to decrease the frequency range of the beam array.

25 beams are selected for the 3rd metal prototype, and every width and height of each beam cross-section is the same as the previous prototype, but the length of each beam is different. The width and height of each beam is 0.44 mm. The designed dimension and the actual dimension such as width, height, and length are reported in the

Table 9. The 25 beams are manufactured on a Fanuc wire EDM at Arizona State University. Fig. 16 shows pictures of the manufactured 5x5 beams.

(a)   (b)
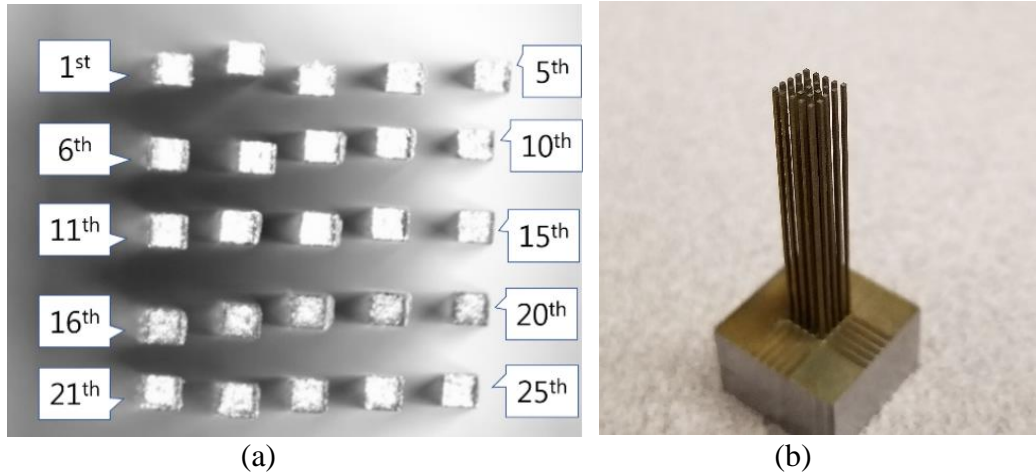
Fig. 16. Images of the 25 test beams manufactured by wire EDM. (a) Image via microscope. (b) Manufactured 5x5 beam.

After the part is manufactured, microscope imaging is used to measure the actual produced dimensions of the beams. Table 9 reports the actual measured beam dimensions and design dimension.

Table 9. List of the actual dimensions of the 25 beams made by wire EDM.

Beam Number	Actual Width [mm]	Actual Height [mm]	Actual Length [mm]	Designed Height/Width [mm]
1	0.4440	0.3924	29.97	0.4400
2	0.4526	0.3953	29.96	0.4400
3	0.4211	0.3953	29.95	0.4400
4	0.4499	0.3925	29.94	0.4400
5	0.4126	0.3897	29.93	0.4400
6	0.4499	0.3867	29.92	0.4400
7	0.4354	0.3839	29.91	0.4400
8	0.3982	0.3871	29.90	0.4400
9	0.4215	0.3868	29.89	0.4400
10	0.4126	0.3811	29.88	0.4400
11	0.4354	0.3896	30.00	0.4400
12	0.4670	0.3867	29.97	0.4400

13	0.4354	0.3839	29.86	0.4400
14	0.4354	0.3924	29.85	0.4400
15	0.4268	0.3867	29.84	0.4400
16	0.4326	0.3753	30.00	0.4400
17	0.4184	0.3781	29.99	0.4400
18	0.4469	0.3638	29.98	0.4400
19	0.4268	0.3695	29.98	0.4400
20	0.4326	0.3552	29.96	0.4400
21	0.4241	0.3783	30.00	0.4400
22	0.4325	0.3726	29.99	0.4400
23	0.4329	0.3638	29.98	0.4400
24	0.4469	0.3609	29.97	0.4400
25	0.4268	0.3638	29.96	0.4400

Compared to the design dimension, the actual dimension of the 25 beams made by wire EDM is around 6% smaller in width and around 17% smaller in height. It is found that the actual height is smaller than the actual width since the manufacturing process for height is on the 2nd cutting process, which is more vulnerable to the internal stress generated during wire EDM machining. Compared to the 1st prototype made by wire EDM, it is found that the error between the actual dimension and design dimension of the 3rd prototype is bigger since the length of the beam of the 3rd prototype is much longer so they could be affected more by the internal stress. Considering the dimension between each beam, wire EDM can achieve very good and consistent X/Y plane resolution.

4.2.2.3.2 Contact Plate Prototyping

It has been found from the previous experiment that finger contact to beam tips stops beam vibration. To solve this problem, the idea of making a plate that is positioned at the height of the beam tips is presented. An aluminum thin plate is selected to make the

plate for the 5x5 beams array. It is manufactured by micro-milling machine at Arizona State University.

Considering all actual beam dimensions of 5x5 beam array, 5x5 rectangular holes are made on the plate in order to insert beam tips to the holes, as shown in Fig. 17. The design dimensions of rectangular holes are 0.6 mm in width and 0.45 mm in height so that the beam vibration could be induced in a single direction.
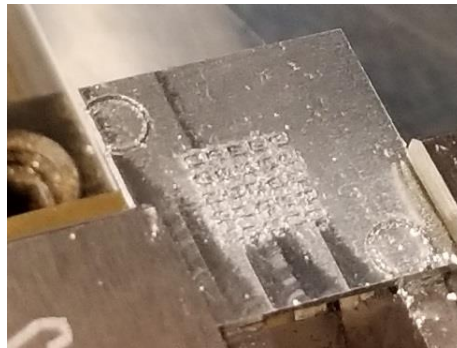
Fig. 17. The plate manufacturing by micro-milling.

In order to conduct an experiment with this plate, the plate must be installed at the same height level of the beam tips. However, due to deformation of the beams during manufacture and due to the small clearance between the hole dimensions and the beam dimensions, the plate could not be installed. Thus, this approach is abandoned in favor of individual rubber interface components further explained in Chapter 7.

4-2-2-4. The 4th Metal Prototyping using Wire EDM

Based on the experimental result of the 3rd metal prototype, it is decided to make beams having low frequency in a row for further experiment. This time, a total of 12 beams in a row were made by wire EDM.

The beam array is designed to have less than 1000Hz as the resonant frequency range for all beams, but the actual dimensions of the beam array are slightly different.

Every beam length is 29.6mm. Fig. 18 shows the image of 12 beams in a row manufactured by wire EDM, and the beam number 1 represents the leftmost beam, and the beam number 12 represents the rightmost beam. Table 10 shows the actual dimensions of the beam array and resonant frequency calculated based on the actual dimensions. This beam array is used to conduct high speed camera experiment to find the actual resonant frequency of each beam and the proper holding type with C clamp and a surface transducer.
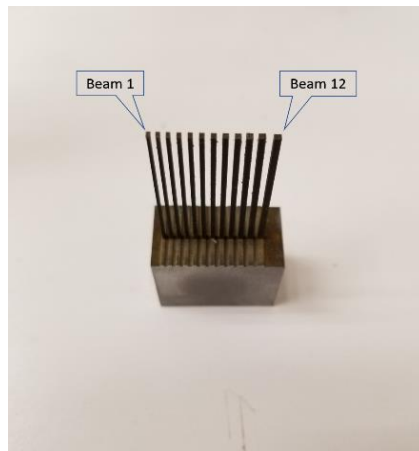
Fig. 18. The image of 12 beams in a row manufactured by wire EDM.

Table 10. List of the actual dimensions of the 12 beams made by wire EDM.

Beam Number	Actual Height [mm]	Actual Width [mm]	Ratio of h and b	Calculated Resonant Frequency [Hz]
1	1.179	0.524	2.249	546.97
2	1.173	0.581	2.018	594.63
3	1.167	0.635	1.837	642.10
4	1.173	0.694	1.690	695.68
5	1.167	0.738	1.582	737.24
6	1.168	0.797	1.466	801.64
7	1.155	0.845	1.367	855.54
8	1.155	0.911	1.268	903.30
9	1.149	0.953	1.206	957.20
10	1.162	1.012	1.148	1017.06
11	1.155	1.070	1.080	1065.01

12	1.155	1.127	1.025	1124.67

4-2-2-5. The 5th Metal Prototyping using Metal Sintering 3D Printer

To conduct human experiment about the user perception for vibration patterns, a new prototype that has 400 beams is made by metal sintering 3D printer to accomplish 400 resolutions. This is competitive with the current highest-resolution haptic display on the market (BrainPort). The prototype is made based on the result in Experiment 18, which investigates the vibration response depending on the decrease of silicone rubber beam length. The beam dimension algorithm in Chapter 4 is used to design optimal beam dimensions so that each beam has a unique resonant frequency and low crosstalk between each beam.

In Experiments 5 and 6, it is revealed that beams made by wire EDM can be controlled more precisely with less crosstalk than the beams made by metal sintering 3D printing. However, metal sintering is selected to manufacture the new prototype due to the limit of manufacture of wire EDM. Wire EDM is a subtractive manufacture method using a wire vertically connected. The wire moves to the material that is fixed on the table of wire EDM and cut the material in a direction using electrodes. For this reason, the dimensions of the beams in the same direction (such as width or height) must be the same for all beams in a particular row or column. In order to make an array of 20x20 beams, at least 20 beams in a row or column must have the same dimension. The result of the beam design algorithm shows that no more than 6 beams can be made with the same dimension in one direction. For this reason, metal sintering is selected.

For the beam design algorithm, stainless steel is considered as the material of metal sintering method. With the mechanical properties of stainless steel such as damping

ratio and elastic modulus, optimal beam dimensions are calculated within 1000Hz frequency range. CO-538-1 powder material is selected for initial manufacture since this material is lower cost than other options. The mechanical properties of a sintered beam are unknown, because they depend on parameters used in the manufacture. For example, the laser power can affect the density of the beam which can also affect the damping ratio and possibly also the elastic modulus. For this reason, the designed resonant frequencies of each beam can be different than the frequencies of the model actually made.

The beam dimension algorithm in Chapter 4 gives a list of combinations of width, height and length of beams that have all unique resonant frequencies. Beams must be placed in such a way that the tops of the beams define a surface with no inflection points in order that the finger or hand is able to contact all beam tips simultaneously. In the combinations of beam dimensions, the 400 longest beams are selected and simulated in Matlab to find an optimal placement for the beams. The first 20 longest beams are located in the first row, and the next 20 longest beams are located in the second row, and so on. Using this placement scheme, the surface defined by the beam tips is a curved surface that has no inflection points, as shown in Fig. 19.

The widths of the 400 beams are 0.1~1.5mm, and heights are all 0.1mm greater than the widths. The lengths of beams are 30.0~59.8mm. The further research will be needed to evaluate the 5th metal prototype.

<div align="center">(a)   (b)</div>
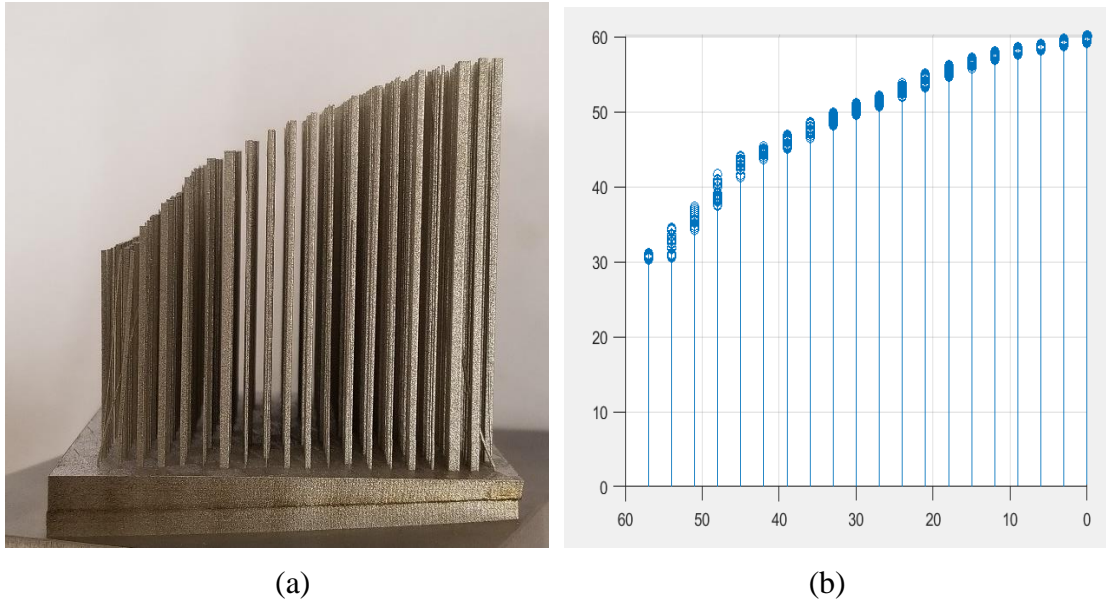
Fig. 19. Image of the 5th metal prototype. (a) The manufactured model on the side view. (b) The simulated model on the side view.

4-2-2-6. Conclusion in Metal Material Prototyping

Metal material prototypes are made since it is found that the material having low damping ratio is needed to minimize the bandwidth between beams in the previous plastic material prototypes experiment.

Since there are two available manufacture methods for metal material: wire EDM and metal sintering 3D printer, the same metal prototypes are made using both methods in order to compare the capabilities of the two methods for the intended structures. An array consisting of 9 beams in a single row is made and used to conduct the high-speed camera experiment. The analyzed result is described in chapter 5 Vibration Experimentation.

Based on the analysis of the result of both methods, wire EDM is selected to make further metal prototypes. A 5x5 beam array having low resonant frequency is created by wire EDM. A plate is also created to attempt to solve the problem that finger contact stops beam vibration. The plate is supposed to be placed at same height of the

beam tips so that a user's finger could not directly force beam tips.

To simplify the installation of the plate, an array of 12 beams in a single row having low frequency is created by wire EDM. This beam array is used to conduct high speed camera experiments and human touch experiments, which are described in Chapter 5 Vibration Experimentation and Chapter 7, Human Experiment.

A 400 beams of array is made by metal sintering 3D printer to accomplish 400 resolutions, which is competitive with the current highest-resolution haptic display on the market (BrainPort). For this prototype, metal sintering is selected due to the limit of manufacture of wire EDM, which is the dimensions of the beams in the same direction (such as width or height) must be the same for all beams in a particular row or column, as explained in Section 4-2-2-5. CO-538-1 powder material is selected for initial manufacture, and the surface defined by the beam tips is a curved surface that has no inflection points.

CHAPTER 5: VIBRATION EXPERIMENTATION

This Chapter presents vibration Experimentation. To find the vibrational

characteristics such as natural frequency and damping ratio, forced and free response

experiment are conducted. Plastic and metal materials are both utilized to find the proper

material for the proposed device, and each experiment setup and result are presented.

Table 11 lists each experiment, its objective, and prototypes that are used for the

corresponding experiments. Refer to Tables 4 and 5 in Chapter 4 for more information on

the prototypes that are referred to in column 4 of Table 11.

Table 11. Experimentations with prototypes.

Experiment		Objective	Prototypes
Experimentation Set 1: Proof of Concept	Experiment 1	Observation of Beam Array Under Sound Forcing in the Beam Axial Direction	$1^{st} \sim 7^{th}$ plastic prototypes
	Experiment 2	High-Speed Camera Investigation	2nd plastic prototype
	Experiment 3	Impulse Response of PLA Beam	2nd plastic prototype
	Experiment 4	Beam Bandwidth and Crosstalk	10th plastic prototype
Experimentation Set 2: Metal Prototype	Experiment 5	Forced Response of EDM Manufactured Prototype	1st metal prototype
	Experiment 6	Forced Response of Sintering Manufactured Prototype	2nd metal prototype
Experimentation Set 3: Low Frequency Metal Beams and a Contact Plate	Experiment 7	Installing a plate on the top of beams contacted to human skin	3rd metal prototype and a plate
Experimentation Set 4: Low Frequency Metal Beams and a Holding Type	Experiment 8	The holding force of a C-clamp measurement	4th metal prototype
	Experiment 9	Three types of holding of C-clamp	4th metal prototype
	Experiment 10	Vibration response with 'Normal holding' type	4th metal prototype

5-1. Experimentation with Plastic Material

Two types of prototypes are made: polymer prototypes and metal prototypes. This section presents the experimental setup and results for the polymer prototypes. One Experimentation Set consisting of 4 individual experiments are reported here: (1) A proof-of-concept experiment investigating the vibrational response of the beams under axial forcing, (2) An investigation of the usefulness of a high-speed camera as a way to quantitatively measure beam vibration, (3) An impulse response test of a single beam made of PLA material, and (4) A preliminary forced-response test of a complete array of beams made of PLA material, forced in the direction perpendicular to the axis.

5-1-1. Experimentation Set 1: Proof of Concept

Every prototype of PLA except the 10th prototype is tested with a simple experiment setup to answer a different research question; The first research objective for this set of experiments is to determine if the beams made of PLA material can be controlled at a certain frequency. The second objective is to determine what kinds of 3D printers and materials are the best for producing plastic prototypes. Third, to determine if the beams that are placed out of the range of speaker can vibrate. Fourth, to determine what is the aspect ratio of beam length and thickness that can be made by various 3D printers.

A forced vibration experiment using a high speed camera and the 2nd prototype is also conducted. The vibration response is recorded and analyzed by Matlab.

5-1-1-1 Experiment 1: Observation of Beam Array under Sound Forcing in the Beam Axial Direction

Research Question:

When a beam array is exposed to sound energy propagating from the base through the beam in the beam's axial direction, can a single beam be made to vibrate in isolation?

Experimental Setup:

As shown Fig. 20, a speaker is placed under the beam base, so that the sound wave coming from the speaker propagates from the base of the beams to the tips (along the axis of the beams). For this experiment, the designed resonant frequency of every beam is calculated based on the lumped mass approximation, as shown in chapter 3, Vibration Analysis. The speaker is connected to an oscilloscope, and the frequency on the oscilloscope is swept around the calculated resonant frequency to find the actual resonant frequency of each beam. Then, the beam vibration is observed with the eye. This same experimental setup is used for prototypes 1-6, but a slightly different setup is used for this experiment on the 7th prototype.
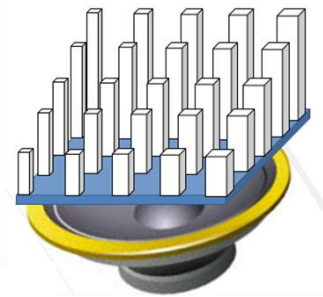
Fig. 20. The experimental setup for plastic material prototypes.

Experimental Results:

With the 1st plastic prototype, it is found that some beams vibrate at certain frequencies, but the amplitude of the beam vibration is small, and other beams did not vibrate at any frequency.

With the 2nd plastic prototype, it is found that most beams vibrate at certain frequencies, and the beam vibration moves from beam to beam as the frequency of oscilloscope is changed. This result proves the concept of the resonant microbeam array. However, only the first few longest beams' amplitudes are large enough to observe by eye. To increase the amplitude of beam vibration, it is hypothesized that beam design parameters such as damping ratio and quality factor need to be modified.

With the 4th plastic prototype, vibration is observed in only 2 longest beams in the 5th ring, and no other beam vibration is observed with the eye.

With the 6th plastic prototype, it is found that no beam vibration is observed at all.

With the 7th plastic prototype, only one beam vibration is observed with the eye. Beams on the edge of the beam base, which are located on the area of outside speaker, do not vibrate.

Other plastic material prototypes could not be tested since they failed to during manufacture.

5-1-1-2 Experiment 2: High-Speed Camera Investigation

A forced vibration experiment using a high-speed camera is performed on the 2nd prototype with the help of the Technical Imaging Lab at ASU Polytechnic.

Research Question:

Can a high-speed camera be used to record and analyze the vibration of beams in an array?

Experimental Setup:

The same experiment setup as Experiment 1 is used as shown in Fig. 20, and a

high-speed camera is also set up to record the beam vibration. The camera frame rate is set to 4700 frames/s, and the beam vibration is recorded at the top view for a beam tip. An image of the high-speed camera experiment is shown in Fig. 21. From the recorded video, a pixel to mm conversion factor (pixels/mm) is calculated by the comparison of real diameter of a beam and pixel value. Then, the Matlab codes, 'VideoReader' and 'vision.PointTracker', are used to load the recorded video and track the beam vibration by making a tracking point on the beam tip, as shown in Fig. 22.
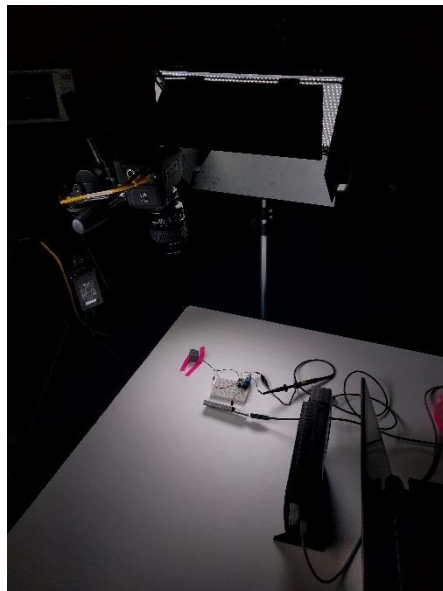
Fig. 21. The experiment setup with a high speed camera.

Fig. 22. The beam prototype of PLA and tracking point.

Experimental Results:

The first 20 frames are tracked, and the tracked data is shown in Table 12. Fig. 23 shows the x and y position of the beam over time.

Table 12. The tracked data of a beam in first 20 frames.

Frame	Pixel Position x	Pixel Position y	Position x [mm]	Position y [mm]	Time [ms]
1	167	128	6.383291262	4.892582524	0
2	164	124	6.268621359	4.73968932	0.212766
3	161	121	6.153951456	4.625019417	0.425532
4	164	120	6.268621359	4.586796117	0.638298
5	166	122	6.345067961	4.663242718	0.851064
6	168	126	6.421514563	4.816135922	1.063830
7	169	127	6.459737864	4.854359223	1.276596
8	166	126	6.345067961	4.816135922	1.489362
9	163	123	6.230398058	4.701466019	1.702128
10	163	121	6.230398058	4.625019417	1.914894
11	165	121	6.30684466	4.625019417	2.127660
12	167	123	6.383291262	4.701466019	2.340426
13	169	125	6.459737864	4.777912621	2.553191
14	168	126	6.421514563	4.816135922	2.765957
15	164	124	6.268621359	4.73968932	2.978723
16	163	123	6.230398058	4.701466019	3.191489
17	164	122	6.268621359	4.663242718	3.404255
18	166	124	6.345067961	4.73968932	3.617021
19	168	126	6.421514563	4.816135922	3.829787
20	168	128	6.421514563	4.892582524	4.042553
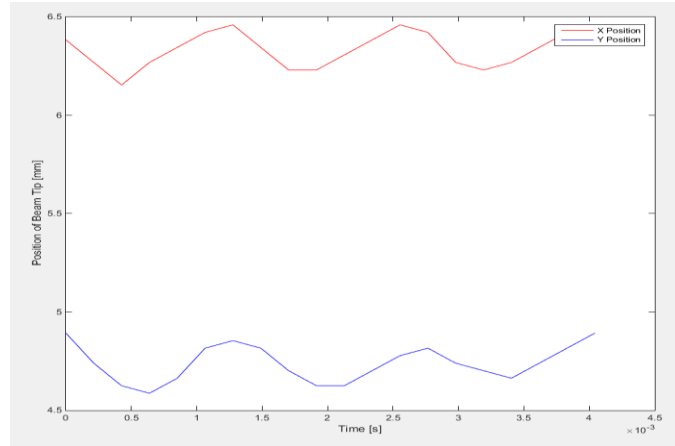
Fig. 23. *x* and *y* position of a beam of PLA in forced vibration.

Fig. 23 shows sinusoidal motion of the *x* and *y* position of a beam vibration. The time between two peaks is 0.0002128 seconds, which works out to 671.6 Hz. Considering manufacture error that the beam shape is not circular, the resonant frequency with the maximum amplitude of the beam might be slightly different with the calculated frequency. This result of the forced response of the beam can prove the resonant beam vibration concept. The total distance moved between a peak and a valley is 0.3243mm, and with the beam being only 1mm in width, that means it is vibrating a little more than 30% of its width.

5-1-1-3 Experiment 3: Impulse Response of PLA Beam

In order to create a device like the one proposed, the damping ratio of the material is one critical parameter that needs to be investigated. The damping ratio affects the difference between the natural and resonant frequencies, and also has a significant effect on the vibrational amplitude of a beam. For example, consider a beam made of PLA plastic with a round cross-section, 20mm long and 1mm in diameter. Given the known PLA density of 1250 kg/m^3 and modulus of elasticity of 3.59 GPa, Fig. 5 shows the amplitude component of the frequency response of this beam given two different

6 0

values of the damping ratio. This figure shows that the maximum vibrational amplitude of the beam with damping ratio 0.005 is 5 times lower than the beam with damping ratio 0.001. Moreover, since damping ratio is related to many other parameters that affect beam vibration, this impulse response experiment, the 2nd high speed camera experiment, is conducted to obtain the free response of a beam.

Research Question:

What is the damping ratio of a beam made of PLA material?

Experimental Setup:

For this experiment, an FDM method is used to create the beams out of a PLA material. Based on the result of Experiment 1, the 2nd prototype is selected for this experiment. To obtain a refined print, several setups for Lulzbot 3D printer are tested. The final refined version of the prototype has much a clearer surface than the previous 2nd prototype, and there is no 'strings' (thin stretches of PLA material which occur due to poor material retraction) between beams with the eye, as shown in Fig. 24. In this prototype, all beams are 1mm in diameter, and each beam is 0.5mm shorter than the beam next to it. The longest beam is 20mm long.
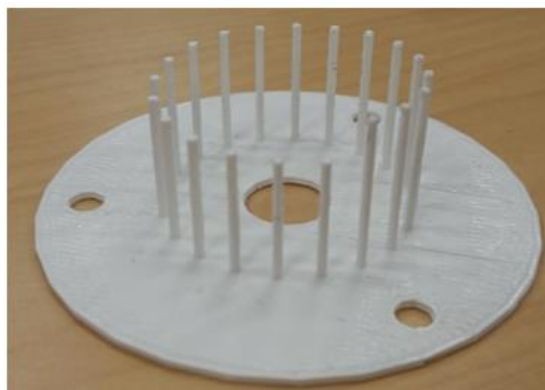
Fig. 24. The refined 2nd prototype of PLA.

An impulse test is then performed to determine the damping ratio of the PLA

material. The top of the longest beam is placed within view of a high-speed camera, and a small metal rod is used to 'flick' the beam, thus exciting the beam's natural frequency. The resulting vibration of the beam is recorded at 7104 frames/s. Fig. 25 shows one frame of the high-speed camera impulse test.
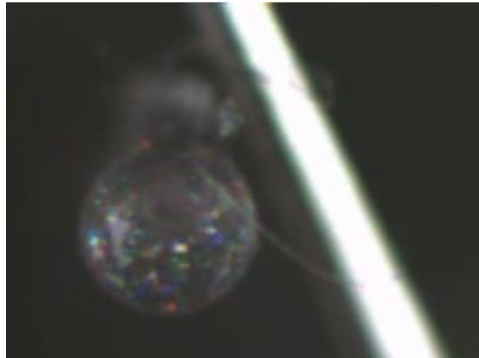
Fig. 25. The moment of hitting a beam with a rod.

Experimental Results:

After the test is completed, Matlab's visual point tracker is used to track the position of the top of the beam over time in the x and y directions for each recording, and the free response of one of the beams is shown in Fig. 26.
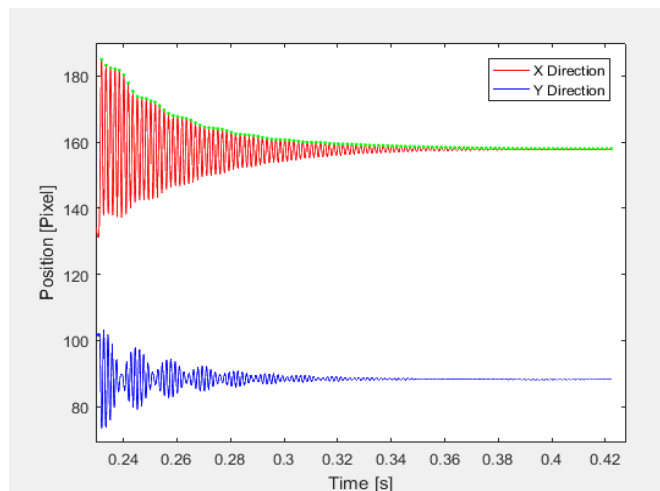
Fig. 26. Beam position in x (top), y (bottom) direction.

The vibration in x direction shows an under-damped second-order system. There are some possible reasons for the beating pattern seen in the y direction; first, there are

multiple modes of vibration. Second, the beam shape is not exactly circular, which makes

the natural frequency different in different directions due to the difference in the area

moment of inertia. This would explain the beating pattern seen, since the natural

frequencies around different bending axes would be close to each other.

Matlab's curve fitting is then used to fit an exponential decay to the x data. Fig.

27 shows the result of the data fitting after offsetting the data a distance of 160.6 pixels to

compensate for the initial position of the beam.
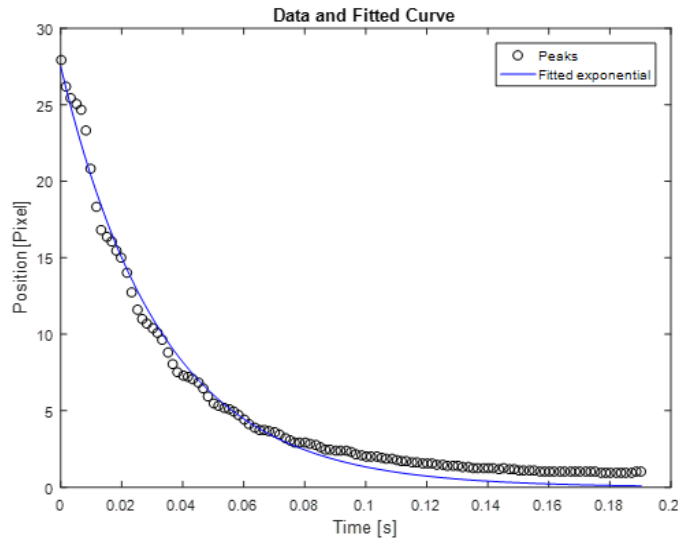
Fig. 27. The exponential decay with compensation.

The fitted equation from the offset data is shown in Eq. (49).

$$f(x) = 187100e^{-38.17x} \qquad (49)$$

The peak values are then used to determine the log decrement δ, which can be

calculated according to Eq. (50), where y_1 and y_2 are two adjacent peaks.

$$\delta = ln\left(\frac{y_1}{y_2}\right) \qquad (50)$$

Table 13 reports the peak values and the calculated log decrement for several

peaks.

Table 13. Calculations for log decrement with data fitting.

Peak Number	Actual Peak Value [pixels]	Fitted and Offset Peak Value [pixels]	Log Decrement from Fitted and Offset Peak Value
1	184.935	26.843	0.063724
2	183.192	25.186	0.063724
3	182.391	23.631	0.063724
4	181.655	22.172	0.063724
5	180.289	20.803	0.063724
6	177.819	19.519	0.063724
7	175.326	18.314	0.063724

The captured data can then be used to determine the damping ratio of PLA using the log decrement method as shown in Eq. (51), where δ is log decrement and ζ is the damping ratio.

$$\zeta = \frac{1}{\sqrt{1+\left(\frac{2\pi}{\delta}\right)^2}} \tag{51}$$

The calculated damping ratio is $\zeta = 0.01$. This was used to design and simulate a 10x10 array of vibratory beams, which is the last plastic material prototype.

5-1-1-4 Experiment 4: Beam Bandwidth and Crosstalk

Considering all the data in Experiment 3, the beam dimensions for the 10th plastic material prototype are designed to see if each beam can be controlled by using the resonant frequency of each beam with less crosstalk.

Research Question:

Does a beam array made of PLA material have sufficiently low crosstalk to make a high-resolution device?

Experimental Setup:

An experiment workstation has been created after the 10th prototype manufacture for better experimentation. The workstation utilizes a speaker capable of producing

frequencies in the audible ranges, and a beam array is attached to the speaker. The speaker selected for initial prototypes is an Uxcell 40 mm-diameter 8Ω, 3W external magnetic speaker. A testbed device is made using a PSoC 5 microcontroller with a digital-to-analog converter output pin connected to a 3W speaker amplifier and utilizing a button keypad and linear potentiometer for input and an LCD display for user output. The testbed device allows the experimenter to set a single frequency for speaker output and observe the vibration response of the prototype beam array. The beam array is attached to the speaker by first removing the speaker diaphragm, then using a custom bracket to connect the beam array directly to the voice coil of the speaker. An image of the testbed and workstation is shown in Fig. 28.
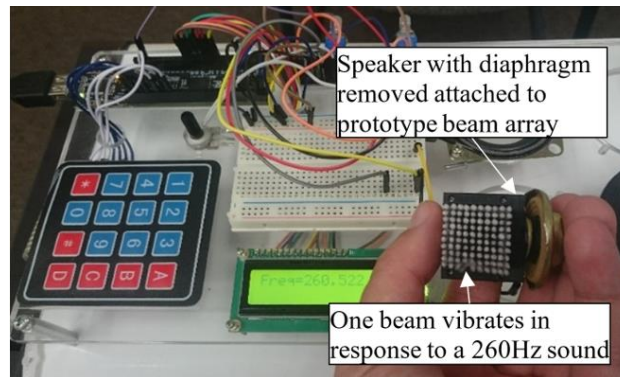
Fig. 28. The 10th prototype beam array and testbed setup in operation. This image shows a single beam vibrating violently in response to a 260Hz excitation.

Experimental Results:

The beam dimension optimization algorithm explained in Chapter 4, Section 4-1, is used to design the final plastic material prototype. The beams selected by the design algorithm are simulated using Matlab in order to compute the lumped mass approximations of the manufactured beams, as given in Eqs. (3) and (10) in Chapter 3, Section 3-1. Fig. 29 shows the simulated amplitude component of the frequency response

for all 100 beams. It shows some differentiation between the peaks, but also some overlap. Ideally, the beam array should be designed so that there is no overlap between peaks. In order to achieve this in future designs, a material with lower damping ratio would be required.
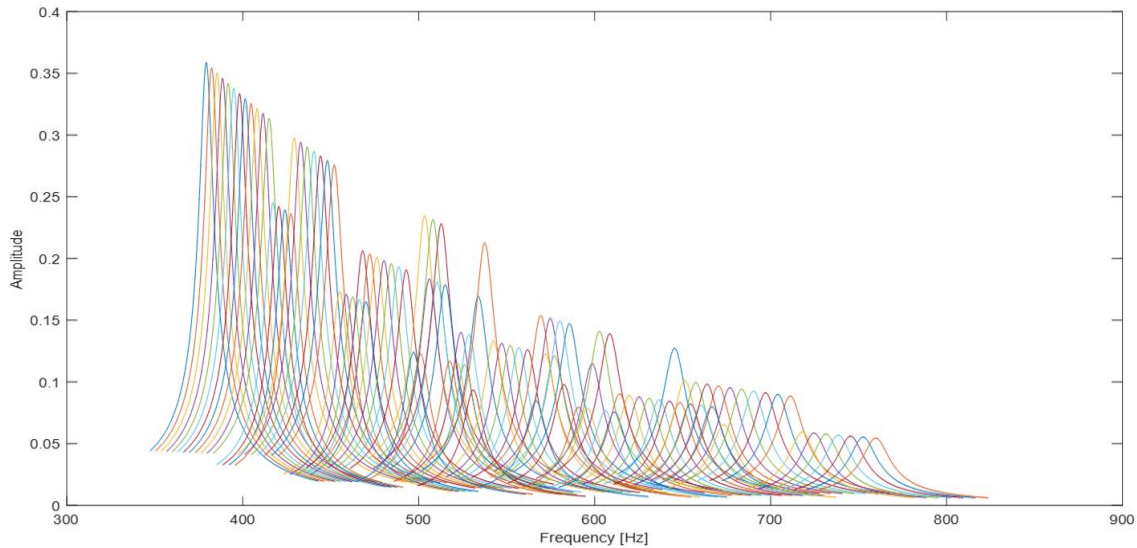
Fig. 29. Amplitude component of the simulated frequency response of the 10x10 PLA beam array.

To validate the simulation result, a forced response experiment using a high-speed camera, the 3rd high speed camera experiment, is conducted. The vibration of the beams in response to the speaker sound can be clearly observed by eye in the experiment. However, significant overlap of vibration between beams is observed, as expected from the amplitude response simulation.

The frequency exciting the observably-vibrating beam is 260 Hz, which is much lower than the natural frequencies that is calculated with the measured diameter of the beams and shown in Fig. 29. In the test shown in Fig. 28, the experimenter's hand is contacting and exerting pressure on the beam base. This may affect the shift in observed resonant frequencies of the beams. In many haptics studies, human skin is modeled as a

spring/damper system. Because of this, the beam array held by a hand can more accurately be modeled as a viscoelastically supported cantilever beam. Kocatürk (Kocatürk 2005) found that a change in beam resonant frequency occurs as a result of a viscous base depending on the diverse frequency parameter and damping parameter. Moreover, the surface of the beams of this prototype is not clear and uniform, and the diameters of the beams along the length is different, as shown in Fig. 30. This non uniform diameter affects the area moment inertia, which affects the frequency of the beams.
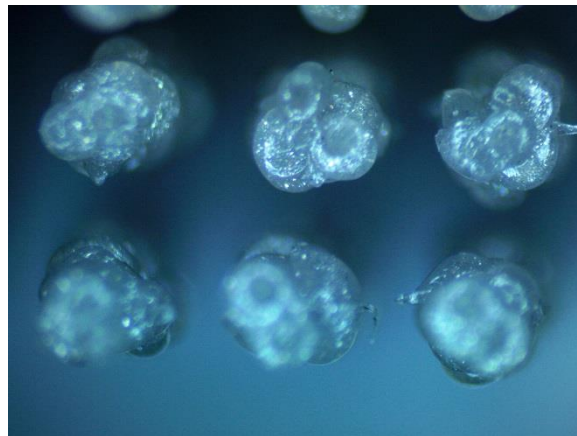
Fig. 30. The image of the 10th plastic prototype via microscope.

5-1-2. Conclusion from Experiments on Polymer Prototypes

Experimentation set 1 consists of two experiments for proof of concept. In the 1st experiment, observation of beam array under sound forcing, a total of 10 plastic prototypes are created and evaluated by simple vibration experiments to check by eye if beams are excited at their resonant frequencies. With some plastic prototypes, beam vibration is observed, but with some other plastic prototypes, no vibration is observed at all. The 2nd prototype showed the best result since it is found that most beams vibrate at resonant frequencies, and the vibration moves along beams by changing the frequency of

oscilloscope. In the 2nd experiment, high speed camera investigation, forced beam vibration on the 2nd prototype is recorded by high speed camera. The first 20 frames are tracked, and the x and y position of a beam over time are obtained. The x and y position show a sinusoidal pattern. The results from the first set of experiments provide proof of the resonant beam vibration concept.

In Experiment 3, an impulse response test for PLA beam is conducted to determine the damping ratio of PLA. The damping ratio of the material is one critical parameter since it affects the resonant frequency and the vibrational amplitude of the beam. A high speed camera is also used to record the impulse response of the beam, and the video is analyzed by a point tracker and curve fitting function of Matlab. From the analyzed data, the damping ratio and log decrement are determined, and they are used for the beam design algorithm.

For Experiment 4, the 10th plastic prototype is designed based on the result of previous experiment. All design parameters such as damping ratio are considered to make a 10x10 PLA prototype. The forced response of the beams is recorded by a high speed camera, and the video is analyzed by a point tracker function in Matlab. The simulation tool is used to simulates the designed beams, and the result is compared to the experimental result. It is found that each beam can be controlled at its resonant frequency, but significant overlap of vibration between beams is observed. To solve this crosstalk problem, a material with lower damping ratio should be considered.

5-2. Experimentation with Metal Material

This section presents the experimental setup and results for the metal prototypes. 5 metal prototypes are manufactured for these experiments, and 6 experiments are

conducted on the prototypes. Each sub-section reports the setup and results of a single experiment.

5-2-1. Experimentation Set 2: Metal Prototypes

There are two possible and available method to manufacture metal prototypes: wire EDM and metal sintering 3D printer. The same models are made by both methods, and the same experiments are conducted with both prototypes in order to figure out which manufacturing method would be better to manufacture long and thin beams in micro scale for my research. For Experiments 5 and 6, Ansys simulation is conducted first, and then the result of the simulation is used to find the resonant frequency of the beams of the 1st and 2nd prototypes. The Ansys simulation is reported in Chapter 6.

5-2-1-1. Experiment 5: Forced Response of EDM Manufactured Prototype

In the experiments with plastic material, it is found that a material having lower damping ratio should be considered for the proposed system to minimize the bandwidth of beams. In Experiment 5, the goal is to prove the vibration beam array concept using metal material prototype and to obtain the resonant frequency of beams made of metal. Research Question:

Can be a metal beam array with smaller bandwidths between beams manufactured by wire EDM so that they can be controlled with less crosstalk? If so, comparing this to the same model made by metal sintering 3D printer, which method would be better to manufacture long and thin micro scale beams?

Experimental Setup:

The 1st metal prototype made of A2 tool steel, which has 9 beams, is manufactured by wire EDM. To test the resonant vibration of the 9-beam prototype of

steel, the base of the beams is connected to a surface transducer with an ethyl cyanoacrylate adhesive, as shown in Fig. 31. The surface transducer is connected to an amplifier, which is connected to a function generator. The function generator is then set to produce a sweep-sine with 5V amplitude from 2100Hz to 2450Hz, in order to include all resonant frequencies found by Ansys simulation in Chapter 6, Section 6-1, over a 2-second time period. A high-speed camera is then positioned to record the beams from the top at a frame rate of 7104 frames per second and a resolution of 256x192 pixels. The selected frame rate provides between 2 and 3 frames per cycle at the resonant frequency of the highest-frequency beam. As the sweep sine is being produced repeatedly, the recording sequence is initiated.
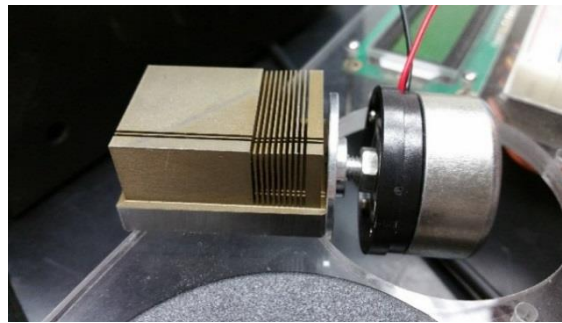
Fig. 31. The 1st prototype of 9-beam row is attached to a surface transducer.

After recording had finished, the video file is loaded into Matlab. The Matlab image processing toolbox 'PointTracker' function, which implements the Kanade-Lucas-Tomasi (KLT), feature-tracking algorithm, is used with a block size of 21 pixels to track the location of the top of each beam over the duration of the sweep sine. Fig. 32 shows one frame captured from the high-speed camera with the Matlab-identified location of the top of each beam. At each frame of the video, the row and column (x and y) location of each beam is recorded.
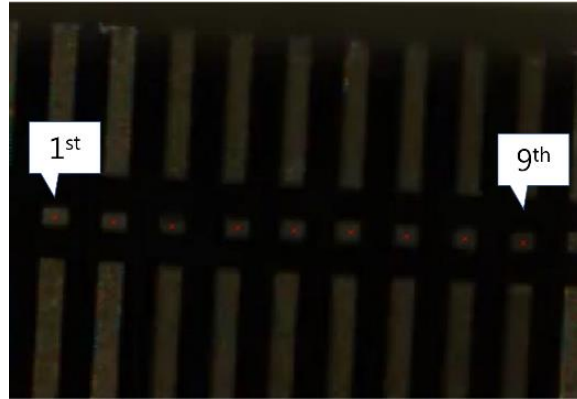
Fig. 32. A high-speed camera image with the Matlab-identified location of each beam marked.

Experimental Results:

The displacement of each beam from its starting location is recorded and is shown in Fig. 33. In the image, the longest beam is on the left and will be referred to as 'beam 1'. The shortest is on the right and will be referred to as 'beam 9'. Fig. 33 shows that the vibrational response of each beam does begin successively with each beam, starting with the beam 1 response reaching a maximum at around 0.1 seconds, and ending with beam 9 reaching a maximum around 1.3 seconds. The function generator is set to produce a sine wave of 2100Hz first and swept it to 2450Hz in 1.5 seconds. Due to using sweep sine wave to resonate beams, it is not possible to figure out the exact frequency value corresponding to time value. It is shown that every beam is resonated at their own resonant frequency, and the vibration response goes to die out to zero as time passes.
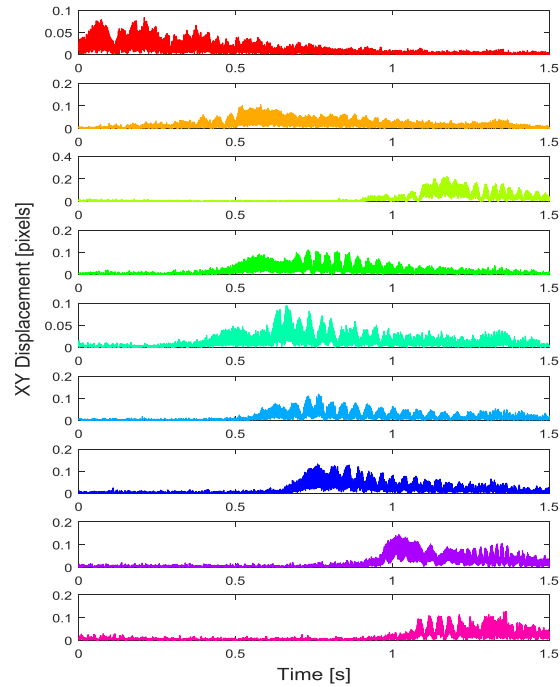
Fig. 33. Displacement of each beam from its starting location during 1.5 seconds of the sweep sine test.

A 'beating' pattern is also observed in the vibration with all beams shortly after the vibration of each beam begins. This beating pattern is due to the superposition of the forced and natural response of each beam as the sweep sine excitation moves above the resonant frequency of the beam before the resonant response has damped out.
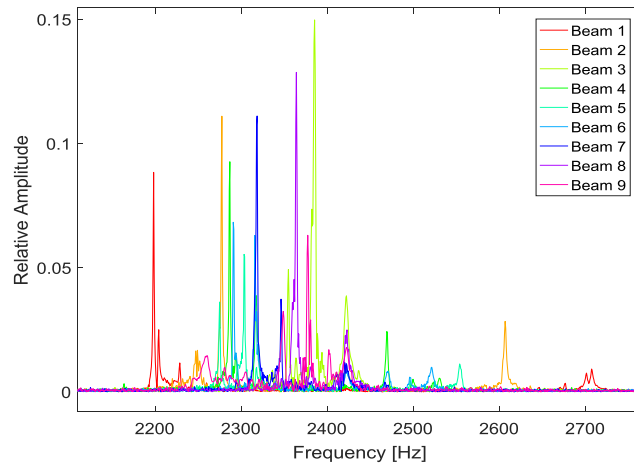
Fig. 34. Frequency components of the response of all nine beams during sweep sine excitation.

A Fourier transform of the data is then computed. Fig. 34 shows the frequency components of the responses of the 9 beams. Fig. 34 shows that the peak resonant frequencies of the beams do not overlap, although there are some secondary peaks which do show up. This confirms that the vibration of a single beam can be actuated by a single frequency independent of the actuation of the other beams. Compared this to the result of Ansys simulation in Chapter 6, Section 6-1, there is small frequency difference such as around 50~60 Hz. This shows the boundary condition difference between Experiment 5 and the Ansys simulation may affect the frequency difference. In the Ansys simulations, one of the side surfaces of the beam base is fixed in this Ansys simulation to express the holding by fingers since the experimenter's hand was contacting and exerting pressure on the beam base in previous experiments with plastic prototypes.

The result of this experiment is compared to the experiment result of the one made by metal 3D printer below in order to select the better manufacture method for metal material for the research.

5-2-1-2. Experiment 6: Forced Response of Sintering Manufactured Prototype

The 9-beam row is made by metal sintering 3D printer to compare the result with the one made by wire EDM. In this experiment, the goal is to obtain the frequency of each beam and to compare the result with the one in Experiment 5 so that the better manufacturing method can be selected.

Research Question:

Can a metal beam array with smaller bandwidths between beams be manufactured by metal sintering 3D printer so that they can be controlled with less crosstalk? If so, comparing this to the same model made by wire EDM, which method

would be better for manufacture of long and thin micro scale beams?

Experimental Setup:

The 2nd metal prototype, which has 9 beams, is manufactured by metal 3D printer. To test the resonant vibration of the 9-beam prototype of steel, the base of the beams is connected to a surface transducer with an ethyl cyanoacrylate adhesive. This prototype could not be set horizontally as was done with the one made by wire EDM, because the base of the sintered array is not massive enough to suspend the transducer. So, the transducer is set on the table with the beam array base protruding vertically, as shown in Fig. 35. Every other aspect of the experimental setup is same as the setup for the 1st metal prototype made by wire EDM, described above, except for the time generating the sweep sine wave. A sweep-sine with 5V amplitude from 2700Hz to 3100Hz, in order to include all resonant frequencies found by Ansys simulation in Chapter 6, Section 6-2, is generated over a 3-second time period.
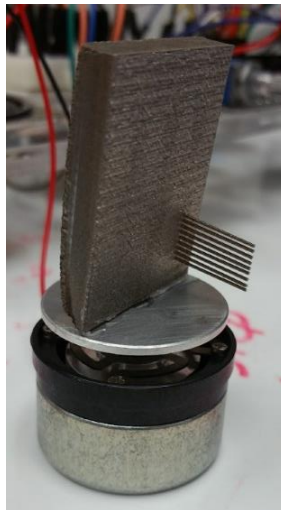
Fig. 35. The 2nd prototype of 9-beam row is attached to a surface transducer.

After recording had finished, the video file is loaded into Matlab. The Matlab image processing toolbox 'PointTracker' function, which implements the Kanade-Lucas-

Tomasi (KLT), feature-tracking algorithm, is used with a block size of 9 pixels to track the location of the top of each beam over the duration of the sweep sine. Fig. 36 shows one frame captured from the high-speed camera with the Matlab-identified location of the top of each beam. At each frame of the video, the row and column (x and y) location of each beam is recorded.
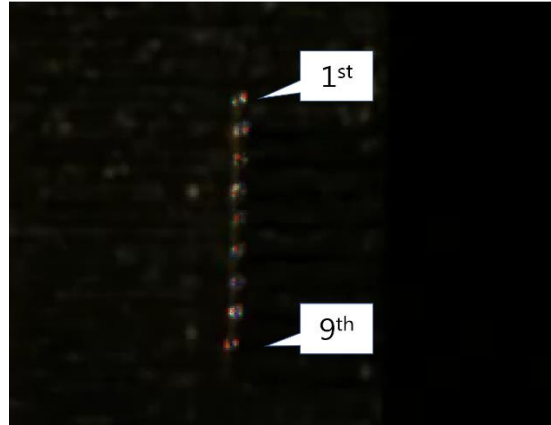
Fig. 36. A high-speed camera image with the Matlab-identified location of each beam marked.

Experimental Results:

The displacement of each beam from its starting location is recorded and is shown in Fig. 37. In the image, the longest beam is on the bottom and will be referred to as 'beam 9'. The shortest is on the top and will be referred to as 'beam 1'. However, no vibration is observed in the frequency range of the sweep from 2700Hz to 3100Hz. Then, the frequency range is changed up to the range from 1800Hz to 2100Hz, and significant beam vibration is observed.

Fig. 37 shows that the vibrational response of each beam does begin successively with each beam, starting with the beam 9 response, the longest, reaching a maximum at around 1.5 seconds, and ending with beam 1, the shortest, reaching a maximum around 2.5 seconds. It is found that some beams vibrate repeatedly 2 seconds after they vibrate,

but their amplitude are different. Due to using sweep sine wave to resonate beams, some beams vibrating are recorded twice in 3 seconds. It is shown that every beam is resonated at their own resonant frequency, and the vibration response goes to die out to zero as time passes.
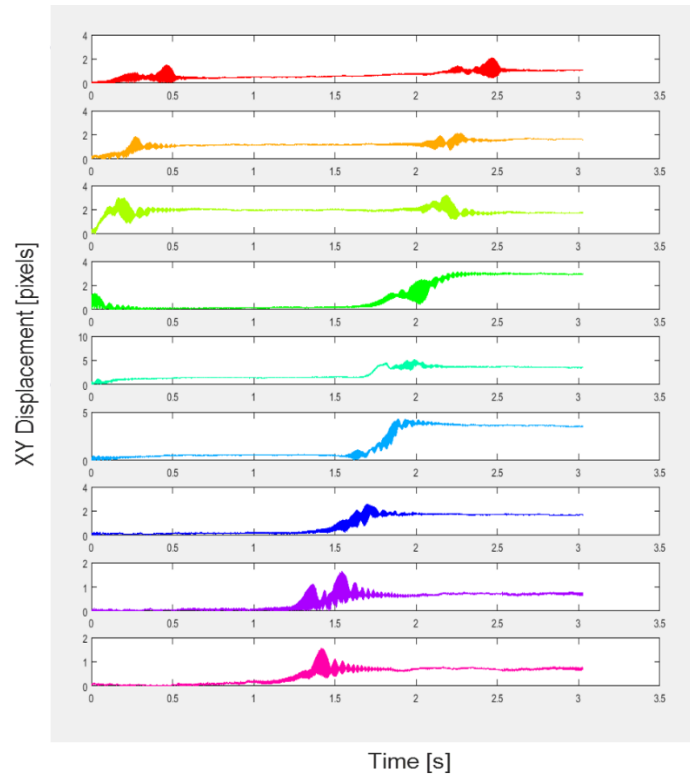
Fig. 37. Displacement of each beam from its starting location during 3 seconds of the sweep sine test.

There are possible reasons for the large vibration frequency range to be shifted. Since the transducer is set on the table with the beam array base protruding vertically, there is a reaction force generated between the contact of the surface transducer and a desk. The desk may work as a spring/damper system for the surface transducer and the beam array, which causes the shift in observed resonant frequencies of the beams. Another possible reason is the unclear cross-sectional area of the beam made by metal 3D printer and area moment of inertia. Due to the square-shaped circular cross-sectional area,

the area moment of inertia of the beam is calculated as the one for rectangular, and this may result in wrong prediction for the resonant frequency of beams. The third possible reason is that the boundary condition using in Ansys simulation and in the experiment are different. In Ansys simulation, one of side surfaces of beam array is fixed, and a certain amount of pressure is applied to the opposite surface. In the experiment, however, no side surface is fixed, and a certain amount of pressure is applied from the surface transducer to a side surface. In the latest research (Wang et al. 2017; Feng et al. 2015; Tan et al. 2017; GIORDANO et al. 1997), it is revealed that the materials of metal 3D printing are in a powder form, and they have different mechanical properties with ordinary metals. During a printing process, the powder material is piled up in layers to build a targeted object, and there are empty spaces between the powders joint due to the size of the powder material. This causes the difference in the elastic modulus and density between the powder form and the block form. The elastic modulus and density of the powder material are even different in every printing process. This difference results in the large frequency shift.

A 'beating' pattern is also observed in the vibration with all beams shortly after the vibration of each beam begins. However, the beating pattern is less clear than the one with wire EDM prototype.

A Fourier transform of the data is then computed. Fig. 38 shows the frequency components of the responses of the 9 beams. Fig. 38 shows that the peak resonant frequencies of the beams do not overlap, although there are some secondary peaks which do show up. This confirms that the vibration of a single beam can be actuated by a single frequency independent of the actuation of the other beams.
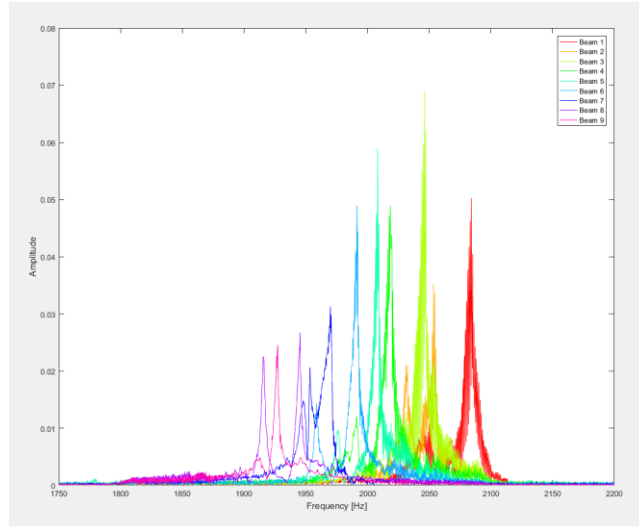
Fig. 38. Frequency components of the response of all nine beams during sweep sine excitation.

5-2-1-3. Result of Comparison between Wire EDM and Metal Sintering 3D Printer

Each experimental result of wire EDM and metal sintering 3D printer shows commonalities and differences. They show each beam can be controlled at a certain resonant frequency of each beam, as shown in Fig. 34 and Fig. 38. However, the beam array made by wire EDM has narrower bandwidth than the one made by metal 3D printer, so each beam of the array made by wire EDM can be controlled more precisely with less crosstalk. This is important for vibratory haptic display device because less crosstalk and narrower bandwidth can allow for more beams in a single array, giving better resolution.

Another problem of metal 3D printer is the frequency range shift. Some possible reasons for it were described above. Table 14 shows the frequency range result in the beam array made by both wire EDM and metal sintering 3D printer. The reasons of the frequency shift are explained more specifically in Chapter 8.

Table 14. Frequency range difference in the beam array made by wire EDM and metal 3D printer.

Wire EDM		Metal Sintering 3D Printer	
Ansys Simulation	Experiment Analysis	Ansys Simulation	Experiment Analysis
2200~2400 Hz	2100~2450 Hz	2700~3100 Hz	1800~2100 Hz

Considering all the experiment results of both wire EDM and metal sintering 3D printer, wire EDM is selected to make further beam array prototypes using metal material.

5-2-2. Experimentation Set 3: Low Frequency Metal Beams and a Contact Plate

Based on the previous experimental results, it is found that the frequency range of beams may be too high since the amplitude of a vibrating beam is small with the tested forcing amplitudes. The frequency and the amplitude of a beam are inversely proportional, as shown in Eqs. (14) and (15), so it is decided to make a new beam array with lower frequency range. After wire EDM is selected to manufacture further metal prototypes for my research, a 5x5 beams array having longer beams as shown Fig. 16 is designed and manufactured to be used in human touch experiments.

5-2-2-1. Experiment 7: Installing a Plate on the Top of Beams contacted to Human Skin

From the previous experiments, it was observed that the user's finger stops beam vibration when touching the tip of beams. To attempt to solve this problem, a plate with a single hole cut for each beam is designed and then manufactured with a micromilling machine, as shown in Fig. 17. The plate is designed so that the tips of the beams protrude through the bottoms of the holes, but not the tops of the holes. In this way, the amount of force that a user can exert on the tips of the beams is limited by the plate.

Research Question:

Can a plate sufficiently limit the force that a user can exert on the beam tips so

that the human skin contact does not inhibit the beam vibration?

Experimental Setup:

The 5x5 beam array is placed and attached on the table by a double-sided tape. In the attempt to fit the holes of the plate to each beam of the beam array, two problems are found in order to install the plate: fitting the beams to the holes of the plate and setting the plate at the same height as the beam tips.

Experimental Result:

During manufacture by wire EDM, the beams deform slightly due to the release of internal stresses and also due to the presence of the water jet. The very small clearance between the edges of the beams and the edges of the holes makes installation of the plate excessively difficult. Thus, this experiment cannot be completed. For this reason, it is determined that future prototypes for initial human experiments must be designed with beams in a row. In that case, the problem of fitting beams could be simplified.

5-2-3. Experimentation Set 4: Low Frequency Metal Beams and a Holding Type

To simplify the problem of the installation of the plate at the same height of the beam tips, an array of 12 beams in a row, the 4th metal prototype, is manufactured by wire EDM. After then, Arizona State University prohibits students from running wire EDM themselves due to some accidents. For this reason, the 4th metal prototype is the last prototype made by wire EDM, which has low resonant frequency range. Therefore, a C-clamp is used to hold the beam array and the surface transducer instead of using an ethyl cyanoacrylate adhesive, in order to avoid damaging the prototype or the surface transducer for future experiments. Additionally, it was observed in earlier experiments with plastic prototypes that exerting a force between the prototype and the speaker

appeared to increase the amplitude of beam vibration. In this experimentation set, this effect will be investigated with the use of the clamp. Fig. 39 shows the holding of C-clamp gripping the 4th metal prototype and the surface transducer.

Fig. 39. The holding of C-clamp

5-2-3-1. Experiment 8: Holding Force Measurement

In this experiment, the goal is to measure the holding force of C-clamp using a force sensor. For the measurement, 3 kinds of force sensors having maximum force range up to 1b (=4.4N), 25 lb (=111N), and 100 lb (=445N) are selected.

Research Question:

Can the holding force of the C-clamp for the beam array and the surface transducer be measured sufficiently with an FSR (force-sensitive resistor) type of sensor?

Experimental Setup:

The force sensor is connected to a PSoC 5 microcontroller with an analog-to digital converter input pin. An LCD display is also connected to the PSoC for user output. The force applied to the force sensor can be shown in the LCD display. Fig. 40 shows one of the force sensors selected for this experiment. The force sensor is placed on the contact area between the surface transducer and the beam array so that the force generating C-

clamp could be measured by the force sensor.
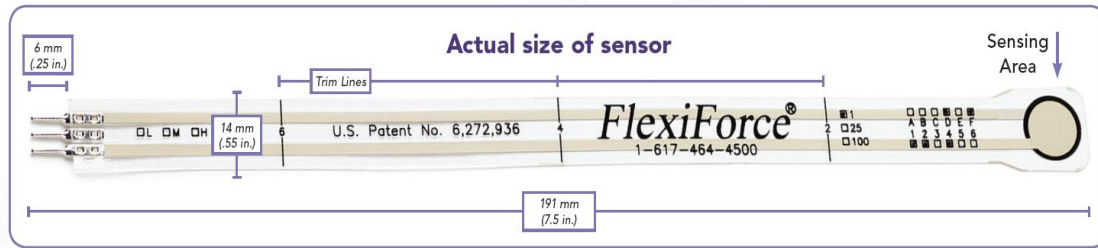
Fig. 40. Image of the force sensor.

Experimental Results:

It is found that the value that the sensor reads depends on the contact area of the force sensor and the object. For example, when the weight of a beam array is measured, the value shown in the LCD display can be different depending on how the beam array contacts the sensing area of the force sensor. When the contact area of the object is larger than the sensing area of the force sensor, the value shown in the LCD display is small. In the opposite way, when the contact area of the object is smaller, the value shown in the LCD display is big. Fig. 41 shows this difference.

It is also found that even though the contact area of the object is smaller than the sensing area of the force sensor, the value shown in the LCD display varies depending on which part in the sensing area a force is applied to.
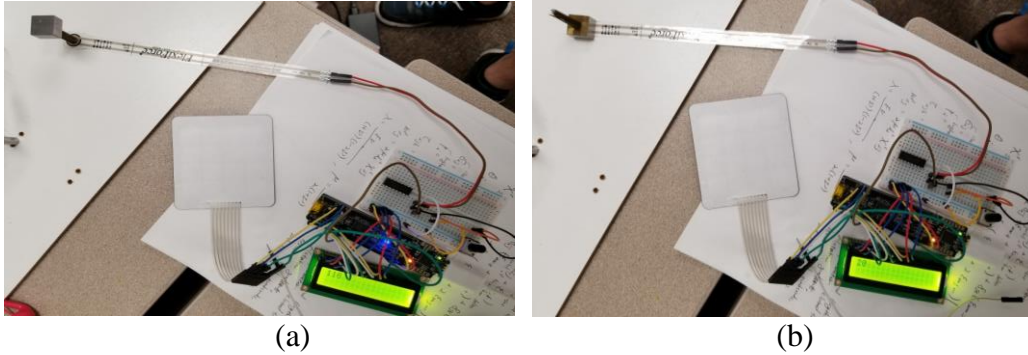
Fig. 41. Image of the contact area effecting on the measured value. (a) When the contact of the object is larger than the sensing area, the value is 20. (b) When the contact of the object is smaller than the sensing area, the value is 116.

For these reasons, this type of force sensor cannot be used to measure quantitatively the holding force of the C-clamp. For future experiments, a different type of force sensor, such as a load cell, should be utilized. For the following experiments, only a qualitative comparison of holding force is attempted.

5-2-3-2. Experiment 9: Three Types of Holding of C-clamp

To figure out how to grip the surface transducer and the beam array by C-clamp in order to maximize the amplitude of beam vibration, three types of holding of C-clamp are tried. Since the force sensor could not be used to measure the force generating from C-clamp, a quantitative method that is found through repeated tests is used.

The three types of holding are: 1. 'Slight holding': C-clamp touches the beam array and the surface transducer but does not exert significant force. 2. 'Normal holding': C-clamp grips the beam array and the surface transducer with sufficiently force that the beam array and surface transducer are not able to slide out of the clamp when the clamp is suspended. 3. 'Tight holding': C-clamp exerts sufficient force that the beam array and the surface transducer cannot be removed by hand without loosening the clamp.

Research Question:

Is the beam vibration amplitude correlated to the holding force between the beam array and the surface transducer?

Experimental Setup:
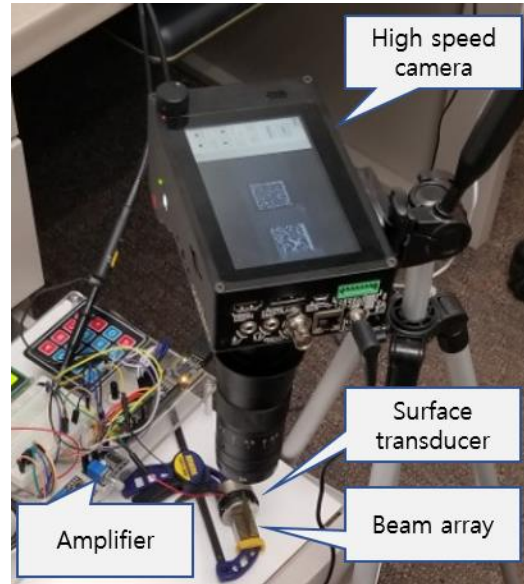
Fig. 42. The experimental setup for three types of C-clamp holding.

A high-speed camera is positioned so that the field of view is perpendicular to the axis of the beams. It is used to record the beam vibration depending on the three types of C-clamp holding. The USB cable from the PSoC is connected to the USB port of the laptop, in order to provide 5V of power to the amplifier. The amplifier power is connected to VDD of the PSoC. Instead of using sweep sine from a certain frequency to another certain frequency for certain period of time, which was used for previous experiments, this time the natural frequency of the first three beams are found by recording the beam vibration while holding the forcing frequency constant, then allowing the vibration to stop, then changing the forcing frequency of the amplifier and recording again. The amplitude dial of the amplifier is adjusted to a small enough amount that the 1st beam does not hit the 2nd beam when the 1st beam resonates. The frame rate of the

camera is set to 8819 frames per second. Fig. 42 illustrates the experimental setup with C-clamp for metal prototypes.

Experimental Results:

The first three beams' vibration responses are recorded and analyzed by an optical flow algorithm implemented in python rather than using the 'Point Tracker' function in Matlab, which implements the Kanade-Lucas-Tomasi algorithm. Due to the beams moving very rapidly in the video files, optical flow algorithm, an algorithm designed for motion detection, performs better than the Kanade-Lucas-Tomasi algorithm, an algorithm designed for static feature detection, as implemented by Matlab.

The total length of all of the video files is about 10 min, which is too long to analyze the beam vibration. This is because 8810 fps (frame per second) that is used to record video files is very high, which requires a lot of time to analyze the video. The code is, then, modified to read only the initial period of frames such as 400 or 800 frames depending on the vibration state and to show the plot of the vibration.

Fig. 43 shows that the vibration response of the 1st beam with 'Normal holding' type at a 461Hz forcing frequency. In the plot, the x label is the frames, and the y label is the beam's movement in the x direction based on the camera coordinates. Three peaks and three troughs are selected randomly, and the average value of them is used to calculate the real amplitude. Table 15 shows the amplitude of the first three beams depending on the holding types, and Fig. 44 shows the comparison of the amplitudes from Table 15.
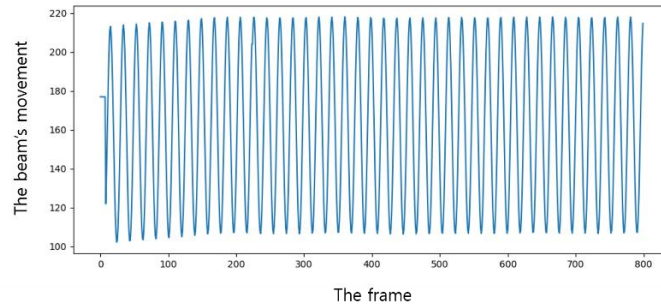
Fig. 43. The 1st beam vibration response with 'Normal holding' at 461Hz.

Table 15. The amplitude calculation depending on holding types.

Holding Type		Average Y value Difference	Actual Height (mm)	Pixel Value	mm/pixel	Amplitude [mm]
Slight Holding	1st beam	51.541	0.568	66	0.0086044	0.444
	2nd beam	30.784	0.617	72	0.0085747	0.264
	3rd beam	24.701	0.667	80	0.0083333	0.206
Normal Holding	1st beam	111.050	0.568	74	0.0076742	0.852
	2nd beam	103.049	0.617	78	0.0079151	0.816
	3rd beam	87.912	0.667	86	0.0077519	0.681
Tight Holding	1st beam	96.118	0.568	75	0.0075719	0.728
	2nd beam	66.402	0.617	76	0.0081234	0.539
	3rd beam	58.353	0.667	87	0.0076628	0.447
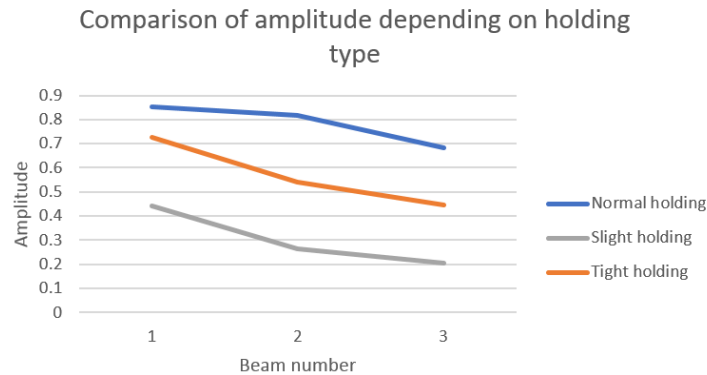
Fig. 44. Comparison of amplitude of first three beams depending on holding type.

Fig. 44 shows that the maximum amplitude of beam vibration is obtained with 'Normal holding' type. This 'Normal holding' type is used for following experiments

using the 4th metal prototype including the human experiment.

5-2-3-3. Experiment 10: Vibration Response with 'Normal holding' Type

In Experiment 9, it is found that 'Normal holing' type is the best to maximize the amplitude of beam vibration. With the 'Normal holding' type, a forced response experiment is conducted to find the resonant frequencies for the beams in an array of 12 beams in a row, the 4th metal prototype.

Research Question:

What is the resonant frequency of each beam of the 4th metal prototype from the forced response experiment?

Experimental Setup:

The same setup in Experiment 9, as shown in Fig. 42 is used for this experiment. Two or three beams are focused in the high-speed camera view every time for high resolution. Since the speed and accuracy of point tracking depend on the resolution of the camera, high frame rate, 8810 fps, is used for the recording. After the targeted beam vibration is recorded, the testbed device is slid over to record other beams. To find the resonant frequency of each beam, the frequency generated from the USB function generator/oscilloscope is changed based on the calculated resonant frequency using lumped mass approximation as shown in Table 10. Several vibration responses around the calculated resonant frequency of each beam are recorded and analyzed in order to determine which excitation frequency corresponds to the maximum amplitude.

Experimental Results:

Table 16 shows the resonant frequency of each beam in the forced response test found by changing the frequency of USB function generator/oscilloscope.

Table 16. The calculated frequency and the resonant frequency in the forced response experiment of the 4th metal prototype.

Peak Number	The Calculated Frequency [Hz]	The Frequency in the Forced Response test [Hz]	The Difference
1	546.97	459	87.97
2	594.63	511	83.63
3	642.10	567	75.10
4	695.68	612	83.68
5	737.24	656	81.24
6	801.64	715	86.64
7	855.54	761	94.54
8	903.30	825	78.30
9	957.20	866	91.20
10	1017.06	915	102.06
11	1065.01	971	94.01
12	1124.67	1010	114.67

Considering the difference between the calculated frequency and the actual frequency appears similar, it is hypothesized that the frequency range is shifted by the difference. There is a possible reason for the vibration frequency range to be shifted. Since the part of C-clamp to grip the object is made of rubber, this may work as a spring/damper system for the beam array, which causes the shift in resonant frequencies of the beams. Considering the similar frequency shift are observed in Experiment 4 and Experiment 6, this assumption would be reasonable. In Experiment 4 and Experiment 6, there are people hand holding the speaker and the beam array, which work as similar as the C-clamp or the desk supporting the surface transducer vertically. In many previous experiments, the frequency shifts are observed only when there is the supporting part that directly contacts the surface transducer to hold. The reason of the frequency difference is revealed in the further research, and the reason is explained in Chapter 8.

The vibration response of each beam is recorded based on the resonant frequency

in the forced response test above and analyzed by an 'Optical flow' algorithm, in python, as described in Experiment 9. Table 17 shows the calculation for the real amplitude of each beam vibration with the 'Normal holding' type. Fig. 45 shows the amplitude of each beam.

Table 17. The amplitude calculation of each beam with 'Normal holding' type.

Beam Number	Average y value Difference	Actual Width (mm)	Actual Height (mm)	Pixel Value	mm/pixel	Real Amplitude (mm)
1st beam	145.882	1.179	0.568	78	0.0072807	1.062
2nd beam	136.135	1.173	0.617	82	0.0075290	1.025
3rd beam	105.750	1.167	0.667	99	0.0067340	0.712
4th beam	74.418	1.173	0.722	94	0.0076839	0.572
5th beam	60.886	1.167	0.765	101	0.0075786	0.461
6th beam	61.572	1.168	0.832	121	0.0068785	0.424
7th beam	47.361	1.155	0.888	122	0.0072809	0.345
8th beam	30.005	1.155	0.938	123	0.0076249	0.289
9th beam	31.109	1.149	0.994	133	0.0074724	0.232
10th beam	22.422	1.162	1.056	142	0.0074364	0.167
11th beam	15.182	1.155	1.106	148	0.0074713	0.113
12th beam	14.120	1.155	1.168	153	0.0076320	0.108
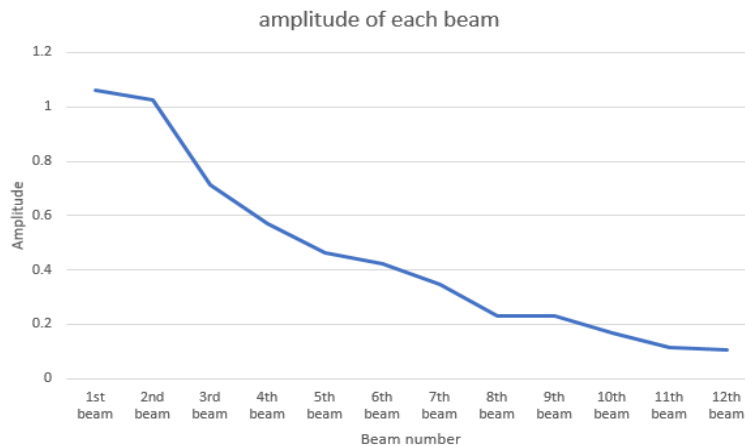
Fig. 45. Amplitude of each beam with 'Normal holding' type.

The amplitude in the table 17 is a relative, not absolute, amplitude. If the experimental conditions change, the amplitude plot might shift up or down, but the

relative amplitude of the vibration of one beam to the vibration of the next will stay the same. This is because the actual amplitude can vary from experiment to experiment if the C-clamp releases the beam array and the surface transducer. If the C-clamp re-grips the beam array and the surface transducer every experiment, the point where the C-clamp grips on them and the holding force applied to them can be different. These changes can cause the different amount of amplitude. Only the absolute amplitude of beams calculated from the same experiment without the misalignment of the beam array and the surface transducer gripped in the C-clamp can be compared relatively. Additionally, the amplitude is calculated from the beam movement in the recording, and this movement is the sum of the movement of beam base and a beam vibration. Moreover, since beam vibrates very fast in the record files, the tracking point in python sometimes can jump to adjacent point during beam vibration, which can also cause minor error in the amplitude of beam vibration.

5-2-4. Conclusion from Experiments on Metal Prototypes

Experimentation set 2 consists of two experiments conducted on metal prototypes: Experiment 5 and 6. These experiments are conducted to compare between wire EDM and metal sintering 3D printing as manufacturing methods for metal microbeam arrays. The same beam array having 9 beams is made by both manufacture methods. High-speed camera experiments are conducted with both beam arrays, and the results are analyzed by point tracker function in Matlab. The experimental results show that each beam of both beam arrays can be controlled at its own resonant frequency. However, the beams in the beam array made by wire EDM can be more precisely controlled with less crosstalk due to the narrower bandwidth. For this reason, wire EDM

is selected to make further metal prototypes for the research.

Experimentation set 3 consists of Experiment 7. In Experiment 7, to make beams having lower frequencies, a 5x5 beam array having a longer length of beams is made by wire EDM. However, all beams are bent due to deformation during manufacture. A plate intended to be placed at the height of the beam tips is considered for a human experiment, but the plate could not be successfully installed the plate due to the small clearance between the hole dimensions and the beam dimensions.

Experimentation set 4 consists of three experiments: Experiment 8, 9, and 10. A beam array of 12 beams in a row, which also has low resonant frequency, is manufactured by wire EDM. In Experiment 8, it is attempted to obtain the holding force of a C-clamp that grips the beam array and the surface transducer using a force sensor. However, it is found that the sensor cannot detect precisely a very small force. The sensor detection varies depending on the contact area of the force sensor and the object. In the 10th experiment, it is attempted to define three types of holding of C-clamp; 'Slight holding', 'Normal holding', and 'Tight holding' in order to maximize the amplitude of beam vibration. It is found that the maximum amplitude of beam vibration is obtained with 'Normal holding' type. In Experiment 10, the 'Normal holding' type is used to obtain the vibration response of each beam of the 4th metal prototype. The resonant frequency of each beam is obtained from the forced response test, and the amplitude of each beam is compared. The reason of the frequency shift is revealed in the further research, and the reason is explained in Chapter 8.

With the experimental result of the 4th metal prototype, human experiments are conducted, and the results are described in chapter 7, Human experimentation.

CHAPTER 6: VIBRATION SIMULATION

In order to successfully design beam arrays, it is necessary to be able to predict the natural frequencies of beams. Two approaches to this goal are to use approximate models, such as the lumped-mass approximation, or to attempt more exact values by using Finite-Element Modeling. This chapter presents the second approach – Finite-Element Modeling – by way of Ansys. Here, an Ansys simulation setup and result is presented for all metal prototypes made by wire EDM and metal sintering 3D printer. Ansys simulations are conducted with 3 metal prototypes to obtain the natural frequency of each beam of those prototypes.

6-1. Ansys Simulation for the 1st Metal Prototype

The Ansys simulation for the 1st metal prototype made by wire EDM is conducted to obtain the resonant frequency range of the prototype.

6-1-1. Ansys Simulation Setup

As shown in Fig. 14, the 1st metal prototype consists of 9 beams manufactured by wire EDM. An Ansys simulation of this prototype is presented here, then a forced response experiment (reported in Chapter 5) is conducted based on this Ansys simulation result. The experimental result is here compared with the Ansys simulation result. The designed dimension of the prototype is shown in Table 6, and the measured dimensions is shown in Table 7.

The measured beam dimensions are used to simulate the vibration of the beams using Ansys software. Fig. 46 shows the model in Ansys and its boundary conditions, and the different cross section of each beam according to the measured dimensions of each

beam. In the experiment, one side of the beam array is exposed to pressure coming from the transducer, and the other side is held by a finger. In the Ansys simulation, the input force is applied to one side of the beam array, and the other side is fixed.

(a)   (b)
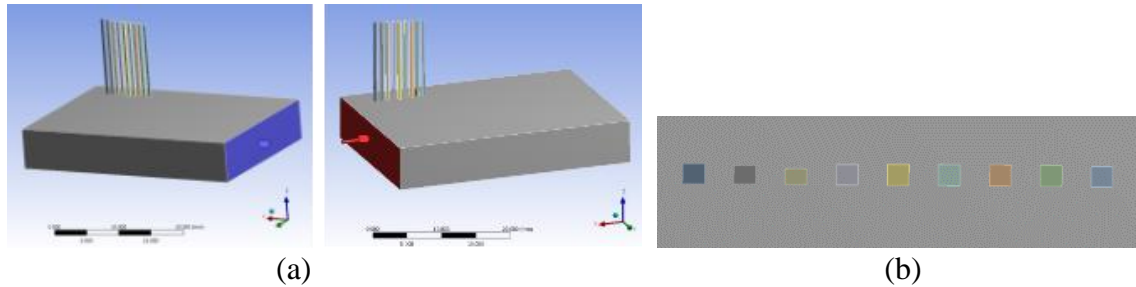
Fig. 46. Illustration of all boundary conditions with the 1st prototype in Ansys simulation. (a) All boundary conditions for the model. (b) Different cross-sectional area of each beam.

6-1-2. Ansys Simulation Result

(a)   (b)
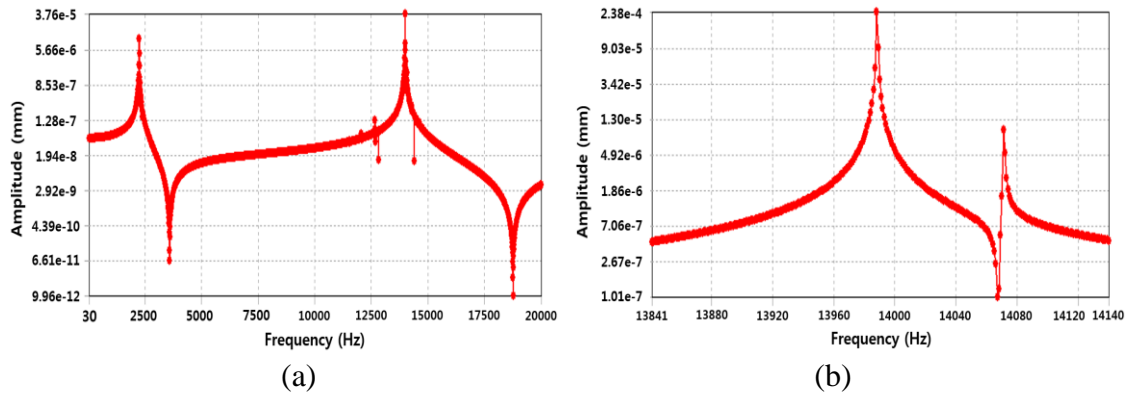
Fig. 47. Vibration simulation of the longest beam of the 1st metal prototype. (a) Vibration in the frequency range 20~20 kHz. (b) Vibration in the frequency range 13840~14140 Hz.

Ansys simulation is conducted with 20~20kHz frequency range, which is the audible frequency range for human beings, and represents the frequency range that can be produced by the speaker in Experiment 5. The vibration of each beam is calculated with 1998 intervals in the 20~20kHz frequency range. Then, the range where the maximum amplitude occurred is simulated again with more defined interval. Fig. 47 shows the vibration of the longest beam in the whole frequency range and the maximum amplitude

range.

In the ANSYS simulation result, it is found that each beam has 2 resonant frequencies; for example, one at a high frequency around 14000 to 14600 Hz and one at a low frequency around 2250 to 2350 Hz for the 1st beam. These two frequencies may correspond to different mode shapes. For Experiment 5, the frequency range from 2250 to 2350 Hz is selected for several reasons: first, lower-frequency mode shapes typically have higher amplitudes. Second, human vibration sensitivity studies have shown higher touch sensitivity to lower vibrational frequencies. Finally, the experiment phase of this research will use a high-speed camera limited to a frame rate of 7104 frames per second. In order to capture the beam vibration at this frame rate, the Nyquist frequency requirement holds that the frame rate must be a minimum of 2x as fast as the beam vibrational frequency. Thus, the high-speed camera will not be able to detect a vibration higher than about 3500Hz. Table 18 reports the 2 resonant frequencies of each beam in the ANSYS model.

Table 18. The resonant frequencies of the 1st metal prototype in Ansys simulation.

Beam Number (Longest)	1st Resonant Frequency (Hz)	2nd Resonant Frequency (Hz)
1st	13988	2243
2nd	14071	2256
3rd	14172	2273
4th	14272	2289
5th	14379	2306
6th	14504	2326
7th	14425	2313
8th	14631	2370
9th	14631	2346

The resonant frequency obtained by Ansys simulation may be a little bit different

than the resonant frequency in the forced response experiment with the 1st metal prototype since one of boundary conditions is different between Ansys simulation and the experiment, which is found when Experiment 5 is conducted. Since in previous experiments with plastic prototypes the experimenter's hand was contacting and exerting pressure on the beam base, one of the side surfaces of the beam base is fixed in this Ansys simulation to express the holding by finger. In Experiment 5 with the 1st metal prototype, however, the beam array is connected to the surface transducer with an ethyl cyanoacrylate adhesive, and it is placed on the testbed, as shown in Fig. 31. It is confirmed after the Experiment 5 that this boundary condition difference rarely affects the frequency range considering very small difference between them as shown in Table 14.

The exact amplitude of the beam vibration in the experiment cannot be predicted in Ansys simulation because the amplitude of the surface transducer is needed for this, but the exact amplitude of the surface transducer is unknown. So, a constant value is used as the amplitude of the surface transducer in Ansys simulation. For this reason, the amplitude in Ansys simulation can be different than the amplitude of the beam vibration in the experiment.

The result of this Ansys simulation is used to conduct the real experiment with the 1st metal prototype. Based on this result, the function generator in the real experiment is set to produce the same frequency ranges of sweep-sine with 5V amplitude, in order to find the actual resonant frequency of each beam. This is termed Experiment 5, and is explained in Chapter 5, Section 5-2-1-1.

6-2. Ansys Simulation for the 2nd Metal Prototype

The Ansys simulation for the 2nd metal prototype made by the metal sintering 3D printer is conducted to obtain the resonant frequency range of the prototype.

6-2-1. Ansys Simulation Setup

As shown in Fig. 15, the 2nd metal prototype having 9 beams is manufactured by the metal sintering 3D printer, and a forced response experiment is conducted based on this Ansys simulation result. The designed dimension of the prototype is shown in Table 8, and the measured dimensions is shown in Table 8.

The measured beam dimensions are used to simulate the vibration of the beams using Ansys software to predict the vibration of the beams as manufactured. In the experiment, one side of the beam array is exposed to pressure coming from the transducer, and the other side is held by a finger. In the Ansys simulation, the input force is applied to one side of the beam array, and the other side is fixed, as shown in Fig. 46.

6-2-2. Ansys Simulation Result

Ansys simulation is conducted with 20~20kHz frequency range, which is the audible frequency range for human beings. The vibration of each beam is calculated with 1998 intervals in the 20~20kHz frequency range. Then, the range where the maximum amplitude occurred is simulated again with more defined interval. Fig. 48 shows the vibration of the longest beam in the whole frequency range and the maximum amplitude range.

| (a) | (b) |
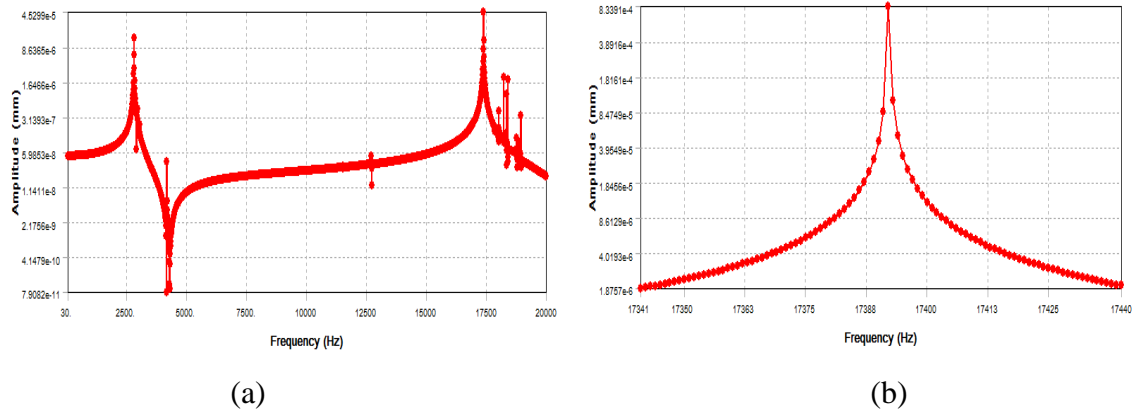
Fig. 48. Vibration simulation of the longest beam of the 2nd metal prototype. (a) Vibration in the frequency range 20~20 kHz. (b) Vibration in the frequency range 17340~17440 Hz.

In the Ansys simulation result, it is found that each beam has 2 resonant frequencies; for example, one at a high frequency around 17340 to 17440 Hz and one at a low frequency around 2750 to 2850 Hz for the 1st beam. These two frequencies may correspond to different mode shapes. For experiment, the frequency range from 2750 to 2850 Hz is selected for several reasons explained in the experiment with the 1st prototype above. Table 19 reports the 2 resonant frequencies of each beam in the ANSYS model.

Table 19. The resonant frequencies of the 2nd metal prototype in Ansys simulation.

Beam Number (Longest)	1st Resonant Frequency (Hz)	2nd Resonant Frequency (Hz)
1st	17392	2797
2nd	18031	2901
3rd	18400	2960
4th	18220	2931
5th	18403	2961
6th	18341	2931
7th	18773	2961
8th	18862	2961
9th	18950	3049

The resonant frequency obtained by Ansys simulation may be different with the

resonant frequency in the forced response experiment with the 2nd metal prototype since one of boundary condition is different between Ansys simulation and the experiment, which is found when the experiment is conducted. Since in previous experiments with plastic prototypes the experimenter's hand was contacting and exerting pressure on the beam base, one of the side surfaces of the beam base is fixed in this Ansys simulation to express the holding by finger. In Experiment 6 with the 2nd metal prototype, however, the beam array is connected to the surface transducer with an ethyl cyanoacrylate adhesive, and it is placed on a table in a vertical direction, as shown in Fig. 35. This difference in boundary condition may result in the difference of resonant frequency. It is confirmed after Experiment 6 that the frequency range obtained from Ansys simulation and the real experiment is very different as shown in Table 14.

6-3. Ansys Simulation for the 3rd Metal Prototype

The Ansys simulation for the 3rd metal prototype, 5x5 beams prototype made by wire EDM, is conducted to obtain the resonant frequency range of the prototype.

6-3-1. Ansys Simulation Setup

As shown in Fig. 16, the 3rd metal prototype having 5x5 beams is manufactured by wire EDM, to conduct an actual vibration experiment based on the result of this Ansys simulation. The designed dimension and the measured dimensions of the prototype is shown in Table 9.

The measured beam dimensions are used to simulate the vibration of the beams using Ansys software to predict the vibration of the beams as manufactured. All boundary conditions in Experiment 7, such as the connection between a surface transducer and the

beam array, is applied for Ansys simulation. Fig. 49 shows the model in Ansys and its boundary conditions, and the different cross section of each beam according to the measured dimensions of each beam. The pressure coming from the transducer is applied to a side surface of the beam base, and another side surface is fixed to express the holding by finger.

(a)   (b)
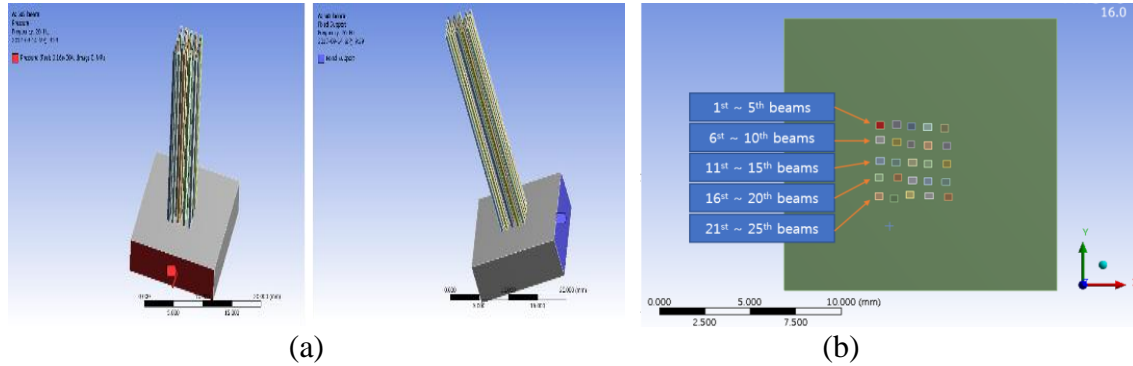
Fig. 49. Illustration of all boundary conditions for the 3rd metal prototype in Ansys. (a) All boundary conditions for the model. (b) Different cross-sectional area of each beam.

6-3-2. Ansys Simulation Result

(a)   (b)
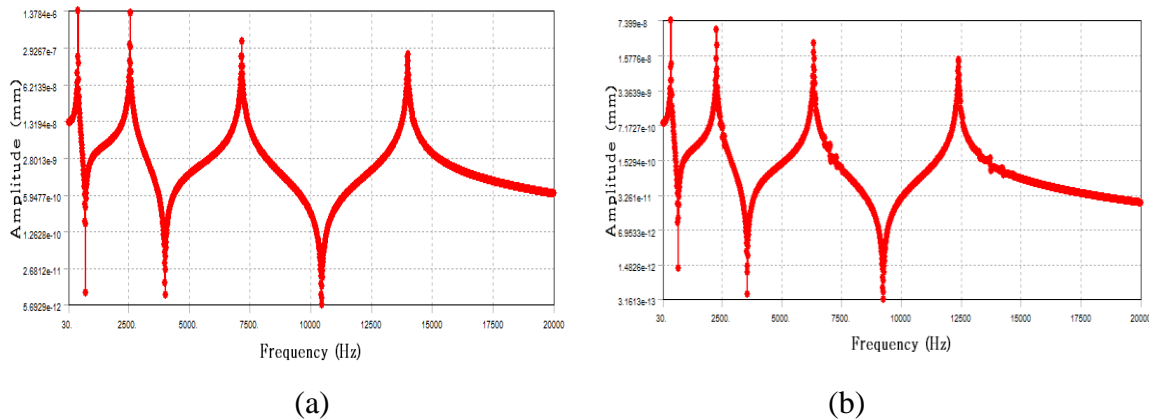
Fig. 50. Vibration simulation of the longest beam of the 3rd metal prototype. (a) Vibration in the frequency range 20~20 kHz. (b) Vibration in the frequency range 13840~14140 Hz.

Ansys simulation is conducted with 20~20kHz frequency range, which is the audible frequency range for human beings. The vibration of each beam is calculated with 1998 intervals in the 20~20kHz frequency range. Then, the range where the maximum

amplitude occurred is simulated again with more defined interval. Fig. 50 shows the vibration response of the longest beam in *x* and *y* direction in the whole frequency range.

In the Ansys simulation result, it is found that each beam has 2 resonant frequencies in *x* and *y* direction; for example, one at a low frequency around 380 to 430 Hz and one at a high frequency around 2300 to 2690 Hz in *x* direction. These two frequencies may correspond to different mode shapes. There are also 2 resonant frequencies of each beam in *y* direction, but it is found that every frequency response of each beam in *y* direction is smaller than the one in *x* direction. For this reason, the frequency response data only in *x* direction are collected. Table 20 reports the 2 resonant frequencies of each beam in *x* direction and the one of smaller frequency range with more defined intervals.

Table 20. The resonant frequencies of the 3rd metal prototype in Ansys simulation.

Beam Number (Longest)	1st Resonant Frequency in *x* Direction [Hz]	2nd Resonant Frequency in *x* Direction [Hz]	The Resonant Frequency on Smaller Range with More Defined Intervals [Hz]
1	410	2560	409
2	2610	420	416
3	2430	390	388
4	2590	410	414
5	2430	390	388
6	2590	410	414
7	400	2510	401
8	2300	370	367
9	2430	390	388
10	380	2380	380
11	400	2510	401
12	430	2690	430
13	400	2510	401
14	400	2510	401
15	2460	390	393

16	400	2490	398
17	2410	380	385
18	410	2580	411
19	2460	390	393
20	2490	400	398
21	390	2450	391
22	400	2490	398
23	390	2440	390
24	410	2580	411
25	2460	390	393

Compared to the result of previous Ansys simulation with the 1st and 2nd metal prototypes, it is found that the resonant frequency range of the 3rd prototype is much smaller.

6-4. Conclusion of Ansys Simulation

With the 1st and 2nd metal prototype, which are made by wire EDM and metal sintering 3D printer, the Ansys simulation are conducted to find the resonant frequency range of each beam. In the experiment, one side of the beam array is exposed to pressure coming from the transducer, and the other side is held by a finger. In the Ansys simulation, the input force is applied to one side of the beam array, and the other side is fixed. The Ansys simulation result with the 3rd metal prototype is not used to conduct the forced response experiment with the prototype since all beams of the prototype are tilled due to manufacture.

In the Ansys simulation with the 1st metal prototype, it is found that each beam has two resonant frequencies in 20~20 kHz frequency range. The 1st resonant frequency of each beam is from 13988~14631 Hz, and the 2nd resonant frequency of each beam is

from 2243~2346 Hz. Due to the frame rate limit of a high-speed camera, the lower frequency range is selected for the forced response experiment with the prototype.

In the Ansys simulation with the 2nd metal prototype, it is also found that each beam has two resonant frequencies in 20~20 kHz frequency range. The 1st resonant frequency of each beam is from 17392~18950 Hz, and the 2nd resonant frequency of each beam is from 2797~3049 Hz. Due to the frame rate limit of a high-speed camera, the lower frequency range is also selected for the real experiment with the prototype.

The 3rd metal prototype, 5x5 beams prototype, is made by wire EDM. This prototype has a longer length than the previous metal prototypes since it is assumed that the resonant frequency of the previous prototypes may be too high for people perception. In the Ansys simulation with the 3rd metal prototype, it is found that the resonant frequency of each beam at a high frequency is from 2300~2690 Hz, and the resonant frequency of each beam at a low frequency is from 367~430 Hz.

Due to the difference in one of boundary conditions between Ansys simulation and the forced response experiments, it is expected that the resonant frequency of metal prototypes can be different. This is confirmed in the result of Experiment 5 and 6, described in chapter 5, Vibration Experimentation.

Since a constant value is used as the amplitude of the surface transducer in Ansys simulation, the amplitude in Ansys simulation and the one in forced response experiments cannot be directly compared.

CHAPTER 7: HUMAN EXPERIMENTATION

This chapter presents the setup and result of 9 human experiments for the proposed device. The 4th metal prototype as shown Fig. 18, which has 12 beams in a row, has been used for the experiment in this chapter. Table 21 shows each experiment and its objective.

Table 21. Human experimentations.

Experiment		Objective
Experimentation Set 5: Direct Finger Touch Experiment	Experiment 11	Dried finger touch to the beam tips
	Experiment 12	Wet and soaped finger touch to the beam tips
Experimentation Set 6: Finger Touch Experiment with a Constraint	Experiment 13	Finger touch experiment with U-shaped constraint
	Experiment 14	Finger touch experiment with L-shaped constraint
	Experiment 15	Finger touch experiment with U-shaped constraint of acrylic panels
	Experiment 16	Finger force measurement with a force sensor and scale
Experimentation Set 7: Finger Touch Experiment with Silicone Rubber Beams	Experiment 17	High-speed camera investigation for the forced response of a beam with silicone rubber beams
	Experiment 18	Vibration response depending on the decrease of silicone rubber beam length
-	Experiment 19	Impulse response of a silicone rubber beam

7-1. Experimentation Set 5: Direct Finger Touch Experiment

The frequency of each beam and 'Normal holding' type of C-clamp, which are found in the forced response experiment, Experiment 10, with the 4th metal prototype, are used to resonate a beam in the prototype with maximum amplitude.

7-1-1. Experiment 11: Dried Finger Touch to the Beam Tips

In many previous experiments, it is found that a user touching the tips of the

vibrating beams is unable to perceive the beam vibration. It is unknown what is the reason for the lack of perception: is the beam vibration amplitude too small for touch perception? Is the vibration frequency too high or low for perception? Or, is there another reason for the lack of perception? In this experiment, a finger touching the beam tips of the 4th metal prototype while the beams are vibrating is recorded with the high-speed camera in order to investigate the reasons for the human lack of perception.

Research Question:

What is the reason for the human lack of perception when touching the tips of the vibrating beams?

Experimental Setup:

The same setup in Experiment 9 is used for this simple finger touch experiment. The experiment is recorded with a high speed camera to analyze it. The only difference is that the camera is positioned so that the field of view is parallel to the axis of the beams. The 1st beam with maximum amplitude is resonated by the surface transducer with the resonant frequency of the beam that is obtained in Experiment 10. At that time, a finger presses the beam tips with various forces to see if there is a moment when the beam does not stop.

Experimental Result:

The recorded video files are checked with eye, and it is found that when the finger touches the beam tip, the amplitude of the vibrating beam decreases, and the beam finally stops. After the finger contacts the beam tips, the beam stops vibrating within about 6-10 milliseconds. This might explain why no beam vibration is perceived.

Fig. 51 illustrates the moment when a finger touches the beam tips. The three

rectangular part vibrating is the first three thinnest beams, and a white object above the three beams is the finger.
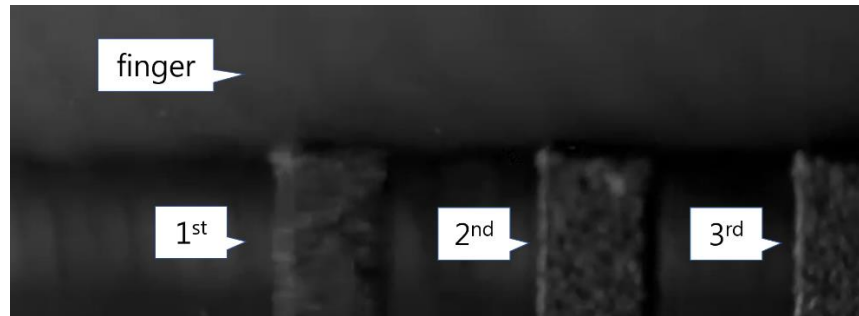
Fig. 51. The image of a dried finger pressing the beam tips.

The reason of the beam vibration stop may be the friction that occurs at the contact surface of beam tips and the finger. Here, the friction is the only force introduced by the presence of the finger that is in the direction of the beam vibration (perpendicular to the beam axis), provided that the skin does not protrude below the surface of the beam tips. If the skin does protrude below the surface of the beam tips, then that skin would exert a normal force in the direction perpendicular to the beam axis. But, from the video captured in this experiment, it is shown that the skin actually does not protrude down. This means that the friction is the only force that could be stopping the beam vibration.

In the following experiments, ways to reduce the friction are investigated.

7-1-2. Experiment 12: Wet and Soaped Finger Touch to the Beam Tips

In Experiment 11, it is revealed that the friction generated at the contact of beam tips and the finger is the probable reason for the beam vibration damping when the finger touches it. Friction is expressed as the product of the coefficient of friction and the normal force exerted by each surface on the other, directed perpendicular to the surface. Thus, there are two possible ways to reduce friction: decrease the coefficient of friction or decrease the normal force. In this experiment, water and soap are used to reduce the

coefficient of the friction.

Research Question:

Can water or soap be used to reduce the coefficient of the friction from the contact of the beam with the finger sufficiently so that contact of the beam with the finger does not significantly damp the beam vibration?

Experimental Setup:

A previous study by O'Meara and Smith reveals (O'Meara and Smith 2001) that the simple presence of soap and water is sufficient to dramatically decrease the coefficient of friction between skin and steel. The same setup and step in Experiment 11 is used for wet and soap finger touch experiment. First, a soaped finger touches the beam tips in a vibrating state, and the vibration response is recorded by a high-speed camera. Then, a wet and soaped finger touches the beam tips, and it is also recorded by the high-speed camera.

Experimental Result:

In the observation of the recorded video files with eye, it is still found that when the finger that is wet or wet and soaped touches the beam tip, the amplitude of the vibrating beam decreases, and the beam finally stops. After the finger contacts the beam tips, the beam stops vibrating within about 6-10 milliseconds. This might explain why no beam vibration is perceived. Fig. 52 illustrates the moment when a wet and soaped finger touches beam tips. The three rectangular part vibrating is the first three thinnest beams, and a white object with bubbles above the three beams is the wet and soaped finger.
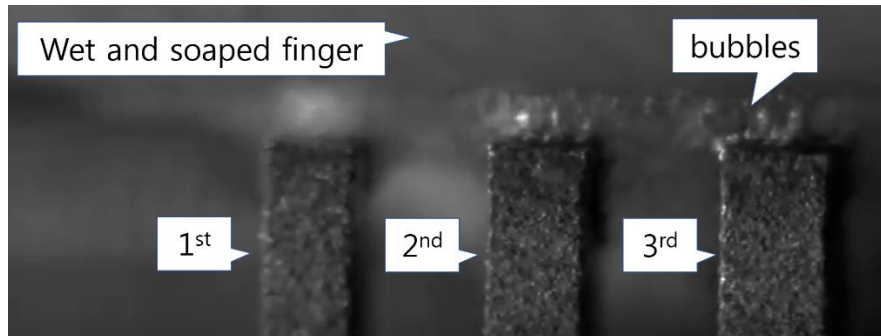
Fig. 52. The image of a wet and soaped finger pressing the beam tips.

7-1-3. Conclusion from Direct Finger Touch Experiment

In many previous experiments, it is found that a user touching the tips of the vibrating beams is unable to perceive the beam vibration. It is unknown what is the reason for the lack of perception. To find the reason, there are three experiments, which is with a dry finger, wet finger, wet and soaped finger, conducted in this Chapter.

In Experiment 11, it is revealed that the friction generated at the contact of beam tips and the finger is the probable reason for the beam vibration damping when the finger touches it. Since friction is expressed as the product of the coefficient of friction and the normal force exerted by each surface on the other, directed perpendicular to the surface, water and soap are used to reduce the coefficient of the friction in Experiment 12.

Regardless of using water and soap to reduce the coefficient of friction, it is found that no vibration is perceived when the finger directly contacts the vibrating beams.

7-2. Experimentation Set 6: Finger Touch Experiment with Constraints

In Experiment 11 and 12, to reduce the coefficient of the friction, several ideas are attempted, but no beam vibration is still detected. In this experiment, a constraint, which has almost same height as the beam tips, is manufactured by a 3D printer to reduce the normal force of the friction.

7-2-1. Experiment 13: Finger Touch Experiment with U-shaped Constraints

Fig. 53. The image of U-shaped constraint.

Previously, a plate was designed and manufactured to limit the normal force that could be exerted on the tips of the beams by a finger by positioning the holes of the plate level with the tops of the beam tips, as given Chapter 4, Section 4-2-2-3. That experiment failed because the small clearance in the plate holes and small manufacturing errors in the beam array prevented the plate from being mounted. In this experiment, a U-shaped constraint is developed to fit around the single-row prototype in order to accomplish the same principle (limiting the normal force exerted by the finger) in a form that is easier to mount. This U-shaped constraint is manufactured by FDM 3D printing, which is an imprecise manufacturing method. Thus, a set of U-shaped constraints are produced at varying heights to allow for experimentation to determine which height is optimal. To find the optimal height of the U-shaped constraint, a total 5 constraints are made with heights from 29.5 mm up to 29.9 mm by increasing 0.1mm, since the layer thickness of the 3D printer is 0.1mm. The set of U-shaped constraints are shown in Fig. 53. The dimension of the channel of the U-shaped constraint is 1.2 mm, which is a little bit larger than the height of the beam in the 4th prototype, as given in Table 10.

Research Question:

When a U-shaped constraint is used to limit the normal force that can be exerted on the tips of the beams by a user, do beams continue to vibrate after being contacted by the skin, and can the user perceive the vibration?

Experimental Setup:

To solve the problem of installing the plate at the same height as beam tips, the U-shaped constraint made of PLA has the similar height with the beam tips. The beams of a beam array are located in the channel of the U-shaped constraint, as shown in Fig. 54.
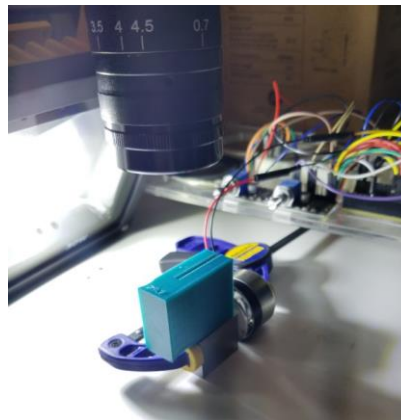
Fig. 54. The image of U-shaped constraint wrapping beams of the 4th prototype.

The same setup in Experiment 10 is used for U-shaped constraint experiment. Every step in this experiment is similar with the one described in Experiment 11, dried finger touch experiment. The sine signal on the function generator is turned on to resonate a beam of the prototype. The frequency of each beam and 'Normal holding' type of C-clamp, which are found in Experiment 10, is used. Since beams do not vibrate when the U-shaped constraint contacts them, a clearance is maintained by using a double sided tape to fix the constraint to the beam base so that the constraint does not touch the beams.

Experimental Result:

With all the 5 of U-shaped constraints, it is found that the U-shaped constraint

with either 29.6 mm or 29.7 mm height are the best to perceive vibration. When using the 29.5 mm height constraint, a finger contacts the beam tips directly since the height of the constraint is not enough to prevent the finger from exerting the normal force to the beam tips. When using the 29.8 mm or 29.9 mm height constraints, the finger cannot touch the beam tips, and no beam vibration is perceived at all since the height of the constraints are too high.

However, there are some problems found in this experiment. First, it is very hard to perceive beam vibration when a finger touches the constraint and the beam tip at the same time. For example, considering the actual length of beams in the 4th prototype is 29.6~29.8mm, when using the constraint having a longer length than the beams, no distinct beam vibration is perceived. Moreover, when using the U-shaped constraint having 29.6 mm or 29.7 mm height, the beam vibration is perceived by tapping the tip of the beams, but it is hard to perceive any distinct beam vibration by just touching the beam tip. It is found that the people skin can recognize an object more easily by applying some amount of pressure.

Another problem is that there is always some vibration transmitted through the U-shaped constraint, and it interferes with recognizing the beam vibration. It would be a challenge to remove or reduce the transmitted vibration in order to increase user perception.

Last, this U-shaped constraint made of green PLA is not a transparent object, so the beam vibration cannot be recorded by a high-speed camera.

7-2-2. Experiment 14: Finger Touch Experiment with L-shaped Constraints

In Experiment 13, a distinct beam vibration is perceived only by tapping the tip of the beams. The reason of this could be that beams still stop vibrate when a finger

touches the beam tips despite of using the U-shaped constraint.

To record the beam vibration with the U-shaped constraint, a constraint made of a transparent material is needed. While making a new U-shaped constraint made of acrylic panel, one side block of the U-shaped constraint that is 29.6 mm height is cut to obtain a L-shaped constraint.

In this experiment, the first research objective is to see if the beam vibration can be perceived while the beam still vibrates. The second objective is to know the optimal height of the constraint, which people can perceive the beam vibration, if the first objective resolves. For the experiment, a finger presses the beam tips very weakly instead of tapping them.

Research Question:

When a L-shaped constraint is used to limit the normal force that can be exerted on the tips of the beams by a user, can the user perceive the vibration by tapping or touching a finger while beams continue to vibrate? If so, what is the optimal height of the constraint?

Experimental Setup:

Every aspect of the experimental setup is same as in Experiment 13, as shown in Fig. 54. The only difference is that a L-shaped constraint is used instead of a U-shaped constraint to record the beam vibration, and the camera is positioned so that the field of view is parallel to the axis of the beams. The frequency of each beam and 'Normal holding' type of C-clamp, which are found in Experiment 10, are also used. The L-shaped acrylic constraints and tape are used to estimate the optimal height of the constraint by adding a single layer of tape between each experimental trial.

Experimental Result:

In this experiment, it is found that beam vibration is perceived while the beam still vibrates through the finger pressing (touching) the beam very weakly. The beam vibration is also perceived by tapping the beam tips with the finger. However, since it is difficult to keep the finger pressing the beam very weakly and constantly, the beam sometimes does stop vibrate. All other beams, the 2nd to 12th beam, are also tested to see if any vibration can be perceived. Unfortunately, no beam vibration is perceived after 4th beam, which the resonant frequency is 612 Hz, even though the finger either presses the beam tip very weakly or taps the tip. There might be two possible reasons for the lack of user perception. One is that the amplitude of the 4th beam may be not enough for the user to perceive the vibration. It is hard to recognize the beam vibration after 4th beam with eye in the forced response experiment. Another reason is that the perceivable frequency range with dynamic touch may be similar to the one with static touch, which is known up to around 500 Hz (Bolanowski Jr et al. 1988). To figure out the exact reason, the further research will be needed.

Next, the L-shaped constraint is used to find the optimal height of the constraint, at which the beam vibration can be perceived. The thickness of a layer of tape is measured by a micrometer, and found to be 0.00285 in = 0.07239 mm. By adding single layers of the tape to the constraint, the total length of the constraint can be adjustable. However, since a layer of the tape can be compressed, the measures of the tape thickness are not very accurate. The constraint made of PLA also has non-uniform and unclear surface. For these reasons, the top surface of the constraint block and the tip of beams are recorded in the side view, and the maximum height difference between them is calculated

using the pixel value in the video files. It is found that the proper length of the constraint is between the beam length and 0.15 mm less than the beam length. In other words, if the length of the beams is 29.6 mm, the length of the constraint should be between 29.45 mm and 29.6 mm.

7-2-3. Experiment 15: Finger Touch Experiment with U-shaped Constraints of Acrylic Panels

A U-shaped constraint made of acrylic panels, which are a translucent material, is manufactured by a laser cutter at Arizona State University.

The laser cutter has a low x/y resolution, so the dimension of several acrylic panels cut is much larger or smaller than the designed dimension. Among the manufactured panels, a pair of about 29.6 mm and a pair of about 29.7 mm acrylic parts are obtained. These are used to make the U-shaped acrylic constraints with a height of 29.6 mm and a height of 29.7 mm.

Research Question:

When a U-shaped constraint of acrylic panels is used to limit the normal force that can be exerted on the tips of the beams by a user, can the user perceive the vibration by tapping or touching a finger, and do the beams continue to vibrate? If so, what is the maximum height of the constraint?

Experimental Setup:

Every aspect of the experimental setup is same as in Experiment 13. The only difference is that a U-shaped acrylic constraint is used instead of a U-shaped constraint of PLA to record the beam vibration, and the camera is positioned so that the field of view is parallel to the axis of the beams. The frequency of each beam and 'Normal holding' type

of C-clamp, which are found in Experiment 10, are also used. The U-shaped acrylic constraints and tape are used to adjust total height of the constraints by adding a single layer of tape between each iteration of this experiment.

Experimental Result:

In this experiment, a finger presses the beam very weakly instead of tapping the beam tips.

With the U-shaped acrylic constraint having 29.6mm height with one layer of tape (= 29.67239mm), as given in Experiment 14, and the U-shaped acrylic constraint having 29.7mm height with one or two layers of the tape (= 29.77239mm or 29.84478mm), beam vibration is perceived by touching the tip of beams very weakly. However, with the U-shaped acrylic constraint having 29.7mm height with four layers of tape (= 29.98956mm), no beam vibration is perceived even though the video file shows the beam is vibrating. This result is similar with the result in Experiment 13 and 14 with U and L shaped constraints.

Even though beam vibration is perceived by touching the beam tip and constraints very weakly, this may not be suitable for the research since it is impossible to maintain the very weak touch with the beams to perceive any beam vibration. It needs to find the way to be able to recognize the beam vibration without touching carefully.

7-2-4. Experiment 16: Finger Force Measurement with a Force Sensor and Scale

In Experiment 15, it is found that with very weak finger touch to the beam tips and constraints, the beam vibration can be perceived. In this experiment, the goal is to measure the maximum finger force that does not stop beam vibration.

Research Question:

Can be the maximum finger force that does not stop beam vibration measured by a force sensor or a scale to quantify the finger force? If so, what is the maximum finger force that can be applied to the beams without stopping the vibration?

Experimental Setup:

There are two simple experiments conducted to measure the finger force.

For the 1st experiment, the same setup in Experiment 13, as shown in Fig. 54 is used with a U-shaped acrylic constraint to figure out the finger force that is applied to the beam tips and constraints. The frequency of each beam and 'Normal holding' type of C-clamp, which are found in Experiment 10, are used. The experimental setup for the force sensor in Experiment 8 is also used. The camera is placed on the side of beams to record beam vibration. The force sensor is placed on a targeted beam tip, which is resonated, and a finger presses the force sensor while the targeted beam vibrates, as shown in Fig. 55.
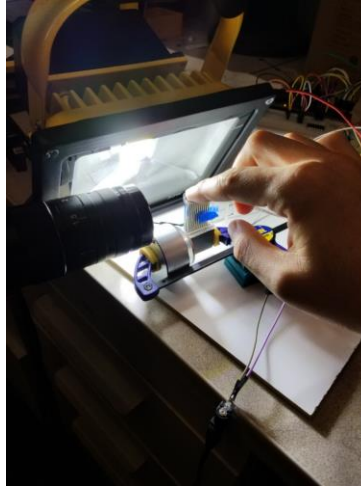
Fig. 55. The image of finger force measurement using a force sensor.

For the 2nd experiment, a scale is used to measure the finger force. First, the C-clamp gripping the surface transducer and the beam array with the acrylic constraint is placed on the scale to measure their weight without a finger press. Then, the vibrating beam tip and constraint are pressed by a finger while the metal beam vibrates, and the

weight caused by the finger force including the whole weight of experimental device is

measured, as shown in Fig. 56.

(a)   (b)
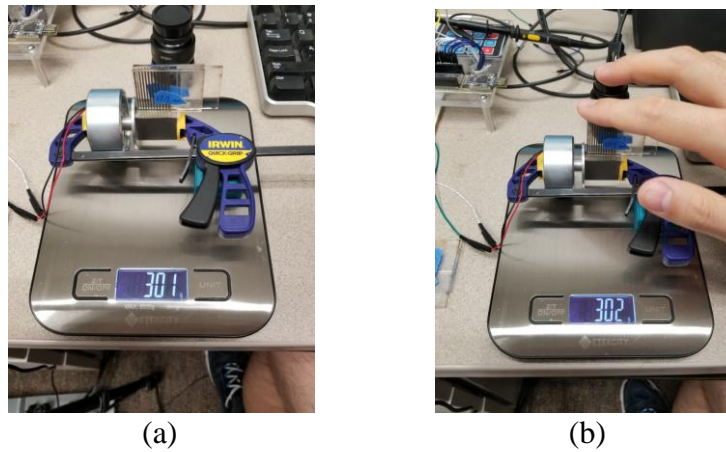
Fig. 56. The image of finger force measurement using a scale. (a) Total weight of whole experimental device without a finger press. (b) Total weight of whole experimental device with a finger press.

Experimental Result:

In the experiment, it is found that the weight caused by the maximum finger

force, which does not stop beam vibration, is less than 1 gram. 1 gram is equal to 0.001

kg, which is 0.001*9.81=0.01 N. This force is too small force to be maintained

continuously when people touch the beam tips.

It is found that other method should be considered to aid the user perception

based on this experiment result.

7-2-5. Conclusion from Finger Touch Experiment with Constraints

To reduce the normal force of the friction and prevent a finger from pressing

beam tips directly, a constraint, having almost same height as the beam tips is considered.

First, A U-shaped constraint is developed and used to conduct a finger touch

experiment. To find the optimal height of the U-shaped constraint, a total 5 constraints

are made with heights from 29.5 mm up to 29.9 mm by increasing 0.1mm, since the layer

thickness of the 3D printer is 0.1mm. It is found in Experiment 13 that it is very hard to perceive beam vibration when a finger touches the constraint and the beam tip at the same time. With the constraint having a little bit smaller length than beams such as 29.6mm or 29.7mm height, the beam vibration is perceived only by tapping the tip of the beams. Another problem is that there is always some vibration transmitted through the U-shaped constraint, which interferes with recognizing the beam vibration. The U-shaped constraint of PLA is not a transparent object, so the beam vibration cannot be recorded.

To record the beam vibration, a L-shaped constraint is made by cutting one side block of the U-shaped constraint with height of 29.6mm. A finger presses the beam very weakly instead of tapping the beam tips to see if the beam vibration can be perceived while the beam still vibrates. It is found that the beam vibration can be perceived with very weak touch while the beam still vibrates, but it is difficult to keep the finger pressing the beam very weakly and constantly. It is also found by adding a layer of tape to the constraint that the proper length of the constraint is between the beam length and 0.15 mm less than the beam length.

A U-shaped constraint made of acrylic panels, which are a translucent material, is manufactured to record the finger touch and beam vibration since the L-shaped constraint could not cover all side surfaces of beams to prevent the direct finger touch. In this experiment, a finger presses the beam very weakly instead of tapping the beam tips. Even though the beam vibration can be perceived, the new method is required to improve the user perception since the very weak finger touch cannot be maintained continuously.

A maximum finger force measurement, which does not stop beam vibration, is also attempted by using a force sensor and a scale. It is found that the weight caused by

maximum finger force, which does not stop beam vibration, is less than 1 gram. This is equal to 0.01 N, and it is too small force that can be maintained when people touch the beam tips.

7-3. Experimentation Set 7: Finger Touch Experiment with Silicone Rubber beams

In previous Experimentation Set 6, it is found that a new method is needed to improve the user perception and to prevent the normal force generating from the direct finger touch to the beam tips. For this, dragon skin 10 very fast is selected to make a silicone rubber beam, which is attached to a beam tip so that a finger could only touch the tips of silicone rubber beams and the normal force of the finger would not exert to the beam tips directly.

7-3-1. Experiment 17: High-Speed Camera Investigation for the Forced Response of a Beam with Silicone Rubber beams

Research Question:

When the normal force generating from a finger is exert on a silicone rubber beam tips attached to the beam tips, can the user perceive the beam vibration through the silicone rubber beam tips?

Experimental Setup:

A and B of 'Dragon Skin 10 very fast' are mixed and solidified. The solidified dragon skin is cut to make rectangular shaped silicone rubber beams. Two silicone rubber beams are attached to the tip of two beams of the 4th metal prototype with an ethyl cyanoacrylate adhesive. The length of silicone rubber beams is 11.7 mm, and their thickness, around 1.1mm, are slightly thicker than the thickness of a beam as given in

Table 10. Since the silicone rubber beams are cut manually, their thickness is not uniform, as shown in Fig. 57. The experimental setup in Experiment 10 is used to resonate the beams to which silicone rubber beams are attached, and a finger touches the silicone rubber beam tip when the beam vibrates in order to perceive the beam vibration. Only two beams with silicone rubber beams attached are resonated. The high speed camera is placed on the side of beams, and it focuses the end of the metal beam to record the vibration of the metal beam.
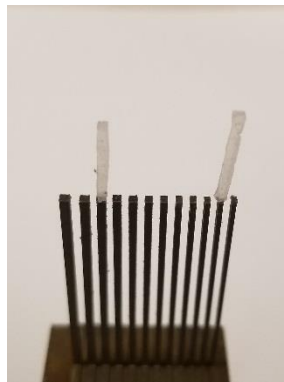
Fig. 57. The 4th prototype and two silicone rubber beams.

Experimental Results:

When the vibration test is conducted with those long silicone rubber beams, no metal beam vibration is observed at around its resonant frequency of the beam found in the force response experiment in Table 10. In general, the amplitude of a 2nd metal beam increases, and beam vibration can be perceived without stopping the vibration, as the silicone rubber beam decreases. After the silicone rubber beam attached to the targeted beam is removed from the beam, the distinct beam vibration is observed at around the resonant frequency. This shows that the long silicone rubber beams absorb the beam vibration, and the amplitude of the beam with the long silicone rubber beams becomes smaller. It is also found that the resonant frequency of the beams can be shifted by

attaching the silicone rubber beams to the beam tips.

Even though the mechanical properties like damping ratio between the silicone rubber beam and metal beam is different, since the total length of beams increases due to adding the silicone rubber beams to the top of beams, the resonant frequency range of the beams are shifted. For example, the frequency of the 1st beam is 511 Hz, and it is shifted to 490 Hz after attaching the silicone rubber beams to the tip of the beams. In the same way, the one of 2nd beam shifted from 569 to 525 Hz, and the 3rd shifted from 612 to 580 Hz, and the 4th shifted from 664 to 620 Hz. The further research will be needed to find the relationship between the beams and silicone rubber beams.

Unfortunately, the resonant frequency range becomes broader after attaching silicone rubber beams, which means the bandwidth of beam vibration becomes broader. For example, the frequency range of the 1st beam is about from 480 to 500 Hz. This can be solved if the length of silicone rubber beams decreases or the rubbers is removed. It is found that cutting the silicon rubber with some increments can affect the frequency shift and the bandwidth of the beam vibration.

7-3-2. Experiment 18: Vibration Response depending on the Decrease of Silicone Rubber Beam Length

In Experiment 17, it is found that there is a frequency range shift and a change in the amplitude of the beam by attaching silicone rubber beams. In this experiment, a total of 46 cases with the silicone rubber beam length changes are investigated, and more than 500 times of a high-speed camera experiment are recorded for every case in order to find the relationship between silicon rubbers and beams.

Research Question:

How does the length of the silicone rubber beam affect the resonant frequency and amplitude of vibration of the metal beams to which they are attached?

Experimental Setup:

Silicone rubber beams manually cut are attached to first five thinnest beams based on the result in Experiment 14 with the L-shaped constraint, in which only the vibration of the first 4 beams can be perceived. Many experiments are conducted with cutting the silicon rubber with an around 1mm increment, and a total of 46 cases with the silicone rubber beam length changes are investigated. The increment for the silicone rubber beam is not constant due to manual cutting. Even though there are some experiments with the same silicone rubber beam length, due to the different cross-sectional dimensions of silicone rubber beams by manual cutting and the misalignment of the beam array and the surface transducer gripped in C-clamp, the results of different experiments cannot be compared – only the results within a single experiment can be compared. Only 2nd beam is resonated, and the vibration response of the 2nd beam is recorded. Since the resonant frequency of the 2nd beam is different depending on the length of silicone rubber beams, the resonant frequency of the beam must be found with eye observation after cutting the silicon rubber with an around 1mm increment every time. Then, about ten frequencies including frequency considered to be resonant frequency are recorded with high speed camera to find the resonant frequency.

The frequency of each beam, which are found in Experiment 9, and 'Normal holding' type of C-clamp are used. The experimental setup for the high speed camera and function generator in Experiment 9 is also used, and Fig. 58 shows the silicone rubber beams attached to the first five thinnest beams.
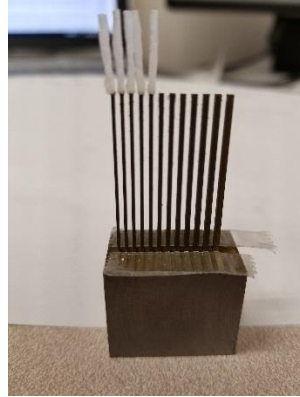
Fig. 58. The silicone rubber beams attached to the first five thinnest beams.

Experimental Results:

The recorded vibration response of the 2nd beam is analyzed by the algorithm, 'Optical flow', in python instead of using 'Point Tracker' function in Matlab, because all video files are recorded in vibrating state not stationary state in this experiment.

The vibration response of the 2nd beam is analyzed depending on the length change of the silicone rubber beams. All experiment results in this experiment are described in Appendix B. For example, Table 22 shows the calculation for the real amplitude of the 2nd beam when all silicone rubber beam lengths are 3.4 mm, and Fig. 59 shows the amplitude of the 2nd beam depending on frequency changes. It is shown that when the silicone rubber beam length is 3.4 mm, the 2nd beam's resonant frequency is 498 Hz.

Table 22. The amplitude calculation of the 2nd metal beam when the 2nd silicone rubber beam length is 3.4mm.

Frequency (Hz)	Average Y value Difference	Actual Width [mm]	Actual Height [mm]	Pixel Value	mm/pixel	Real Amplitude [mm]
475	3.191	1.173	0.617	64	0.0096465	0.0308
480	4.060	1.173	0.617	64	0.0096465	0.0392
485	5.380	1.173	0.617	64	0.0096465	0.0519
490	8.060	1.173	0.617	64	0.0096465	0.0778

495	17.173	1.173	0.617	64	0.0096465	0.1657
496	22.109	1.173	0.617	64	0.0096465	0.2133
497	27.401	1.173	0.617	64	0.0096465	0.2643
498	29.549	1.173	0.617	64	0.0096465	0.2850
499	23.744	1.173	0.617	64	0.0096465	0.2290
500	17.661	1.173	0.617	64	0.0096465	0.1704
505	6.375	1.173	0.617	64	0.0096465	0.0615
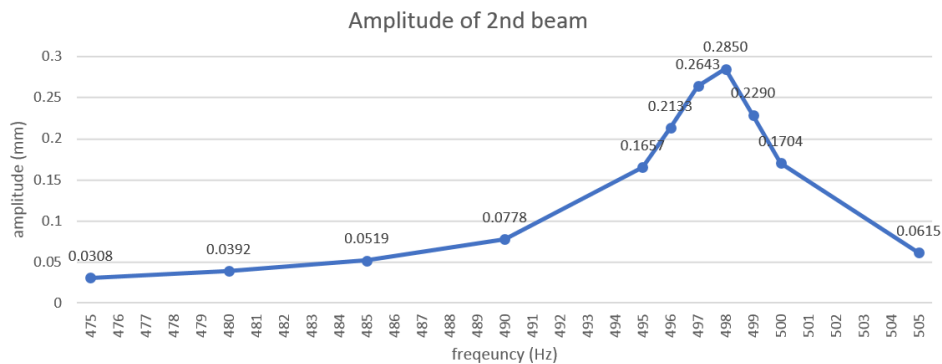
Fig. 59. Amplitude of the 2nd beam when the 2nd rubber beam lengths is 3.4mm.

After all video files are analyzed, there are several things found in this experiment.

(1) There are certain lengths of the silicone rubber beams for which the 2nd metal beam vibrates with much lower amplitude. For example, when the silicone rubber beam length is about 10.3~10.7mm, 5.6~6.7mm, or 2.1mm, the amplitude of the beam vibration is greatly decreased. These lengths could be different in another experiment since the surface of the rubber beams is not homogenous and uniform, and their thickness is not constant due to the error caused by manual cutting. Fig. 60 (b) and (f) illustrate these cases where the resonant frequency of the metal beam cannot be observed because the amplitude of vibration is very small at all frequencies.

Fig. 60. Amplitude of the 2nd metal beam when the five rubber beams have the lengths: (a) (12.0, 12.0, 12.0, 12.0, 12.0mm). (b) (10.7, 10.7, 10.7, 10.7, 10.7mm). (c) (9.6, 9.6, 9.6, 9.6, 9.6mm). (d) (8.5, 8.5, 8.5, 8.5, 8.5mm). (e) (7.6, 7.6, 7.6, 7.6, 7.6mm). (f) (6.7, 6.7, 6.7, 6.7, 6.7mm).

(2) Between the two certain lengths, the amplitude of beam vibration becomes larger and then becomes smaller after a certain silicone rubber beam length. Fig. 60 shows the frequency response of the 2nd metal beam depending on the silicone rubber beam length. Table 23 also shows the amplitude difference of the 2nd metal beam depending on the silicone rubber beam lengths.

(3) The resonant frequency of the 2nd metal beam trends towards the resonant frequency of the beam without the silicone rubber beam, as the silicone rubber

beam length becomes shorter. However, when the amplitude of vibration of the metal beam is very small due to the length of the silicone rubber beam, the resonant frequency becomes very different than it was without the rubber beam, which can be seen by comparing each image in Fig. 60. Table 23 shows the frequency difference of the 2nd metal beam depending on the silicone rubber beam lengths.

(4) When the silicone rubber beam length is longer than 10mm, the maximum amplitude and resonant frequency of the steel beam cannot be determined.

(5) When the silicone rubber beam length is shorter than 2mm, the vibration of the beam becomes more difficult to perceive by touch.

(6) Silicone rubber beams may absorb the beam vibration from other metal beams. For example, there are 4 silicone rubber beams attached to the 2nd to 5th beams, and there is no silicone rubber beam attached to the 1st beam. When a silicone rubber beam is attached to the 1st beam, the amplitude of 2nd metal beam decreases significantly, which can be seen by comparing Fig. 61 (a) to Fig. 61 (b).

(7) If the length of the 2nd rubber beam is different than the lengths of the other rubber beams, then the frequency response of the 2nd metal beam is very different than it is when every rubber beam has the same length, as seen by comparing Fig. 61 (b) and (c).

(8) Three experiment sets are performed to find the silicone rubber beam length that maximizes the vibrational amplitude of the 2nd metal beam. In these three experiments, the optimal rubber length is found to be 4.3, 4.6, 3.4mm.

(9) If the difference in length between the 2nd rubber beam and other rubber beams is small, and the length of the 2nd rubber beam is around the length with the maximum amplitude, the vibration result is similar with the case of all silicone rubber beams with the same length. For example, if the difference in the length between the 2nd rubber beam and other rubber beams is around 0.6mm, and the length of the 2nd rubber beam is 3.4 mm, the maximum amplitude and resonant frequency of the 2nd metal beam in both cases are about the same. But the bandwidth is smaller in the case of every beam having same length of silicone rubber beams, as shown in Fig. 62.

Based on these results, it is hypothesized that the silicone rubber beam has its own resonant frequency, so when the resonant frequency of the silicone rubber beam is similar to the resonant frequency of the metal beam, the amplitude of metal beam vibration is smaller.

Table 23. The amplitude and resonant frequency of the 2nd metal beam difference depending on the silicone rubber beam lengths in an experiment set.

Five Rubber Beam Lengths [mm]	Amplitude of the 2nd Metal Beam [mm]	Resonant Frequency of the 2nd Metal Beam [Hz]
(12.2, 12.2, 12.2, 12.2, 12.2)	0.0946	494
(10.7, 10.7, 10.7, 10.7, 10.7)	0.0276	Not observable
(9.6, 9.6, 9.6, 9.6, 9.6)	0.0854	480
(9.6, 8.5, 9.6, 9.6, 9.6)	0.2490	496
(8.5, 8.5, 8.5, 8.5, 8.5)	0.2518	495
(8.5, 7.6, 8.5, 8.5, 8.5)	0.1509	502
(7.6, 7.6, 7.6, 7.6, 7.6)	0.1467	502
(7.6, 6.7, 7.6, 7.6, 7.6)	0.0437	505
(5.6, 5.6, 5.6, 5.6, 5.6)	0.0278	Not observable
(5.6, 4.6, 5.6, 5.6, 5.6)	0.1505	485
(4.6, 4.6, 4.6, 4.6, 4.6)	0.1332	484
(4.6, 4.0, 4.6, 4.6, 4.6)	0.2601	490

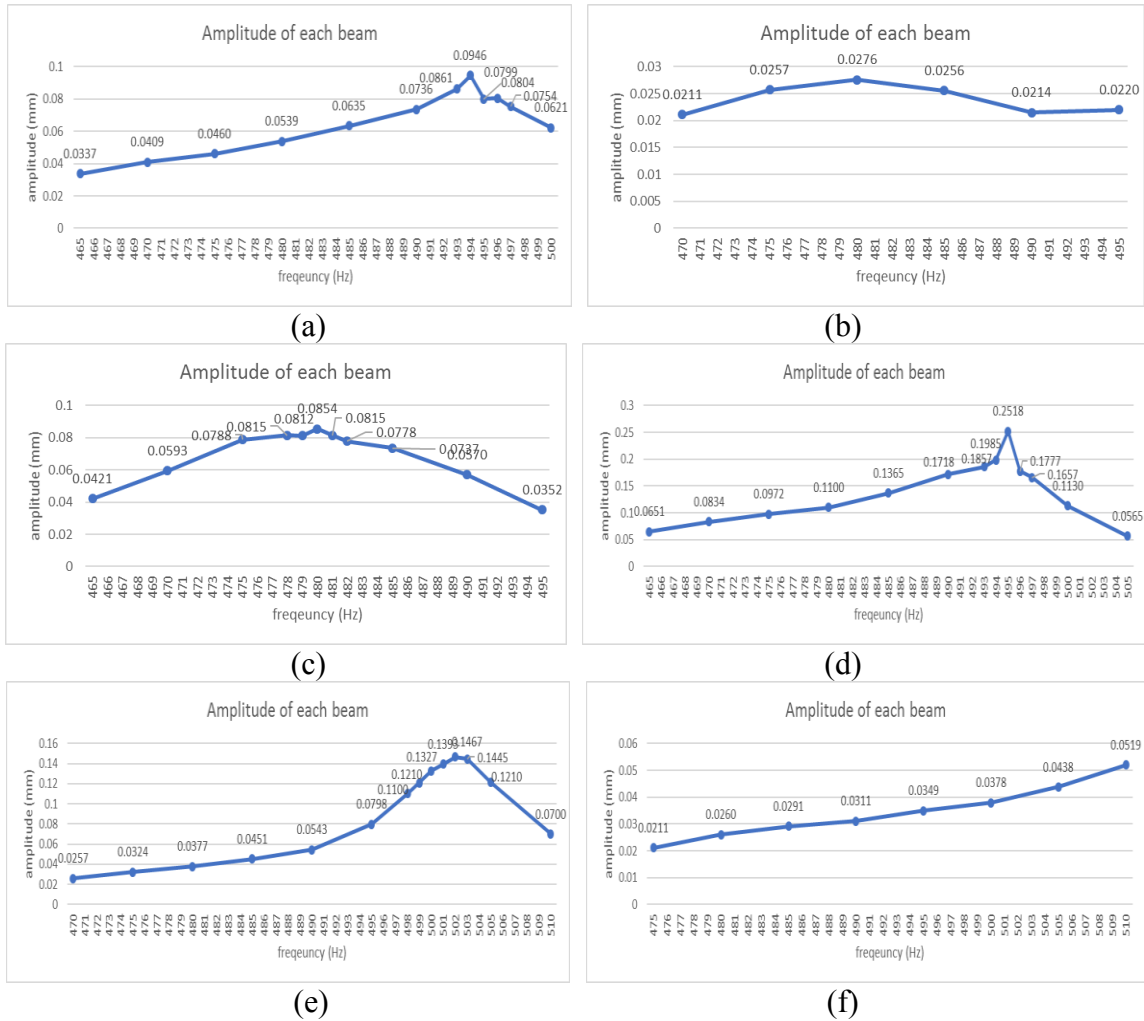| (3.4, 3.4, 3.4, 3.4, 3.4)	0.2850	498

(a)

(b)

(c)
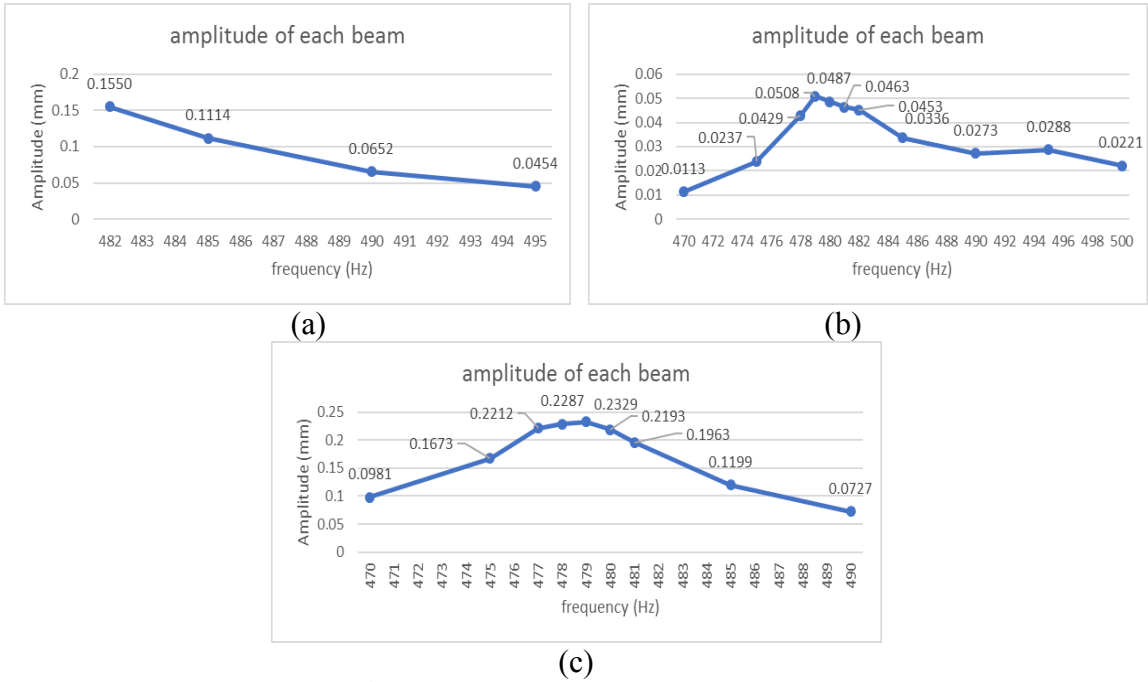
Fig. 61. Amplitude of the 2nd metal beam when the five rubber beams have the lengths: (a) (0, 4.3, 11.8, 11.8, 11.8mm). (b) (11.8, 4.3, 11.8, 11.8, 11.8mm). (c) (4.3, 4.3, 4.3, 4.3, 4.3mm).

(a)

(b)
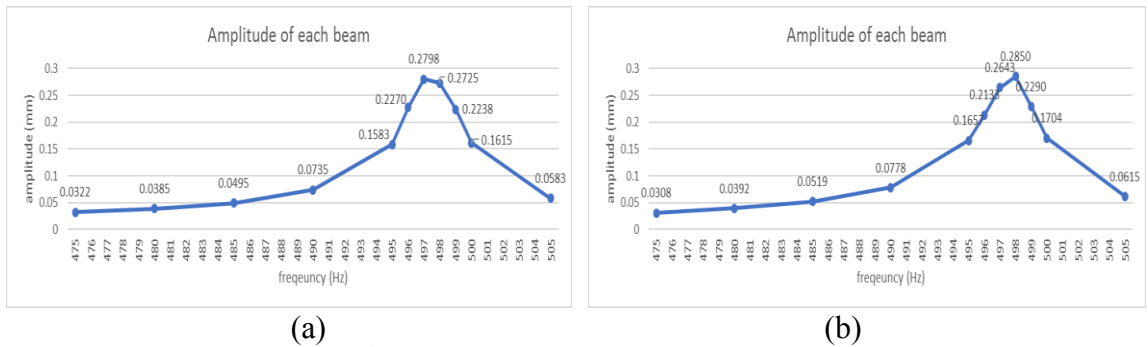
Fig. 62. Amplitude of the 2nd metal beam when the five rubber beams have the lengths: (a) (4.0, 3.4, 4.0, 4.0, 4.0mm). (b) (3.4, 3.4, 3.4, 3.4, 3.4mm).

7-3-3. Experiment 19: Impulse Response of a Silicone Rubber Beam

In order to find the material properties of a silicone rubber beam, an impulse

response experiment is conducted. The damping ratio of the material is one critical

parameter since it affects the difference between the natural and resonant frequencies, and also has a significant effect on the vibrational amplitude of a beam. The damping ratio is needed to conduct a numerical analysis of the relationship between metal beams and silicone rubber beams.

Research Question:

What is the damping ratio of a beam made of silicone rubber?

Experimental Setup:

For this experiment, the dragon skin 10 very fast is selected to make a silicone rubber beam. The silicone rubber beams are attached to the beams of the 4th metal prototype for this experiment, as shown Fig. 57. The silicone rubber beam is cut manually, and it does not have a precise uniform surface. This is important since a non-uniform surface can affect the area moment of inertia, the main vibration direction, natural frequency, log decrement and damping ratio. In this experiment, the silicone rubber beam is considered to have 1.1mm in width and height and to have 10.3mm in length.

An impulse test is then performed to determine the damping ratio of the silicone rubber beam. The top of the beam is placed within view of a high-speed camera, and a small metal rod is used to 'flick' the beam, thus exciting the beam's natural frequency. The resulting vibration of the beam is recorded at 4023 frames/s. For easy tracking, a black marker is used to mark the beam tip. Fig. 63 shows one frame of the high-speed camera impulse test.

Fig. 63. The moment of hitting a beam with a rod.

Experimental Results:

After the test is completed, Matlab's visual point tracker is used to track the position of the top of the beam over time in the x and y directions. Fig. 64 shows the results.
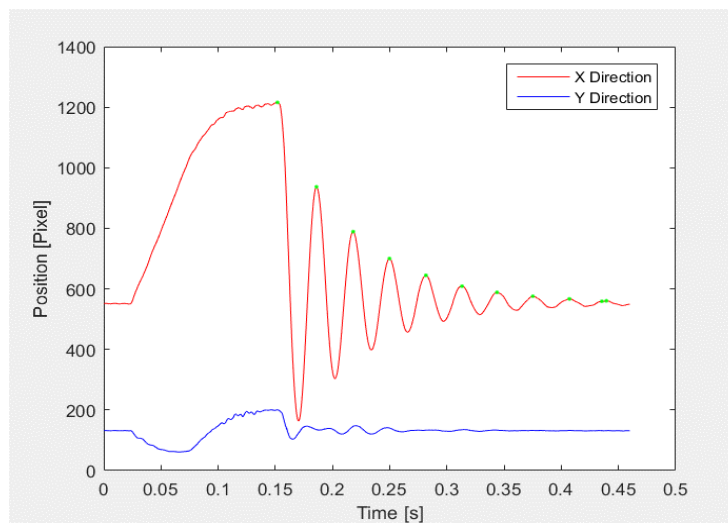
Fig. 64. Beam position in x (top), y (bottom) direction.

The X vibration shows the response as an under-damped second-order system. Since the beam is flicked almost in one direction, the beam slightly vibrates in the y direction.

Matlab's curve fitting is then used to fit an exponential decay to the x data. Fig. 65 shows the result of the data fitting after offsetting the data that is a distance of 599.1

1 2 9

pixels to compensate for the initial position of the beam.
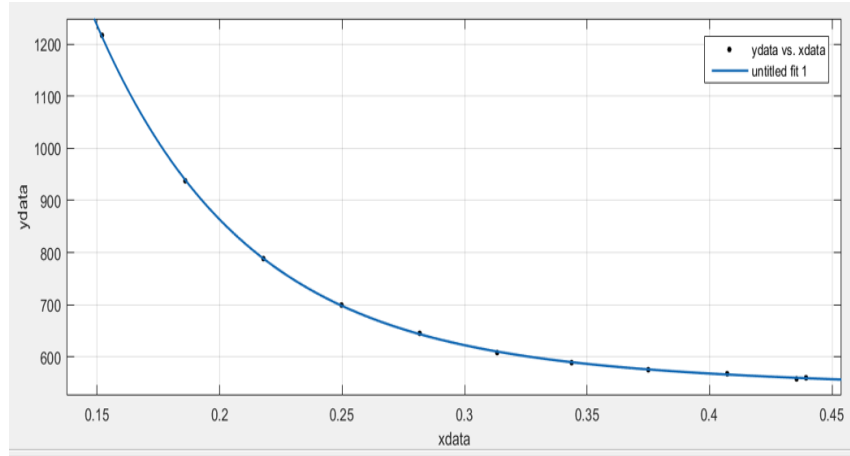
Fig. 65. The exponential decay with compensation.

The fitted equation from the offset data is shown in Eq. (52).

$$f(x) = 7765e^{-16.52x} \tag{52}$$

The peak values are then used to determine the log decrement δ, which can be

calculated according to Eq. (50), where y_1 and y_2 are two adjacent peaks.

Table 24 reports the peak values and the calculated log decrement for several

peaks.

Table 24. Calculations for log decrement with data fitting.

Peak Number	Actual Peak Value [pixels]	Fitted and Offset Peak Value [pixels]	Log Decrement from Fitted and Offset Peak Value
1	1215.604	631.677	0.527158
2	936.882	372.867	0.527158
3	789.135	220.096	0.527158
4	700.171	129.918	0.527158
5	644.634	76.688	0.527158
6	608.865	45.268	0.527158
7	588.331	26.721	0.527158

The captured data can then be used to determine the damping ratio of the silicone

rubber beam using the log decrement method as shown in Eq. (51), where δ is log

decrement and ζ is the damping ratio.

The calculated damping ratio is $\zeta = 0.0836$. This is used to make a numerical model to compare the result with the experimental result.

7-3-4. Conclusion from Finger Touch Experiment with a Silicone Rubber Beam

The new method using a silicone rubber beam to prevent a finger from pressing the beam tips directly is proposed. Dragon skin 10 very fast is selected to make silicone rubber beams, and they are attached to the beam tips for the experiment.

Only 2 silicone rubber beams are attached to the beam tips to conduct an experiment to see if the normal force exerting by a finger to the silicone rubber beam tips can affect the metal beam vibration. Through the forced response test with the high-speed camera investigation, beam vibration is observed and perceived without stopping the beam vibration. The shift in the resonant frequency range of beams is also observed.

To find the relationship between the beams and silicone rubber beams attached to the beams, hundreds of vibration response experiments are conducted with high-speed camera to record the 2nd metal beam vibration. Several features are observed in the experiments, and it is described in Section 7-3-2.

Base on the result, it is hypothesized that the silicone rubber beam has its own resonant frequency and harmonic cycle, and when it is similar with the one of beam targeted, beam seems not vibrating.

To conduct a numerical analysis to compare the result with the experimental result, an impulse response experiment is conducted. The material properties of the silicone rubber beam such as the damping ratio is calculated, and it was 0.0836.

CHAPTER 8: EVALUATION OF ERROR SOURCES AND SIZE EFFECT OF MICRO-MESOSCALE STEEL BEAMS

In previous experiments with plastic and metal prototypes, it is found that there is error in the calculated resonant frequencies of beams based on the lumped mass approximation or Ansys simulation relative to the measured frequencies obtained in the forced or free response experiments. This chapter presents possible error sources that might affect the frequency differences found in Experiment 4, 5, 6, and 10 in Chapter 5.

Furthermore, the size effect, one of the important reasons for the difference between calculated and actual resonant frequencies of A2 tool steel beams is also presented in Section 8-6. Size effect is the dependency of the elastic modulus on the size and kind of material, when the structure is small. This size effect on elastic modulus and damping ratio of A2 tool steel for Micro-Meso scale cantilever beams for the proposed system is investigated.

8-1. Manufacture and Measurement Error

During manufacture, the cross-sectional shape of beams has some error relative to the designed shape. This cross-sectional shape error affects the area moment of inertia of a beam, causing error in the calculated natural frequencies. Moreover, measurement error in measuring the manufactured beams also causes error in the frequency calculations. These error sources are greater in a 3D printing process than wire EDM because 3D printing is an additive material method while wire EDM is a subtractive material method. For instance, the beams of the PLA beam array, as shown in Fig. 30, are designed as a circular cross-section, but the shape of the beams is not circular in

Experiment 4. This shape difference affects the area moment of inertia, which affects the natural frequency of a beam. Moreover, the non-uniform diameter along the beam length causes error in diameter measurement, which also results in error in frequency calculation.

8-2. Boundary Condition Difference between Experiments and Ansys Simulations

In the Ansys simulations for the 1st and 2nd metal prototypes, one of the side surfaces of the beam base is fixed in this Ansys simulation to express the holding by fingers since the experimenter's hand was contacting and exerting pressure on the beam base in previous experiments with plastic prototypes. In Experiments 5 and 6 with the 1st and 2nd metal prototypes, however, the beam arrays are connected to the surface transducer with an ethyl cyanoacrylate adhesive, and they are placed on a table in a horizontal or vertical direction, as shown in Figs. 29 and 33. This difference may affect the frequency shift.

8-3. Powder Type Material of the Metal 3D Printing

The materials of metal 3D printing are in a powder form and have been found to have mechanical properties different from the ordinary metal block. This is one of main reason for the large frequency shift in the prototypes made by metal 3D printing.

During a printing process, the powder material is piled up in layers to build a targeted object, and there are empty spaces between the powders joint due to the size of the powder material (Martin et al. 2017; Weng et al. 2016; Abueidda et al. 2017), as shown in Fig. 66. This causes the difference in mechanical properties of the materials such as the elastic modulus and density between the powder form and the block form,

which have a severe effect on the frequency of a beam. There are many parameter settings that have been researched to increase the efficiency of the metal 3D printing, but the mechanical properties such as elastic modulus and density of the powder material even can be different in every printing process with the same parameter settings. This difference becomes more pronounced when a small object such as microbeams are printed. These results in the large frequency shift in the beams of the beam array made by metal 3D printing, as described in Experiment 6.
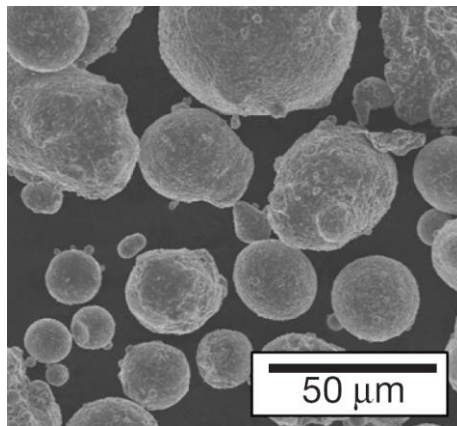
Fig. 66. The image of a standard alloy powder (Martin et al. 2017).

8-4. Calculation of Area Moment of Inertia along Varying Bending Axes

The area moment of inertia can be different even in the same object depending on the axis on which bending occurs, as described in Chapter 3, Section 3-1. If the width of a rectangular cross-sectional beam is smaller than the height, the main vibration occurs in x direction, and the area moment inertia along y direction, I_y, expressed as $\frac{b^3 h}{12}$, must be used rather than the area moment inertia along x direction, I_x, expressed as $\frac{b h^3}{12}$. As shown in Tables 7 and 8, the width is thicker than the height of the 1st and 2nd metal prototype due to the manufacture error, and the main vibration is in y direction with those

prototypes. However, in the calculation of the frequency for the beams of those

prototypes, it was assumed that the main vibration direction is x, and the area moment

inertia along x direction, I_x, expressed as $\frac{bh^3}{12}$, was calculated and used. This causes the

frequency shift.

8-5. Error in Fitting a Free Response of a Beam to an Exponential
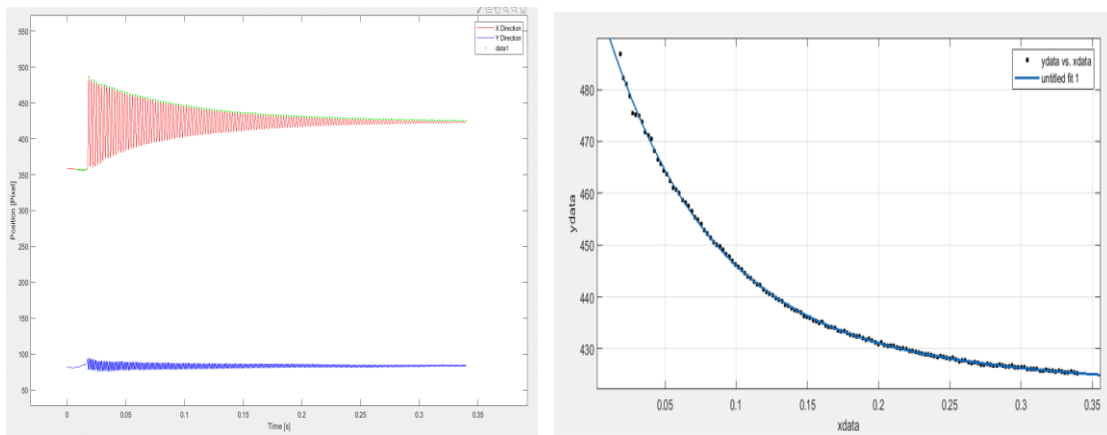
Fig. 67. A beam's free response. (a) The beam position in x (top), y (bottom) direction.
(b) Fitting an exponential decay to x data.

When a free response of a beam is fit to an exponential decay to find the log

decrement, damping ratio, the natural frequency of the beam, Matlab's visual point

tracker and curve fitting function are used. In recording video files of a beam vibration,

the beam is located at around the center of the files to record full beam vibration

movement, as shown in Figs. 24 and 58. Since the visual point tracker in Matlab tracks

the beam movement based on the camera coordinates, the initial position of the tracking

point on the beam tip is not 0 origin, as shown in Figs. 25 and 59. For this reason, the

fitted equation from the free response the beam is consist of two terms of exponential. It

was assumed that the 2nd term of the fitted equation is to describe the initial x position of

the beam, and it can be ignored for the calculation of log decrement. For example, to consider a free response of a beam of the 4th metal prototype, as shown in Eq. (53) and Fig. 67.

$$f(x) = 71.26e^{-13.41x} + 428.6e^{-0.02793x} \tag{53}$$

The 2nd term in Eq. 53 was assumed to describe the initial x position, 428, of the beam and. However, it is found that the 2nd term of the equation is a linear equation with a slope, which cannot be ignored for the calculation of log decrement, as shown Fig. 68.
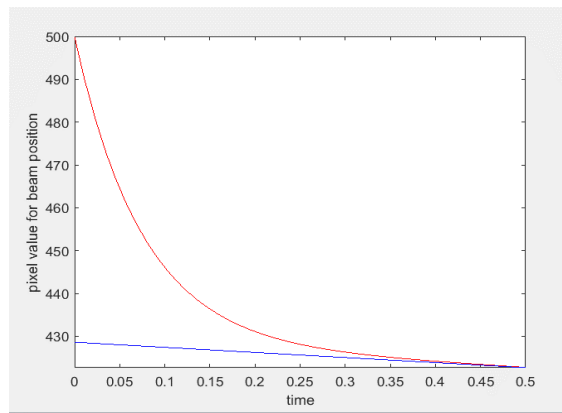
Fig. 68. The image of the fitted equation of a beam. The red one shows the equation with both the 1st and 2nd term. The blue one shows only the 2nd term.

This error in fitting a free response of a beam to an exponential can affect the frequency shift. To fix this error, the initial x position should be subtracted from the data of tracking a beam movement before fitting the data to an exponential decay, which results in only one term of the fitted equation.

8-6. Size Effect of Micro-Mesoscale Steel Beams

The size effect is the dependency of the elastic modulus on the size and kind of material, when the structure is small.

As explained in Chapter 3, the size effect was not considered in my early stage

research due to several reasons: First, the size effect and other non-linear effects of microbeam vibration is intrinsic to certain materials with non-homogenous microstructures by many experimental results. Second, the beams in the proposed system may be much less subject to the size effect and other nonlinearities of microscale elements since the smallest beam size of the model is smaller than the largest size of beams that have shown these nonlinear effects in other researches. Third, there is no known research results about the size effect of materials that are used for my research such as PLA, stainless steel or A2 tool steel.

However, it is found that there is still the frequency difference between the result of Experiment 10 and the calculated frequency based on the lumped mass approximation after adjusting it with all possible methods mentioned above in order to fix the frequency difference. The following subsections represent the size effect for the 10th metal prototype made of A2 tool steel.

8-6-1. Size Effect on Elastic Modulus in Micro-Mesoscale Cantilever Beams

Elastic modulus is a fundamental material property that affects the stiffness and natural frequency of a structure. It is considered as an independent material property in macroscale structures. However, much previous research has shown that the elastic modulus is affected by size in microscale structures. The size effect defines the inconstant elastic modulus depending on the size of a structure. One of the predominant theories for the size effect is the modified couple stress, which introduces additional material length scale parameters in order to analyze the nonlinear behavior of microscale continuous elements(Ghayesh, Farokhi, and Amabili 2014; Farokhi, Ghayesh, and Hussain 2016; Delgado-Velázquez 2007). The length scale parameter results in an additional term in the

elastic modulus, and the resultant elastic modulus is different depending on the kind and size of material. Much previous research has shown that the length scale parameters is revealed as a constant value or a variable value depending on the kind of material or the size of material. According to Abazari et al. (Abazari et al. 2015), the resultant elastic modulus is called the 'effective elastic modulus', E_{eff}, and it can be calculated as in Eq. (54), where v is the Poisson's ratio, l is the length scale parameter, and h is the height of the material when the main vibration is in y direction.

$$E_{eff} = E + 24 \frac{E}{1+v} \left(\frac{l}{h}\right)^2 \qquad (54)$$

Various research studies have shown effective elastic modulus change of some materials such as polymer, plastic, and some metals. Their effective elastic modulus sometimes increases, decreases, or is constant when the dimension of material changes(McFarland and Colton 2005; Liu et al. 2006; Ballestra et al. 2010; Li et al. 2003; Nilsson, Borrisé, and Montelius 2004; Babaei Gavan et al. 2009; Chen et al. 2006).

Currently, the 'size effect' which results in a variation in elastic modulus can only be determined empirically – the effect of size on elastic modulus varies depending upon material and size of material, and there is no known analytical relationship. Here, the size effect on mesoscale cantilever beams of A2 tool steel is investigated.

8-6-2. Resonant Frequencies of the 4th Metal Prototype based on Three Different Methods

The 4th metal prototype shown in Fig. 18 is used to conduct a free-response experiment. The experimental result is then compared to both the calculations from a lumped-mass approximation of the microbeams, as shown in Eq. (13), and the experimental result of a force response experiment in Experiment 10, in Chapter 5,

Section 5-2-2-3.

The resonant frequencies of the prototype are re-calculated considering the right bending direction for the area moment of inertia, as described in Chapter 8, Section 8-4. Since the height of each beam is the same, and the width of each beam is different, only the beam vibration in the direction of the width, here referred to as the x direction, is considered as the main vibration for the experiment to calculate the area moment of inertia. Table 25 shows the actual dimensions of the beam array and resonant frequency re-calculated based on the lumped mass model. Fig. 69 shows the forced response of one of the beams and its fitting curve using Matlab.
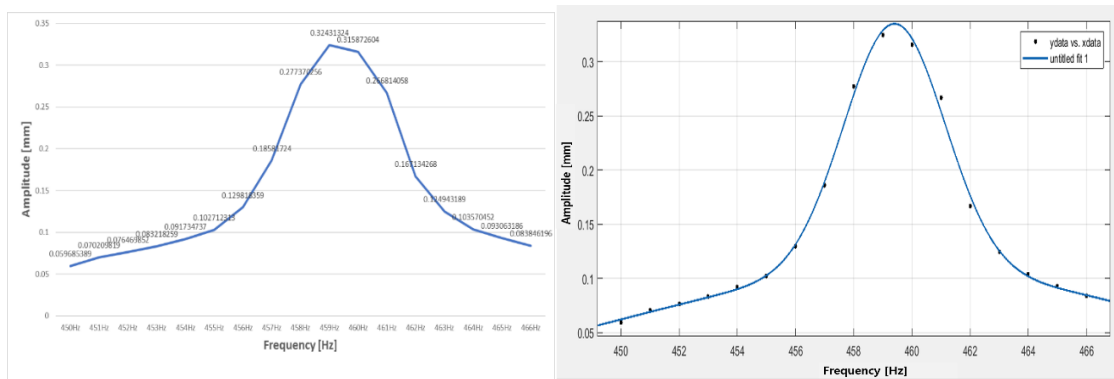
Fig. 69. The 1st beam's forced response and its fitting curve. (a) the experimental data from forced response. (b) the fitted data in Matlab.

Table 25. List of the recalculated resonant frequencies of the 12 beams.

Beam number	Actual Height h [mm]	Actual Width b [mm]	Ratio of h and b	Resonant Frequency from Lumped Mass Method [Hz]
1	1.179	0.524	2.249	501.63
2	1.173	0.581	2.018	556.12
3	1.167	0.635	1.837	607.89
4	1.173	0.694	1.690	663.93
5	1.167	0.738	1.582	705.70
6	1.168	0.797	1.466	762.28

7	1.155	0.845	1.367	808.60
8	1.155	0.911	1.268	871.60
9	1.149	0.953	1.206	911.96
10	1.162	1.012	1.148	968.36
11	1.155	1.070	1.080	1023.52
12	1.155	1.127	1.025	1078.19

For the free response experiment, a high-speed camera setup in Experiment 9 is used. The top of each beam is placed within view of the high-speed camera, and a small metal rod is used to 'flick' the beam, thus exciting the beam's natural frequency. The resulting vibration of the beam is recorded at 21650 frames/s, which is higher than the one in forced response experiment. In the forced response experiment, Matlab's point tracker is used to track the amplitude of beam vibration, and the results are compared to determine which excitation frequency corresponds to the maximum amplitude. However, in the free response experiment, a higher frame rate is used because not only the amplitude but also other vibrational parameters such as damping ratio and log decrement are needed to be calculated. The beam array is fixed by using double sided tape so that it would not move by the force from flicking of the metal rod. Experiments are conducted seven times for each beam. Fig. 70 shows one frame of the high-speed camera free response test.
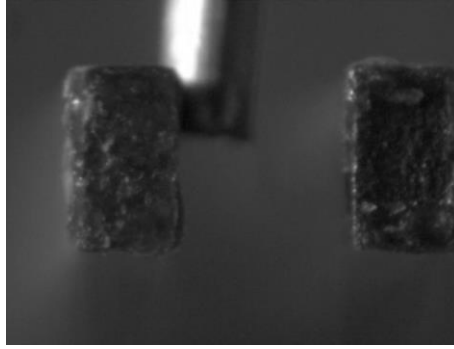
Fig. 70. The moment of hitting a beam with a rod in the free response experiment.

Matlab's visual point tracker is used to track the position of the top of the beam over time in the x (width) and y (height) directions for each recording, and the free response of one of the beams is shown in Fig. 71. Since the height of each beam is constant, and the width of each beam varies, the beam vibration in only x direction is considered as the main vibration for the experiment.
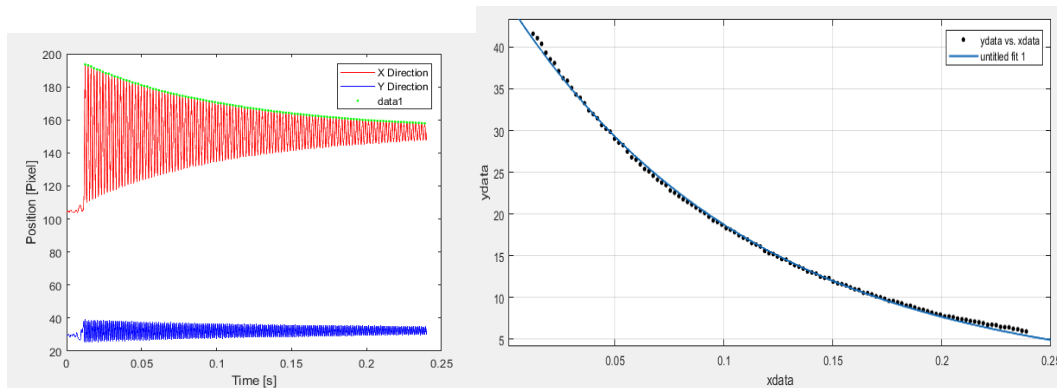
Fig. 71. The 2nd beam's free response. (a) The beam position in x (top), y (bottom) direction. (b) Fitting an exponential decay to x data.

The x vibration shows the response of an under-damped second-order system. Matlab's curve fitting is then used to fit an exponential decay to the peaks of the x data. The fitted equation from the offset data for the 2nd beam is shown in Eq. (55), where t is time value.

$$f(x) = 45.71e^{-8.919t} \tag{55}$$

The peak values are then used to determine the log decrement δ, which can be calculated according to Eq. (50). Table 26 reports some of peak values and the calculated log decrement for several peaks for the 2nd beam.

Table 26. Calculations for log decrement with data fitting.

Peak Number	Actual Peak Value [pixels]	Fitted and Offset Peak Value [pixels]	Log Decrement from Fitted and Offset Peak Value
1	41.587	40.932	0.0175
2	41.069	40.220	0.0175
3	40.388	39.520	0.0175
4	39.321	38.833	0.0175
5	38.539	38.157	0.0175
6	38.085	37.493	0.0175
7	37.105	36.841	0.0175

The captured data can then be used to determine the damping ratio of each beam using the log decrement method as shown in Eq. (51), where δ is log decrement and ζ is the damping ratio. The calculated damping ratio of each beam is shown in the Table 29.

In the free response of a beam, the resonant frequency, ω_r, can be determined using the period of each peak, T, as shown in Eq. (56).

$$\omega_r = \frac{2\pi}{T} \qquad (56)$$

Since the period T is the amount of time between adjacent peaks, it can be calculated as the number of frames f between adjacent peaks divided by the frame rate, as shown in Eq. (57).

$$T = \frac{f\ [frames]}{21650\ [\frac{frames}{second}]} \qquad (57)$$

The resonant frequency of each beam from the free response experiment is

shown in Table 27.

8-6-3. Effective Elastic Modulus and Length Scale Parameter under Micro-Mesoscale

Table 27 and Fig. 72 show the values of resonant frequency determined using the three methods investigated in this study: The calculated resonant frequency based on the lumped mass approximation is denoted by f_lm, the resonant frequency from the forced response experiment is denoted by f_forced, and the resonant frequency from the free response experiment is denoted by f_free.

Table 27. The three types of resonant frequency of each beam and the difference between each type.

Beam Number	Actual Width b [μm]	f_lm [Hz]	f_forced [Hz]	f_free [Hz]	f_lm- f_forced	f_lm- f_free
1	524.351	501.63	459	457	42.63	44.63
2	581.311	556.12	511	508	45.12	48.12
3	635.434	607.89	567	564	40.89	43.89
4	694.006	663.93	612	610	51.93	53.93
5	737.673	705.70	656	657	49.7	48.7
6	796.810	762.28	715	715	47.28	47.28
7	845.230	808.60	761	764	47.6	44.6
8	911.090	871.60	825	821	46.6	50.6
9	953.273	911.96	866	866	45.96	45.96
10	1012.235	968.36	915	911	53.36	57.36
11	1069.886	1023.52	971	966	52.52	57.52
12	1127.032	1078.19	1010	1006	68.19	72.19
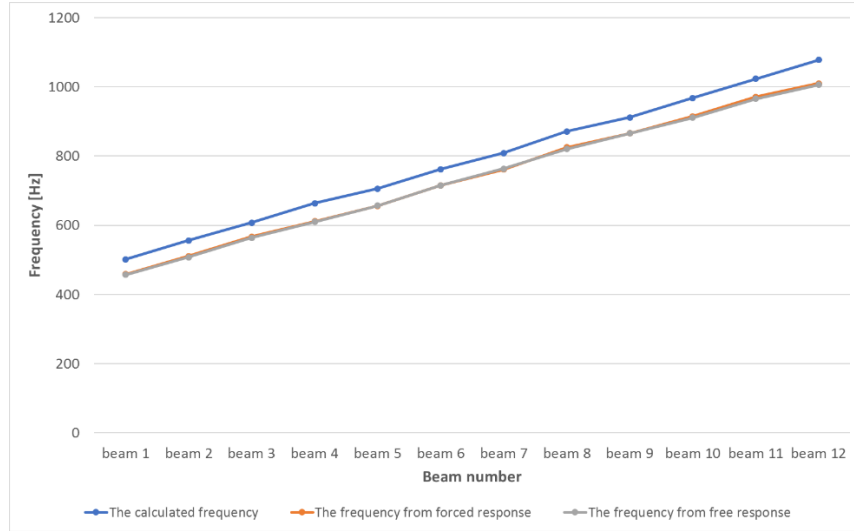
Fig. 72. The three types of resonant frequency of each beam.

It is found that the resonant frequency of each beam obtained from both forced response and free response experiments is very similar. However, the calculated resonant frequency based on the lumped mass approximation and using the well-known elastic modulus of A2 tool steel is quite different from other two calculations. The frequency difference is increased as the width of the beam increases.

From Eq. (13), either a variation in stiffness or in mass is the reason of the frequency difference. Since mass is the product of density, height, width and length of a material, measurement error might affect the frequency difference. However, the standard deviation in the beam dimension measurement is less than 0.01 mm for every beam, which causes a frequency difference of up to 10 Hz. Therefore, dimension measurement error cannot alone explain a frequency difference of at least 40 Hz as seen in Table 27. As a result, a difference in stiffness to explain the frequency difference is considered. If the same value of equivalent mass of each beam is used for the three types resonant frequency calculation, there is a difference of stiffness calculated from the lumped-mass model and the stiffness calculated from either the forced or the free response. This is

consistent with the size effect. Using Eqs. (11) and (13), the three types of stiffness are calculated, as shown in Fig. 73.
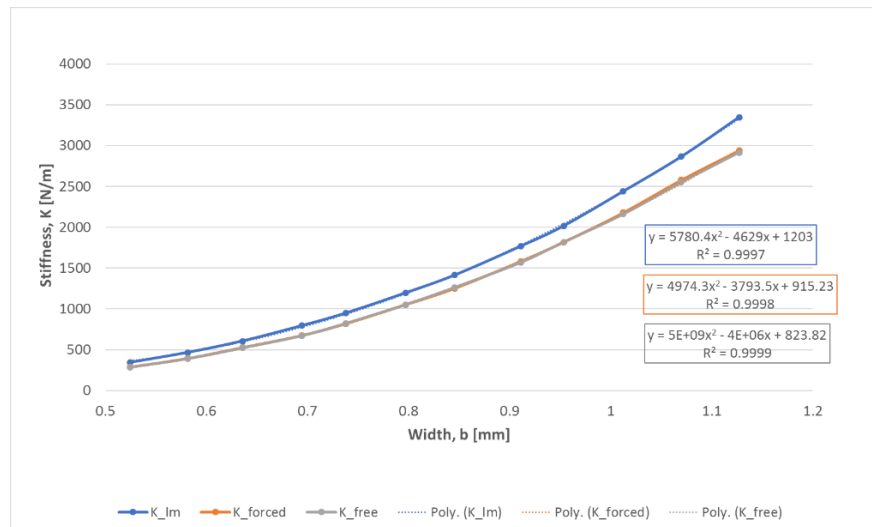
Fig. 73. The three types of stiffness difference.

It is found that the stiffness value and stiffness difference between the one from f_lm and the one from either f_forced or f_free increases as the width of each beam, b, increases. Given that the same value of area moment of inertia and the actual length of each beam are used to calculate the stiffness of three types, the only parameter that could cause this stiffness difference is elastic modulus, as shown Eq. (13). This can show that the elastic modulus of A2 tool steel changes at the mesoscale, and the effective elastic modulus should be required to investigate the resonant behavior of beams in micro and even mesoscale. Fig. 74 Shows the effective elastic modulus calculated from the resonant frequencies obtained from both forced response and free response experiment, which were calculated from Eq. (13).
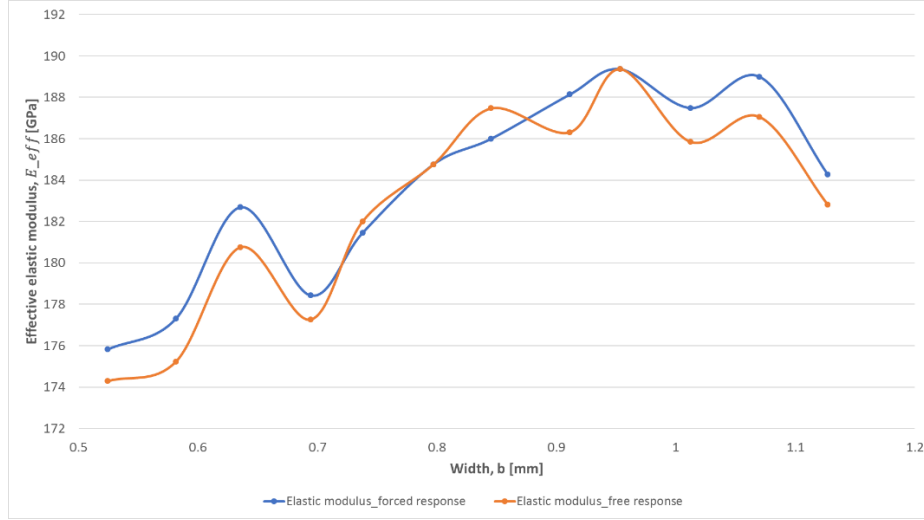
Fig. 74. The effective elastic modulus of forced response and free response.

Since the main vibration direction in the research is in the x (width) direction, height, h in Eq. (54) is changed to width, b for the model, as shown in Eq. (58) (Abazari et al. 2015).

$$E_{eff} = E + 24 \frac{E}{1+v} (\frac{l}{b})^2 \qquad (58)$$

If the well-known Poisson's ratio of A2 tool steel, 0.3, is used for calculation, Eq. (58) can be represented into Eq. (59).

$$l = b \sqrt{\frac{1.3(E - E_{eff})}{(-24) * 210 \times 10^9}} \qquad (59)$$

Then, the length scale parameter of each beam made of A2 tool steel can be calculated, and it is shown in Fig. 75.
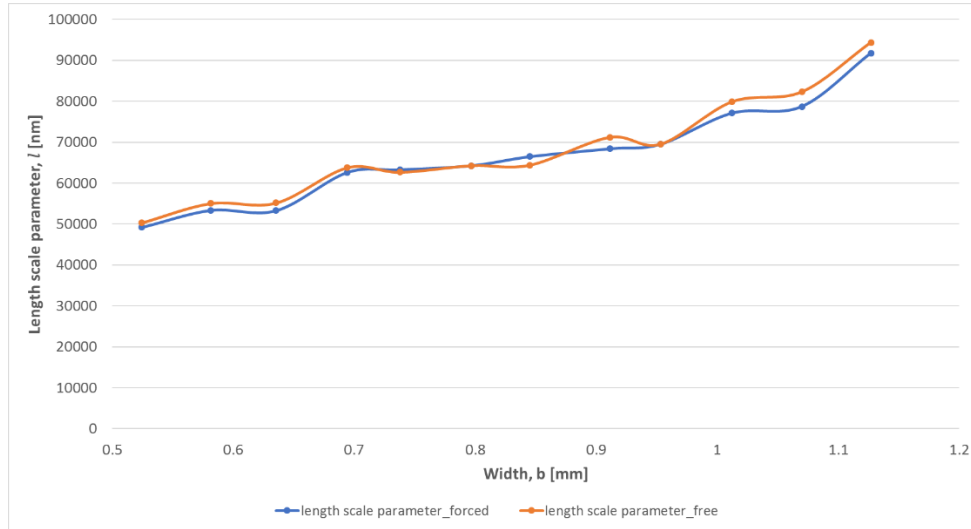
Fig. 75. The relationship between length scale parameter and width.

It is found that the length scale parameter obtained from both forced response and free response experiment increases slightly as the width of beams increases. Table 28 shows the effective elastic modulus, length scale parameter, and length scale parameter divided by width of both forced response and free response experiment, and both results are very similar. The difference of the effective elastic modulus, length scale parameter, and length scale parameter divided by width are within 1.19%, 4.6%, and 4.5% respectively. It is also found that the length scale parameter divided by width has a value between around 0.7 and 0.9, and it generally decreases as the width increases. In my model, the length scale parameter could be considered to decrease as the ratio of height and width decreases. In other words, a thin beam, which has a higher ratio of height and width, has a higher length scale parameter per width rather than a thick beam in micro and mesoscale beams made A2 tool steel.

Table 28. The effective elastic modulus, length scale parameters from the forced and free response of each beam.

Beam Number	Eeff_forced [GPa]	Eeff_free [GPa]	Length scale_forced [nm]	Length scale_free [nm]	Length scale_forced/b	Length scale_forced/b
1	175.827	174.298	49228	50318	0.0939	0.0960
2	177.308	175.233	53380	55049	0.0918	0.0947
3	182.696	180.768	53325	55176	0.0839	0.0868
4	178.435	177.271	62621	63765	0.0902	0.0919
5	181.461	182.015	63290	62673	0.0858	0.0850
6	184.760	184.760	64292	64292	0.0807	0.0807
7	186.005	187.474	66495	64427	0.0787	0.0762
8	188.144	186.324	68407	71199	0.0751	0.0781
9	189.368	189.368	69542	69542	0.0730	0.0730
10	187.493	185.857	77125	79878	0.0762	0.0789
11	189.003	187.061	78735	82295	0.0736	0.0769
12	184.278	182.822	91799	94363	0.0815	0.0837

8-6-4. Damping Ratio under Micro-Mesoscale

In the free response of beam vibration, the damping ratio of each beam is calculated using log decrement in Eq. (51). Free response experiments are conducted seven times for each beam, and the mean damping ratio is obtained from the data. Table 29 shows the mean damping ratio and its standard deviation.

Table 29. List of the mean damping ratio and its standard deviation of the 12 beams made by wire EDM.

Beam Number	Actual Width b [μm]	Mean Damping Ratio	Standard Deviation	Ratio of h and b
1	524.351	0.00201	0.000263	2.249
2	581.311	0.00249	0.000225	2.018
3	635.434	0.00470	0.000378	1.837
4	694.006	0.00709	0.000597	1.690
5	737.673	0.01110	0.001044	1.582
6	796.810	0.01054	0.000313	1.466

7	845.230	0.01058	0.001057	1.367
8	911.090	0.00941	0.000487	1.268
9	953.273	0.01076	0.001129	1.206
10	1012.235	0.01330	0.001027	1.148
11	1069.886	0.01398	0.001811	1.080
12	1127.032	0.01544	0.002414	1.025
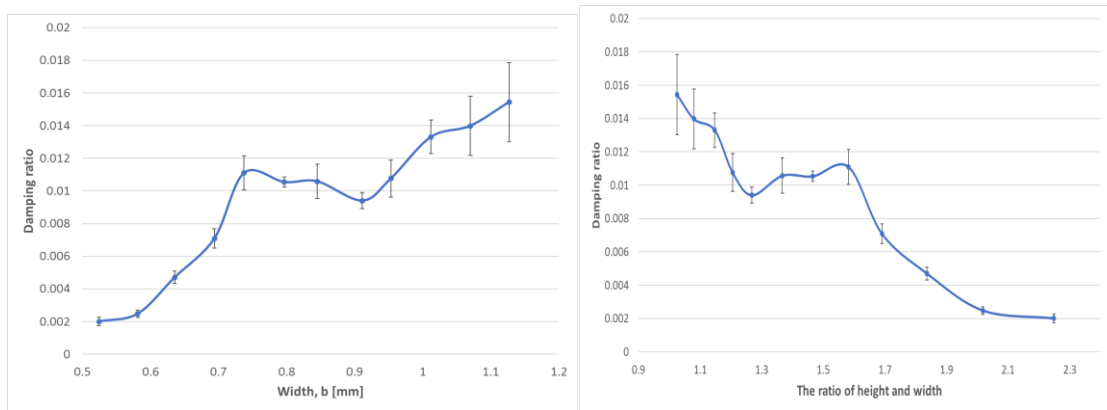
Fig. 76. The damping ratio of each beam. (a) Damping ratio depending on the width of beams. (b) The relationship between damping and the ratio of h and b.

Fig. 76 shows the difference in damping ratio depending on the width of each beam. It is found that the damping ratio increases as the width of the beam increases until the width reaches 0.74 mm. After that, the damping ratio is maintained as 0.01. After the beam width is larger than around 1 mm, the damping ratio increases again. While the standard deviation of damping is comparatively small until the width is smaller than 1 mm, the standard deviation becomes larger after the width is bigger than 1 mm, which is corresponds to from the 10th to 12th beam. For that range of widths, the damping increases as the amplitude of beam vibration becomes larger due to the stronger flicking force applied to the beam. This is because, beam vibration is excited around many different axes when the beam cross-section is close to square. In other words, when the

amplitude of beam vibration in *x* direction becomes smaller than the amplitude in *y* direction, the main vibration direction is changed, which seems to affect the vibration in *x* direction. At that time, the shape of vibration in *x* direction is changed, making it difficult to fit into an exponential decay. Moreover, a beating pattern also appears. These tendencies become stronger as the ratio of height and width becomes closer to 1.

Fig. 76 also shows the difference of damping ratio with width depending on the ratio of height and width of beams. It is found that to minimize the damping ratio variation in a beam array for haptic display, it is better to have beams having smaller ratio of height and width than 2.0.

8-7. Conclusion from Size Effect of Micro-Mesoscale Steel Beams

In this chapter, the reason of the frequency shift (difference) between the frequency obtained in the forced or free response of beams of an array and the frequency calculated based on the lumped mass approximation or simulated by Ansys with measured dimensions of the beams.

In the section 8-1 to 8-5, diverse reasons of the frequency shift are investigated: 1. The manufacture and measurement error. 2. Boundary condition difference between experiments and simulation. 3. Powder type material of the metal 3D printing. 4. Calculation of area moment of inertia along wrong direction. 6. Error in fitting a free response of a beam to an exponential.

In the section 8-6, the size effects, one of dominant reason for the frequency shift, on the mesoscale beams made of A2 tool steel are investigated. By comparison of three types of resonant frequency obtained from a lumped mass approximation, forced

response experiment, and free response experiment, stiffness and elastic modulus difference are studied. Resonant behaviors of cantilever beams with size effect are investigated, and the length scale parameter and damping ratio depending on the actual dimension and the ratio of height and width are calculated based on the modified couple stress theory.

The result might have some minor errors such as manufacture, measurement, and data fitting error. Manufacturing error might occur during the wire EDM machining process, and the dimension of beam might not be perfectly homogeneous along the length of beams. Measurement error might occur during the measurement process for beam dimensions. In the forced and free response analysis, the tracking point for the targeted beam in Matlab might rarely move to adjacent point, which might cause minor error. In the free response analysis, the R^2 value of fitting curve is 0.9916 to 0.999 for the 1st to 9th beam, and 0.9646 to 0.9963 for the 10th to 12th beam. From the 10th to 12th beam, since their ratio of height and width is close to 1, it would be hard to neglect the beam vibration not in x direction, which causes a minor error.

CHAPTER 9: DISCUSSION, CONCLUSIONS AND FUTURE WORK

9-1. Discussion and Conclusion

This work includes six primary research phases: propose vibration model, design beam array for plastic and metal material, propose manufacturing methods for plastic and metal material, evaluate vibration model of plastic and metal material, human tactile experiment, and evaluation of error sources and size effect of micro-meso scale steel beam.

Two vibration models are proposed: the lumped mass vibration model for a single beam and a multi degree of freedom base excitation vibration model for a complete vibration array. Many design parameters are considered to make proper prototypes. For each important parameter, a design algorithm or a simulation tool are proposed. For other important parameters such as the natural frequency and amplitude of a beam, an optimization algorithm is proposed. Diverse plastic and metal materials are considered for beam design, and various manufacture methods are also considered to make several prototypes.

The prototype models are evaluated by the forced or free response experiment using a high speed camera. For those experiments, Ansys simulations of the prototypes are conducted to find the resonant frequency of each beam. To solve the user perception problem that the finger stops the beam vibrating due to the finger force exerting on the beam tips, human experiment with diverse possible solutions are conducted.

In previous experiments with plastic and metal prototypes, it is found that there is error in the calculated resonant frequencies of beams based on the lumped mass approximation or Ansys simulation relative to the measured frequencies obtained in the

forced or free response experiments. Possible error sources that might affect the frequency differences are considered.

The size effect, which is the dependency of the elastic modulus on the size and kind of material, on the micro-mesoscale beams made of A2 tool steel is investigated. Definition of the size effect on A2 tool steel micro-mesoscale beams is an important contribution because it becomes more difficult to predict the resonant frequency of each beam due to the changes in elastic modulus and damping ratio in micro-mesoscale. Moreover, the number of beams that can be manufactured within a certain frequency range, which has a unique resonant frequency, is reduced due to the larger bandwidth and crosstalk between each beam.

The following is a summary of the contributions and conclusions of this work:

(1) Proposed two vibration models: the lumped mass vibration model for a single beam and a multi degree of freedom base excitation vibration model for a complete vibration array.

- The correction coefficient 0.985555741 is multiplied by the resonant frequency calculated by the lumped-mass model, then the resonant frequency from the eigenvalue method can be calculated.

(2) Created beam dimension optimization algorithm that considers important parameters such as beam dimension, damping ratio, manufacturing resolution and others, which can affect the frequency and amplitude of beams.

- The lowest frequency can guarantee the highest amplitude since they are inversely proportional. Moreover, in the condition of limited X/Y resolution of any manufacture method for micro-mesoscale beams and the limit of

beam length difference for the surface defined by the beam tips, which needs

no inflection points, the lowest frequency should be selected for the

algorithm.

(3) Investigated three different manufacture methods for micro-meso cantilever

beams: FDM 3D printing, Metal sintering 3D printing, Wire EDM.

- The number of beams that can be made with each method in the frequency

  range from 20 to 20 kHz, which is the audible frequency range, is revealed.

(4) Proposed manufacturing methods with plastic material for micro-mesoscale

beams by investigating diverse 3D printers and materials.

- Lulzbot 3D printer with PLA works the best to manufacture a plastic

  material beam array among the 3D printers that have been investigated such

  as Objet 3D printer, Fortus 3D printer or form 1+ 3D printer.

(5) Evaluated plastic material prototypes by the forced or free response experiment.

- PLA plastic material's damping ratio is 0.01.

- There is a crosstalk problem, which the bandwidth of different beams

  overlaps due to high damping ratio.

- Error is found in the calculated resonant frequencies of beams based on the

  lumped mass approximation or Ansys simulation relative to the measured

  frequencies obtained in the forced or free response experiments.

(6) Proposed manufacturing methods with metal material for micro-mesoscale

beams by manufacturing same models with Metal sintering and wire EMD.

- Wire EDM has a higher X/Y resolution than metal sintering so that the

  number of beams having unique frequencies, which can be manufactured by

wire EDM, in a certain frequency range is theoretically higher than the one made by metal sintering. For example, the number of beams made of A2 tool steel, made by wire EDM is 12961, and the number of stainless steel, made by metal sintering is 8982.

- For manufacture of many beams having a unique frequency, it is not worth to use wire EDM due to the limit in manufacture, which the dimension of the beams in the same direction must be same for all beam in a row or column.

- There is another important parameter to manufacture a beam array, which is the surface defined by beam tips. The placement of the beam should be considered for human contact and user perception.

(7) Presented Ansys simulation model using a finite element method for three metal prototypes, which the results of the simulations are used to conduct experiments to evaluate each model.

- The simulation results are different than the experimental results due to diverse error sources described in Chapter 8. The size effect is the main reason for the difference, and the power type material is also the reason affects the difference significantly in the prototypes made by metal sintering 3D printing.

(8) Evaluated metal material prototypes by the forced or free response experiment using C-clamp to avoid the force exerted by finger holding and to maximize the amplitude of beam vibration.

- The force of the clamp cannot be measured by FSR (force-sensitive resistor) type of sensor, and 'Normal holding' is the best to maximize beam vibration

amplitude according to a quantitative method.

- Error is found in the calculated resonant frequencies of beams based on the lumped mass approximation or Ansys simulation relative to the measured frequencies obtained in the forced or free response experiments.

(9) Presented finger touch experiment with various attempts such as a dry finger contact, wet and soaped finger contact, U or L-shaped constraints in order to reduce the coefficient or the normal force exerted by the finger of the friction.

- No beam vibration is felt regardless using water and soap to reduce the coefficient of the friction

- Beam vibration is easily perceived by tapping but rarely perceived by touching when using the constraints.

- The proper length of the constraint is between the beam length and 0.2 mm more than the beam length.

- Even with the proper length of the constraint, beam vibration is perceived by touching the beam tips very weakly.

- It is found that the people skin can recognize a vibrating object more easily by applying some amount of pressure, which always stops beam vibration.

- No beam vibration is perceived after the 4th beam of the 4th metal prototype, which the resonant frequency is around 500 Hz due to small amplitude.

- The maximum finger force, which does not stop beam vibration, is found by a weight, and it is less than or equal to 1 gram, which is equal to 0.01 N.

(10) Presented finger touch experiment with silicone rubber beams attached metal beam tips in order to solve the user perception problem.

- Beam vibration can be much easily perceived by attaching silicone rubber beams to the metal beam tips.

- There are certain lengths of the silicone rubber beams for which the 2nd metal beam vibrates with much lower amplitude.

- Between the two certain lengths, the amplitude of beam vibration becomes larger and then becomes smaller after a certain silicone rubber beam length.

- The resonant frequency of the 2nd metal beam trends towards the resonant frequency of the beam without the silicone rubber beam, as the silicone rubber beam length becomes shorter.

- When the amplitude of vibration of the metal beam is very small due to the certain length of the silicone rubber beam, the resonant frequency becomes very different than it was without the rubber beam.

- When the silicone rubber beam length is longer than 10mm, the maximum amplitude and resonant frequency of the steel beam cannot be determined.

- When the silicone rubber beam length is shorter than 2mm, the vibration of the beam becomes more difficult to perceive by touch.

- Silicone rubber beams may absorb the beam vibration from other metal beams.

- The optimal rubber length, which maximizes the vibrational amplitude of the 2nd metal beam, is found to be 4.3, 4.6, 3.4mm in three experiment sets.

- If the length of the 2nd rubber beam is different than the lengths of the other rubber beams, then the frequency response of the 2nd metal beam is very different than it is when every rubber beam has the same length.

- If the difference in length between the 2nd rubber beam and other rubber beams is small, and the length of the 2nd rubber beam is around the length with the maximum amplitude, the vibration result is similar with the case of all silicone rubber beams with the same length.

(11) Evaluated silicone rubber beams that are around 1.1mm in width and height and 10.3mm in length, which is made of the dragon skin 10 very fast.

- The silicone rubber beams' damping ratio is 0.0836.

(12) Evaluated error sources for the difference in between the frequencies based on the lumped mass approximation or Ansys simulation and the measured frequencies obtained in the forced or free response experiments.

- Manufacture and measurement error are a reason for the difference, and they are greater in a 3D printing process than wire EDM process

- Boundary condition difference between experiments and Ansys simulations is a reason for the difference.

- Powder type material of the metal 3D printing is one of important reasons for the sintered prototypes.

- Calculation of area moment of inertia along varying bending axes is a reason for the difference.

- Error in fitting a free response of a beam to an exponential is also a reason for error.

(13) Presented size effect on micro-meso scale steel beams, which is most important reason for error in frequencies, based on the fact that the resonant frequency difference found between the three different methods: The calculated resonant

frequency based on the lumped mass approximation, the resonant frequency from the forced response experiment, and the resonant frequency from the free response experiment.

- The calculated resonant frequency based on the lumped mass approximation and using the well-known elastic modulus of A2 tool steel is quite different from other two calculations.

- A variation in stiffness or in mass is the reason of the frequency difference, and the mass variation due to measurement error cannot alone explain a frequency difference of at least 40 Hz.

- A stiffness variation is consistent with the size effect, and only parameter that could cause this stiffness difference is elastic modulus.

- The effective elastic modulus, which defines the variable elastic modulus, should be required to investigate the resonant behavior of beams in micro-mesoscale.

- The length scale parameter, which is an additional term in the effective elastic modulus to explain the elastic modulus difference, increases slightly as the width of beams increases.

- The damping ratio of each beam made of A2 tool steel is different depending on the width of each beam.

- It is found that to minimize the damping ratio variation in a beam array for haptic display, it is better to have beams having smaller ratio of height and width than 2.0.

Contributions (2), (3), (6), and (7) have been published in the first journal paper

(Daehan Wi and Sodemann 2018). Contributions (1), (4), (5) have been published in the first conference paper (D. Wi, Sodemann, and Chicci 2017). Contributions (8), (13) have been submitted to the Journal of Vibration and Control. Contributions (9), (10), (11) have been submitted to a special issue on Haptics for Human Augmentation in Multimodal Technologies and Interaction.

9-2. Future Work

The further research for the investigation of the 5th metal prototype made by metal sintering 3D printing, as shown in Fig. 19, will be required. Since some thin beams failed to be manufactured or are bended, the dimension of each beam, the minimum dimension of beams that are manufactured successfully, and the pattern of the bending is needed to be revealed to make a better prototype that has more accurate dimensions by metal sintering method.

The experiments to obtain the density of the metal prototypes and silicone rubber beams will be required. Since The mechanical properties such as density of a sintered beam made of CO-538-1 powder material and a silicone rubber beam made of the dragon skin 10 very fast are unknown, the well-known density value of stainless steel and silicone rubber are used. The experiment will help to reveal the relationship between metal beams and silicone rubber beams by obtaining the precise density of the materials.

The perceivable frequency range with dynamic touch in the certain forcing amplitude is unknown, the further research will be required. It would be very useful to manufacture a new beam array with better user perception.

If a more accurate metal prototype is manufactured, which has at least 20x20

beams, the human experiment to test the system functionality will be required. Since the

current highest-resolution haptic display on the market (BrainPort) has around 400

resolutions, the experiment result with the new prototype can be compared to BrainPort

and analyzed for the further improvement and prototypes.

REFERENCES

Abazari, Amir Musa, Seyed Mohsen Safavi, Ghader Rezazadeh, and Luis Guillermo Villanueva. 2015. "Modelling the Size Effects on the Mechanical Properties of Micro/Nano Structures." *Sensors* 15 (11): 28543–62. https://doi.org/10.3390/s151128543.

Abueidda, Diab W., Mete Bakir, Rashid K. Abu Al-Rub, Jörgen S. Bergström, Nahil A. Sobh, and Iwona Jasiuk. 2017. "Mechanical Properties of 3D Printed Polymeric Cellular Materials with Triply Periodic Minimal Surface Architectures." *Materials & Design* 122 (May): 255–67. https://doi.org/10.1016/j.matdes.2017.03.018.

Akgöz, Bekir, and Ömer Civalek. 2013. "A Size-Dependent Shear Deformation Beam Model Based on the Strain Gradient Elasticity Theory." *International Journal of Engineering Science* 70 (September): 1–14. https://doi.org/10.1016/j.ijengsci.2013.04.004.

Auvray, Malika, Sylvain Hanneton, and J Kevin O'Regan. 2007. "Learning to Perceive with a Visuo — Auditory Substitution System: Localisation and Object Recognition with 'The Voice.'" *Perception* 36 (3): 416–30. https://doi.org/10.1068/p5631.

Babaei Gavan, Khashayar, Hidde J. R. Westra, Emile W. J. M. van der Drift, Warner J. Venstra, and Herre S. J. van der Zant. 2009. "Size-Dependent Effective Young's Modulus of Silicon Nitride Cantilevers." *Applied Physics Letters* 94 (23): 233108. https://doi.org/10.1063/1.3152772.

Bach-y-Rita, P. 1970. "Neurophysiological Basis of a Tactile Vision-Substitution System." *IEEE Transactions on Man-Machine Systems* 11 (1): 108–10. https://doi.org/10.1109/TMMS.1970.299970.

Bach-y-rita, Paul. 1983. "Tactile Vision Substitution: Past and Future." *International Journal of Neuroscience* 19 (1–4): 29–36. https://doi.org/10.3109/00207458309148643.

Bach-Y-Rita, Paul, Carter C. Collins, Frank A. Saunders, Benjamin White, and Lawrence Scadden. 1969. "Vision Substitution by Tactile Image Projection." *Nature* 221 (5184): 963–64. https://doi.org/10.1038/221963a0.

Bach-y-Rita, Paul, and Stephen W. Kercel. 2003. "Sensory Substitution and the Human–Machine Interface." *Trends in Cognitive Sciences* 7 (12): 541–46. https://doi.org/10.1016/j.tics.2003.10.013.

Ballestra, Alberto, Eugenio Brusa, Giorgio De Pasquale, Mircea Gh. Munteanu, and

Aurelio Somà. 2010. "FEM Modelling and Experimental Characterization of Microbeams in Presence of Residual Stress." *Analog Integrated Circuits and Signal Processing* 63 (3): 477–88. https://doi.org/10.1007/s10470-009-9420-9.

Barari, Amin, Hamed Dadashpour Kaliji, Mojtaba Ghadimi, and Davood domiri ganji. 2011. "Non-Linear Vibration of Euler-Bernoulli Beams." *Latin American Journal of Solids and Structures* 8 (June): 139–48. https://doi.org/10.1590/S1679-78252011000200002.

Bhowmick, Alexy, and Shyamanta M. Hazarika. 2017. "An Insight into Assistive Technology for the Visually Impaired and Blind People: State-of-the-Art and Future Trends." *Journal on Multimodal User Interfaces*, January, 1–24. https://doi.org/10.1007/s12193-016-0235-6.

"Bionic Vision for the Blind - Retinal Implant? Eye Surgery?" n.d. Accessed February 21, 2017. https://www.seeingwithsound.com/retinal.htm.

"BLITAB® – Feelings Get Visible." n.d. Accessed February 23, 2017. http://blitab.com/.

Bolanowski Jr, Stanley J., George A. Gescheider, Ronald T. Verrillo, and Christin M. Checkosky. 1988. "Four Channels Mediate the Mechanical Aspects of Touch." *The Journal of the Acoustical Society of America* 84 (5): 1680–1694.

Borst, Christoph W., and Charles D. Cavanaugh. 2004. "Haptic Controller Design and Palm-Sized Vibrotactile Array." *Technical Report*. https://www.researchgate.net/profile/Charles_Cavanaugh/publication/228938509_Haptic _Controller_Design_and_Palm-sized_Vibrotactile_Array/links/02e7e53b5bd0657152000000.pdf.

Bourbakis, N.G., and D. Kavraki. 2001. "An Intelligent Assistant for Navigation of Visually Impaired People." In *Proceedings of the IEEE 2nd International Symposium on Bioinformatics and Bioengineering Conference, 2001*, 230–35. https://doi.org/10.1109/BIBE.2001.974434.

Brown, David, Tom Macpherson, and Jamie Ward. 2011. "Seeing with Sound? Exploring Different Characteristics of a Visual-to-Auditory Sensory Substitution Device." *Perception* 40 (9): 1120–35. https://doi.org/10.1068/p6952.

Campbell, A., and T. Choudhury. 2012. "From Smart to Cognitive Phones." *IEEE Pervasive Computing* 11 (3): 7–11. https://doi.org/10.1109/MPRV.2012.41.

Chen, C. Q., Y. Shi, Y. S. Zhang, J. Zhu, and Y. J. Yan. 2006. "Size Dependence of Young's Modulus in ZnO Nanowires." *Physical Review Letters* 96 (7): 075505. https://doi.org/10.1103/PhysRevLett.96.075505.

Dakopoulos, D., S.K. Boddhu, and N. Bourbakis. 2007. "A 2D Vibration Array as an Assistive Device for Visually Impaired." In *Proceedings of the 7th IEEE International Conference on Bioinformatics and Bioengineering, 2007. BIBE 2007*, 930–37. https://doi.org/10.1109/BIBE.2007.4375670.

Dakopoulos, D., and N. Bourbakis. 2009. "Towards a 2D Tactile Vocabulary for Navigation of Blind and Visually Impaired." In *IEEE International Conference on Systems, Man and Cybernetics, 2009. SMC 2009*, 45–51. https://doi.org/10.1109/ICSMC.2009.5346336.

Dakopoulos, D., and N. G. Bourbakis. 2010. "Wearable Obstacle Avoidance Electronic Travel Aids for Blind: A Survey." *IEEE Transactions on Systems, Man, and Cybernetics, Part C (Applications and Reviews)* 40 (1): 25–35. https://doi.org/10.1109/TSMCC.2009.2021255.

D'Angio, Paul Christopher. 2012. "Adaptive and Passive Non-Visual Driver Assistance Technologies for the Blind Driver Challenge®," April. https://vtechworks.lib.vt.edu/handle/10919/27582.

Danilov, Yuri, and Mitchell Tyler. 2005. "Brainport: An Alternative Input to the Brain." *Journal of Integrative Neuroscience* 4 (04): 537–550.

Delgado-Velázquez, Iván. 2007. "Nonlinear Vibration of a Cantilever Beam." ROCHESTER INSTITUTE OF TECHNOLOGY.

"Dot Incorporation." n.d. Dot Incorporation. Accessed February 23, 2017. http://www.dotincorp.com/.

Du Buf, JM Hans, João Barroso, Jojo MF Rodrigues, Hugo Paredes, Miguel Farrajota, Hugo Fernandes, João José, Victor Teixeira, and Mário Saleiro. 2011. "The SmartVision Navigation Prototype for Blind Users." http://sapientia.ualg.pt/handle/10400.1/893.

"Effective Mass - Serendipedia." n.d. Accessed July 18, 2017. http://www.serendi-cdi.org/serendipedia/index.php?title=Effective_Mass.

Ezaki, N., K. Kiyota, B. T. Minh, M. Bulacu, and L. Schomaker. 2005. "Improved Text-

Detection Methods for a Camera-Based Text Reading System for Blind Persons." In *Eighth International Conference on Document Analysis and Recognition (ICDAR'05)*, 257-261 Vol. 1. https://doi.org/10.1109/ICDAR.2005.137.

"Factsheet on Persons with Disabilities | United Nations Enable." n.d. Accessed March 21, 2019. https://www.un.org/development/desa/disabilities/resources/factsheet-on-persons-with-disabilities.html.

Farokhi, Hamed, and Mergen H. Ghayesh. 2015. "Nonlinear Dynamical Behaviour of Geometrically Imperfect Microplates Based on Modified Couple Stress Theory." *International Journal of Mechanical Sciences* 90 (January): 133–44. https://doi.org/10.1016/j.ijmecsci.2014.11.002.

Farokhi, Hamed, Mergen H. Ghayesh, and Shahid Hussain. 2016. "Large-Amplitude Dynamical Behaviour of Microcantilevers." *International Journal of Engineering Science* 106 (September): 29–41. https://doi.org/10.1016/j.ijengsci.2016.03.002.

Feng, Peng, Xinmiao Meng, Jian-Fei Chen, and Lieping Ye. 2015. "Mechanical Properties of Structures 3D Printed with Cementitious Powders." *Construction and Building Materials* 93 (September): 486–97. https://doi.org/10.1016/j.conbuildmat.2015.05.132.

Ghayesh, Mergen H., and Hamed Farokhi. 2015. "Chaotic Motion of a Parametrically Excited Microbeam." *International Journal of Engineering Science* 96 (November): 34–45. https://doi.org/10.1016/j.ijengsci.2015.07.004.

Ghayesh, Mergen H., Hamed Farokhi, and Marco Amabili. 2014. "In-Plane and out-of-Plane Motion Characteristics of Microbeams with Modal Interactions." *Composites Part B: Engineering* 60 (April): 423–39. https://doi.org/10.1016/j.compositesb.2013.12.074.

GIORDANO, Russell A., Benjamin M. Wu, Scott W. Borland, Linda G. Cima, Emanuel M. Sachs, and Michael J. Cima. 1997. "Mechanical Properties of Dense Polylactic Acid Structures Fabricated by Three Dimensional Printing." *Journal of Biomaterials Science, Polymer Edition* 8 (1): 63–75. https://doi.org/10.1163/156856297X00588.

Grant, Patricia, Lindsey Spencer, Aimee Arnoldussen, Rich Hogle, Amy Nau, Janet Szlyk, Jonathan Nussdorf, Donald C. Fletcher, Keith Gordon, and William Seiple. 2016. "The Functional Performance of the BrainPort V100 Device in Persons Who Are Profoundly Blind." *Journal of Visual Impairment & Blindness* 110 (2): 77–88.

Hee Lee, Gim, Friedrich Faundorfer, and Marc Pollefeys. 2013. "Motion Estimation for

Self-Driving Cars with a Generalized Camera." In *Proceedings of the IEEE Conference on Computer Vision and Pattern Recognition*, 2746–2753. http://www.cv-foundation.org/openaccess/content_cvpr_2013/html/Lee_Motion_Estimation_for_2013_CVPR_paper.html.

Kilgour, Andrea R, Beatrice de Gelder, and Susan J Lederman. 2004. "Haptic Face Recognition and Prosopagnosia." *Neuropsychologia* 42 (6): 707–12. https://doi.org/10.1016/j.neuropsychologia.2003.11.021.

Kim, Junsung, Hyoseung Kim, Karthik Lakshmanan, and Ragunathan Raj Rajkumar. 2013. "Parallel Scheduling for Cyber-Physical Systems: Analysis and Case Study on a Self-Driving Car." In *Proceedings of the ACM/IEEE 4th International Conference on Cyber-Physical Systems*, 31–40. ACM. http://dl.acm.org/citation.cfm?id=2502530.

Kocatürk, Turgut. 2005. "Determination of the Steady-State Response of Viscoelastically Supported Cantilever Beam under Sinusoidal Base Excitation." *Journal of Sound and Vibration* 281 (3): 1145–56. https://doi.org/10.1016/j.jsv.2004.03.028.

Kong, Shengli, Shenjie Zhou, Zhifeng Nie, and Kai Wang. 2009. "Static and Dynamic Analysis of Micro Beams Based on Strain Gradient Elasticity Theory." *International Journal of Engineering Science* 47 (4): 487–98. https://doi.org/10.1016/j.ijengsci.2008.08.008.

Konyo, Masashi, S Tadokoro, and Toshi Takamori. 2000. "Artificial Tactile Feel Display Using Soft Gel Actuators." In *Proceedings - IEEE International Conference on Robotics and Automation*, 4:3416–21 vol.4. https://doi.org/10.1109/ROBOT.2000.845250.

Konyo, Masashi, Satoshi Tadokoro, Akinori Yoshida, and Naoki Saiwaki. 2005. "A Tactile Synthesis Method Using Multiple Frequency Vibrations for Representing Virtual Touch." In *Intelligent Robots and Systems, 2005.(IROS 2005). 2005 IEEE/RSJ International Conference On*, 3965–3971. IEEE.

Lam, D. C. C., F. Yang, A. C. M. Chong, J. Wang, and P. Tong. 2003. "Experiments and Theory in Strain Gradient Elasticity." *Journal of the Mechanics and Physics of Solids* 51 (8): 1477–1508. https://doi.org/10.1016/S0022-5096(03)00053-X.

Lee, Gim Hee, Friedrich Fraundorfer, and Marc Pollefeys. 2013. "Structureless Pose-Graph Loop-Closure with a Multi-Camera System on a Self-Driving Car." In *Intelligent Robots and Systems (IROS), 2013 IEEE/RSJ International Conference On*, 564–571. IEEE. http://ieeexplore.ieee.org/abstract/document/6696407/.

Li, Xinxin, Takahito Ono, Yuelin Wang, and Masayoshi Esashi. 2003. "Ultrathin Single-Crystalline-Silicon Cantilever Resonators: Fabrication Technology and Significant Specimen Size Effect on Young's Modulus." *Applied Physics Letters* 83 (15): 3081–83. https://doi.org/10.1063/1.1618369.

Lisetti, Christine L., and Diane J. Schiano. 2000. "Automatic Facial Expression Interpretation: Where Human-Computer Interaction, Artificial Intelligence and Cognitive Science Intersect." *Pragmatics & Cognition* 8 (1): 185–235.

Liu, K. H., W. L. Wang, Z. Xu, L. Liao, X. D. Bai, and E. G. Wang. 2006. "In Situ Probing Mechanical Properties of Individual Tungsten Oxide Nanowires Directly Grown on Tungsten Tips inside Transmission Electron Microscope." *Applied Physics Letters* 89 (22): 221908. https://doi.org/10.1063/1.2397547.

Loomis, Jack M., Reginald G. Golledge, and Roberta L. Klatzky. 1998. "Navigation System for the Blind: Auditory Display Modes and Guidance." *Presence: Teleoperators and Virtual Environments* 7 (2): 193–203. https://doi.org/10.1162/105474698565677.

Luo, Yvonne H.-L., and Lyndon da Cruz. 2014. "A Review and Update on the Current Status of Retinal Prostheses (Bionic Eye)." *British Medical Bulletin* 109 (1): 31–44. https://doi.org/10.1093/bmb/ldu002.

Mann, Steve, Jason Huang, Ryan Janzen, Raymond Lo, Valmiki Rampersad, Alexander Chen, and Taqveer Doha. 2011. "Blind Navigation with a Wearable Range Camera and Vibrotactile Helmet." In *Proceedings of the 19th ACM International Conference on Multimedia*, 1325–1328. ACM. http://dl.acm.org/citation.cfm?id=2072005.

Martin, John H., Brennan D. Yahata, Jacob M. Hundley, Justin A. Mayer, Tobias A. Schaedler, and Tresa M. Pollock. 2017. "3D Printing of High-Strength Aluminium Alloys." *Nature* 549 (7672): 365–69. https://doi.org/10.1038/nature23894.

McDaniel, Troy, Shantanu Bala, Jacob Rosenthal, Ramin Tadayon, Arash Tadayon, and Sethuraman Panchanathan. 2014. "Affective Haptics for Enhancing Access to Social Interactions for Individuals Who Are Blind." In *Universal Access in Human-Computer Interaction. Design and Development Methods for Universal Access*, 419–29. Springer, Cham. https://doi.org/10.1007/978-3-319-07437-5_40.

McFarland, Andrew W., and Jonathan S. Colton. 2005. "Role of Material Microstructure in Plate Stiffness with Relevance to Microcantilever Sensors." *Journal of Micromechanics and Microengineering* 15 (5): 1060–1067. https://doi.org/10.1088/0960-1317/15/5/024.

Nari Kim, Myoung-Ae Choi, Gyoungwan Lee, Minsun Kim, and Byungrim Park. 2013. "Assessment of tactile acuity by vibrotactile stimulation in blind and deaf humans." 시각장애연구 29 (3): 49–62.

Nau, Amy, Michael Bach, and Christopher Fisher. 2013. "Clinical Tests of Ultra-Low Vision Used to Evaluate Rudimentary Visual Perceptions Enabled by the BrainPort Vision Device." *Translational Vision Science & Technology* 2 (3): 1–1.

Ng, Choon-Boon, Yong-Haur Tay, and Bok-Min Goi. 2015. "A Review of Facial Gender Recognition." *Pattern Analysis and Applications* 18 (4): 739–55. https://doi.org/10.1007/s10044-015-0499-6.

Nilsson, S. G., X. Borrisé, and L. Montelius. 2004. "Size Effect on Young's Modulus of Thin Chromium Cantilevers." *Applied Physics Letters* 85 (16): 3555–57. https://doi.org/10.1063/1.1807945.

O'Meara, D. M., and R. M. Smith. 2001. "Static Friction Properties between Human Palmar Skin and Five Grabrail Materials." *Ergonomics* 44 (11): 973–88. https://doi.org/10.1080/00140130110074882.

Ong, Jong Min, and Lyndon da Cruz. 2012. "The Bionic Eye: A Review." *Clinical & Experimental Ophthalmology* 40 (1): 6–17. https://doi.org/10.1111/j.1442-9071.2011.02590.x.

Park, Taekeun, Jungil Jung, and Jinsoo Cho. 2016. "A Method for Automatically Translating Print Books into Electronic Braille Books." *Science China Information Sciences* 59 (7): 072101. https://doi.org/10.1007/s11432-016-5575-z.

Ramstein, Christophe. 1996. "Combining Haptic and Braille Technologies: Design Issues and Pilot Study." In *Proceedings of the Second Annual ACM Conference on Assistive Technologies*, 37–44. Assets '96. New York, NY, USA: ACM. https://doi.org/10.1145/228347.228355.

Réhman, Shafiq ur. 2010. *Expressing Emotions through Vibration for Perception and Control*. Department of Applied Physics and Electronics, Ume\a a University. https://pdfs.semanticscholar.org/fd4c/46bfd3bb00ed93b0bb5b28ef0336f59f0c15.pdf.

Romero, Mario, Brian Frey, Caleb Southern, and Gregory D. Abowd. 2011.

"BrailleTouch: Designing a Mobile Eyes-Free Soft Keyboard." In *Proceedings of the 13th International Conference on Human Computer Interaction with Mobile Devices and Services*, 707–709. MobileHCI '11. New York, NY, USA: ACM. https://doi.org/10.1145/2037373.2037491.

Ruspini, Diego C., Krasimir Kolarov, and Oussama Khatib. 1997. "The Haptic Display of Complex Graphical Environments." In *Proceedings of the 24th Annual Conference on Computer Graphics and Interactive Techniques*, 345–352. ACM Press/Addison-Wesley Publishing Co. http://dl.acm.org/citation.cfm?id=258878.

"Structural Dynamics - Beams." n.d. Accessed March 16, 2017. http://www.vibrationdata.com/beams.htm.

Sun, Wei, Ying Liu, Hui Li, and Dejun Pan. 2013. "Determination of the Response Distributions of Cantilever Beam under Sinusoidal Base Excitation." In *Journal of Physics: Conference Series*, 448:012010. IOP Publishing. http://iopscience.iop.org/article/10.1088/1742-6596/448/1/012010/meta.

Tan, X. P., Y. J. Tan, C. S. L. Chow, S. B. Tor, and W. Y. Yeong. 2017. "Metallic Powder-Bed Based 3D Printing of Cellular Scaffolds for Orthopaedic Implants: A State-of-the-Art Review on Manufacturing, Topological Design, Mechanical Properties and Biocompatibility." *Materials Science and Engineering: C* 76 (July): 1328–43. https://doi.org/10.1016/j.msec.2017.02.094.

"Vision Impairment and Blindness." n.d. Accessed March 21, 2019. https://www.who.int/news-room/fact-sheets/detail/blindness-and-visual-impairment.

Wacker, Philipp, Chat Wacharamanotham, Daniel Spelmezan, Jan Thar, David A. Sánchez, René Bohne, and Jan Borchers. 2016. "VibroVision: An On-Body Tactile Image Guide for the Blind." In *Proceedings of the 2016 CHI Conference Extended Abstracts on Human Factors in Computing Systems*, 3788–3791. CHI EA '16. New York, NY, USA: ACM. https://doi.org/10.1145/2851581.2890254.

Wang, Xin, Man Jiang, Zuowan Zhou, Jihua Gou, and David Hui. 2017. "3D Printing of Polymer Matrix Composites: A Review and Prospective." *Composites Part B: Engineering* 110 (February): 442–58. https://doi.org/10.1016/j.compositesb.2016.11.034.

Weng, Zixiang, Jianlei Wang, T. Senthil, and Lixin Wu. 2016. "Mechanical and Thermal Properties of ABS/Montmorillonite Nanocomposites for Fused Deposition Modeling 3D Printing." *Materials & Design* 102 (July): 276–83. https://doi.org/10.1016/j.matdes.2016.04.045.

Wi, D., A. Sodemann, and R. Chicci. 2017. "Vibratory Haptic Feedback Assistive Device for Visually-Impaired Drivers." In *2017 IEEE SmartWorld, Ubiquitous Intelligence Computing, Advanced Trusted Computed, Scalable Computing Communications, Cloud Big Data Computing, Internet of People and Smart City Innovation (SmartWorld/SCALCOM/UIC/ATC/CBDCom/IOP/SCI)*, 1–5. https://doi.org/10.1109/UIC-ATC.2017.8397593.

Wi, Daehan, and Angela Sodemann. 2018. "Vibration Analysis for the Development of Resonant Microbeam High-Resolution Vibrotactile Haptic Display." *Journal of Vibration and Control*, May, 107754631877867. https://doi.org/10.1177/1077546318778672.

Xu, Cheng, Ali Israr, Ivan Poupyrev, Olivier Bau, and Chris Harrison. 2011. "Tactile Display for the Visually Impaired Using TeslaTouch." In *CHI'11 Extended Abstracts on Human Factors in Computing Systems*, 317–322. ACM. http://dl.acm.org/citation.cfm?id=1979705.

APPENDIX A

ALL DATAS OF PLASTIC PROTOTYPES

1. Description of Plastic Material Prototypes

For the 1st prototype, PLA material and Lulzbot 3D printer are used. A total of 20 beams are made in a circular pattern on a base of 2mm thickness. All beams are designed to have a square cross section with 1mm on each side. The longest beam is 20 mm, and each subsequent beam is 0.2mm shorter. The angle between each beam in the circular pattern is 18 degrees. There is a hole at the center of the base to locate a speaker below the base. The distance between a beam and the hole is 1mm. The cross-sectional shape of manufactured beams exhibits poor squareness, and the surfaces of beams are not clear and uniform. This is because FDM 3D printing is an additive method, which melted plastic material is squeezed from the nozzle to pile up in layers to build the designed model. In FDM, it is possible to manufacture only beam lengths that are an integer multiple of the layer height and only cross-sectional areas with a diameter that is within the X/Y positioning resolution of the machine. On the surface of the printed 1st prototype, there are many surplus materials like 'strings', which are connected between each beam. It seems to need a better setup for Lulzbot 3D printer to obtain more accurate model without the surplus material.

For the 2nd prototype, the same conditions used for the 1st prototypes are used. Only differences are that the thickness of the beam base is 1mm, and the distance between a beam and the hole at the center is 10mm. This difference in the thickness of the base can be used to find the beam vibration difference depending on the beam base thickness. The 2nd prototype also has unclear surface of beams and many strings between each beam.

For the 3rd prototype, ABS material and Objet 3D printer are used. A total 100 beams are made in 5 circular patterns on a base of 1mm thickness. There are 20 beams on each circular pattern. All beams are designed to have a square cross section. The width and height of all beams on an innermost circular pattern is 1mm, and the beams on each subsequent circular pattern have 0.1mm larger width and height; The width and height of beams on the 2nd circular pattern is 1.1mm, and the width and height of beams in the 3rd is 1.2mm, and the width and height in the 4th is 1.3mm, and the width and height in the 5th is 1.4mm. The longest beam in a circular pattern is 20mm, and each subsequent beam in the same circular pattern is 0.2mm shorter. The distance between a beam on the innermost circular pattern and the hole at the center is 1mm, and the distance between beams on each subsequent circular pattern is also 1mm. The operating principle of Objet 3D printer differs from Lulzbot 3D printer previously used. They are in same FDM, but the Object 3D printer surrounds the targeted model with a kind of soft resin material. In my research, beams are surrounded in the soft material. It must be removed by water jet, which water pressure is adjustable. However, since the beams are very thin and long, even the water jet with the lowest water pressure destroys the beam array.

For the 4th prototype, the same model as the 3rd prototype are made with a different 3D printer, Fortus 3D printer. The material used with Fortus 3D printer is ABS material. This time the model is made successfully, but the actual dimensions of beams are thicker than other prototypes made of PLA material. This is because the material properties of PLA material such as elastic modulus and mass density are higher than those of ABS material, which makes ABS to be a softer material than PLA. A model made of a softer material can have more inaccurate dimensions because FDM is an additional method where the molten material is squeezed and layered. The cross-sectional

shape of beams also exhibits poor squareness.

For the 5th prototype, form 1+ 3D printer and its material, Photopolymer Resin, are used. This printer has better accuracy in manufacture than the 3D printers previously used like the Lulzbot. The Form 1+ 3D printer works in a different way compared to the Lulzbot. Most 3D printers like Lulzbot are of the FDM variety, which melted plastic is slowly squirted through a nozzle in layers to build up a print. The Form 1+, however, is an SLA model, which uses a liquid resin material which solidifies under exposure to lasers light. The build platform, where the print is built, is upside down and dips into a fluid status of resin below. Then, lasers are used to harden a layer of resin to the correct outline. The platform raises a fraction for the next layer to be hardened, and it keeps maintaining until the complete model is printed. The print keeps rising very slowly wholly from the resin tank with bunch of branches, which holds the print. After manufacture, the print should be fully dipped into a sealable tub filled with isopropyl alcohol and leaved for a while until alcohol washes extra resin off. This washing process is repeated few times to improve the quality of the print. After then, any remained support structures should be removed by snips and tweezers.

For the 5th prototypes, a total of 143 beams are attempted in a 13 x 11 rectangular pattern on a 1mm thick base. All beams are designed to have a rectangular cross section. The rectangular pattern has rows that are all the same length and varying cross-sectional area and has columns that are all the same cross-sectional are with varying length. The first beam has 0.7mm side length and each subsequent beam is 0.04mm larger in each row. The longest beam is 40mm, and each subsequent beam is as shorter as 15 degree in each row. The distance between the beams in the first row and the side of beam base is 2.2mm, and the distance between each beam is 5.42mm. Since resin is a fluid status material and doesn't have elastic modulus, ABS material property is used to calculate the resonant frequency according to Dr. Hsu's advice, whose research area is 3D printer. Due to the operating principle of form 1+ 3D printer, which makes the bottom part and branches to hold the print, the initial angle for making the print is set as close as 0 degree so that those supporting part would not be generated. However, the half of beam base is made, and another half is completely failed, as shown in Table 4. Some beams are also detached or broken from the beam array when washing them in a sealable tub filled with isopropyl alcohol since they are thin and long. Even the beams made successfully do not have good quality.

For the 6th prototype, Objet 24 3D printer and its material, VeroWhitePlus (RGD835), are used. This Object 3D printer works in the FDM way, and there are 2 type of material options; which are glossy and matte. The printing method for glossy type is as similar as the Lulzbot 3D printer previously used, which molten plastic is squirted through a nozzle in layers to build up a print. The printing method for matte type is as similar as the Object 3D printer, which a support material wraps the print around, and it should be removed by water jet. 2 type options are both tried to make 2 models having different beam dimension and number of beams. For the 1st model, there are total 100 beams having rectangle cross section in 5 circular patterns on a 1 mm thick base. All beams in an innermost ring have 0.92mm side length, and each subsequent beam is 0.02mm larger. Longest beam is 23.8mm, and each subsequent beam is 0.2mm shorter. The distance between beams and the hole at the center is 1mm. The distance between each beam in an innermost circular pattern is 2.1 mm, and the distance in each

subsequent circle is 0.2mm larger. For the 2nd model, there are 5 x 3 beams in a rectangular pattern on a 1 mm thick base. Every beam is designed to have rectangular shape and same resonant frequency. The smallest beam has 0.31mm thickness and 11.14mm length, and the largest beam has 1.55mm thickness and 24.9mm length. The distance between the beams in the first column and the circle at the center is 2mm. The distance between each beam in each row and column is 2mm. Both 2 models are designed based on the calculation considering printer specification and the aspect ratio of beam length to thickness. The models are manufactured successfully in both glossy and matte type. The matte type, however, has a support material surrounding the model, and the model is broken when washing it due to high water pressure as same as prototype 3.

For the 7th prototype, a total of 143 beams of PLA, 13 x 11 beams, are made in a rectangular pattern on a 1mm thick base. The rectangular shape is selected for the beam base this time. Since the speaker used for the experiment has circular shape, it is tried to know if the beams located out of the range of the speaker could be excited. The pattern has rows that are all the same length and varying cross-sectional area and has columns that are all the same cross-sectional area with varying length. The side length of the first beam is 1 mm, and each subsequent beam is 0.1mm larger in each row. The longest beam is 20mm, and each subsequent beam is 0.2mm shorter. The distance between the first beam in the first row and the side surface of the beam base is 2.2mm. The distance between each beam is the same as the sum up of the thickest beam dimension in the first row and the thickest beam dimension in the next row. After manufacturing, it is found that every beam dimension of the model printed is thicker than the designed dimensions.

For the 8th prototype, the same material and 3D printer as the 6th prototype are used. This time the specification of the printers and the ratio of beam length and thickness are considered to improve manufacturing. Base on the test result of the 6th prototype, the 45 degrees of initial angle is also considered to successfully print the model. A total of 15 beams, 5 x 3 beams, are made in a rectangular pattern, on 1 mm thick base. Every beam is designed to have a rectangular shape and has same resonant frequency. The smallest beam has 0.31mm thickness and 11.14mm length. The largest beam has 1.55mm thickness and 24.9mm length. The distance between the beams in the first column and the hole at the center is 2mm, and distance between each beam in each row and column is 2mm. However, the beams in the first column, which are smallest beams, are not made at all, and other beams made successfully have a relatively thin thickness or were bent. Despite of consideration of the specification of the printer, the beam array is not made successfully. It seems this printer is not good option to make the model having thin and long dimensions.

For the 9th prototype, every set up is same as the one for the 7th prototype. Only difference is that this model has tilted beams. Since a finger touch to the beam tip could hinder beam vibration, the tilted beams are considered for beam vibration model so that the finger will not force the beam tips directly and stop the beam vibration. The distance between the beam in the first column and the hole at the center is 11.482mm. The angle between beams and the base of beam array is 60 degrees. Similar to the result of 7th prototype, some beams are not made at all, and some are bent. The beam base is even broken.

For the 10th prototype, the final PLA prototype, a 10 x10 array of vibratory beams is designed using the damping ratio calculated in impulse response test in the

Chapter 5, Vibration Experimentation. A set of beam dimensions which satisfies the five requirements that is discussed in the Chapter 4, Manufacturing and prototyping, is estimated. The beam array consists of beams between 1mm and 1.4mm in diameter, at 0.1mm increments, and lengths between 20mm and 25mm, in 0.1mm increments, as shown in Table 4.

2. Description of the Experiment Result with Plastic Material Prototypes

With the 1st prototype of PLA, it is found that some beams vibrate at certain frequencies, which shows the resonant microbeam vibrotactile array works. However, the amplitude of the beam vibration is small, and other beams do not vibrate at any frequency.

With the 2nd prototype of PLA, most beams vibrate at certain frequencies, and the beam vibration moves along beams when the frequency of oscilloscope is changed. This proves the concept using resonant microbeam. However, there are still some improvement points. Only first few longest beams' amplitude is big, and it is hard to see the one of other shortest beams with the eye. To increase the amplitude of beam vibration, it should be needed to consider various beam design parameters such as damping ratio and quality factor. Diverse materials for several 3D printers also should be investigated to manufacture the better and more accurate model having clearer and uniform surfaces. Another improvement is that it is hard to perceive beam vibration when a finger touches the tip of the beams, but it is easier to perceive it when touching the side surface of the beams. Considering that all beams should be contacted at the same time to perceive beam vibrations that describe a real image, the contact point should be beam tips. The most sensitive body part are fingertip and palm in order, and the palm would be the best place for my research considering an enough space for the contact area. For this reason, figuring out the method to make people perceive beam vibration via touching to beam tips would be very important part in the research.

With the 4th prototype of PLA, vibration is observed in only 2 longest beams in the 5th circular pattern, and no beam vibration is not observed with the eye.

With the 9th prototype of PLA, it is found that no beam vibration is observed at their resonant frequency.

With the 5th prototype of PLA, only one beam vibration, which are located inside of the speaker range, is observed with the eye. The beams on the edge of the beam base, which are located on the area of outside speaker, do not vibrate at all.

No experiment with other prototypes is conducted since they are failed to manufacture.

APPENDIX B

ALL FORCED RESPONSES OF THE 2ND METAL BEAM

WITH SILICONE RUBBER BEAMS

In Experiment 18, to investigate the relationship between silicon rubbers and metal beams, a total of 46 cases with the silicone rubber beam length changes are investigated, and more than 500 times of a high-speed camera experiment are recorded for every case in order to find the relationship between silicon rubbers and beams. These experiments are divided by 3 experiment set. The silicone rubber beams are cut manually with some increments. 5 silicone rubber beams are attached to the first thinnest 5 metal beam tips, and the frequency response of the only 2nd metal beam is recorded and analyzed.
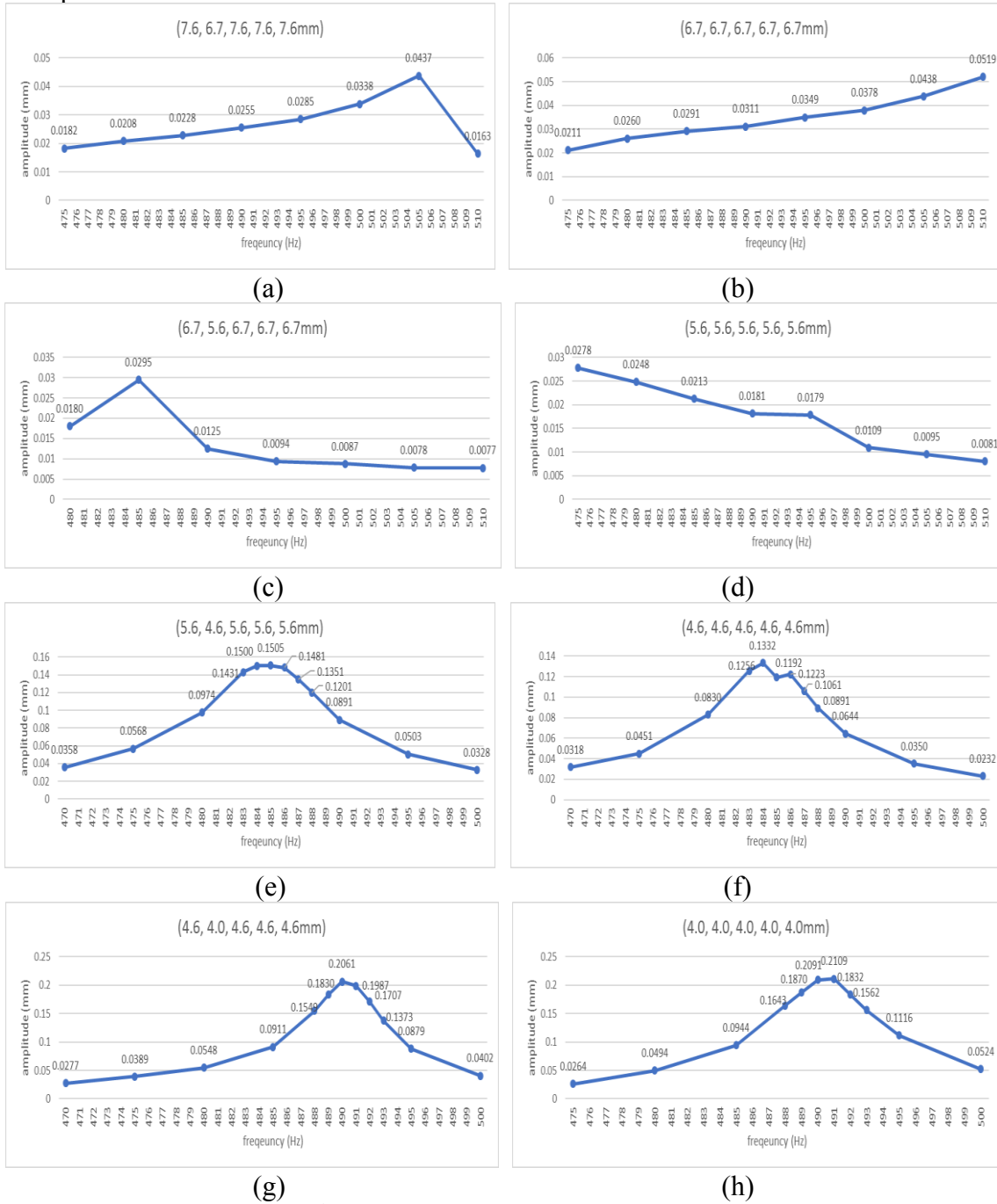
1. Experiment Set 1

(a)

(b)

(c)

(d)

(e)

(f)
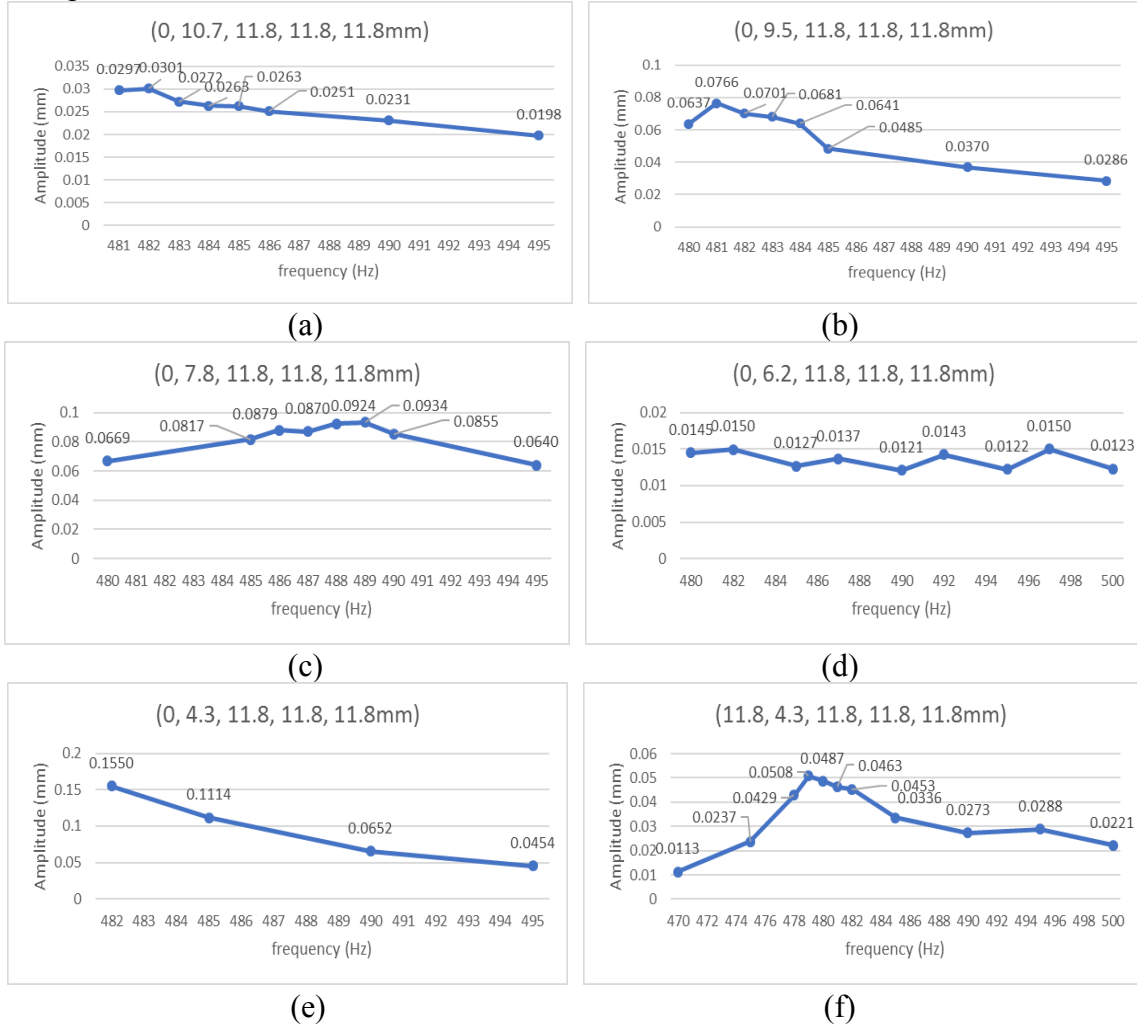
Fig. 78. Amplitude of the 2nd metal beam when the five rubber beams have the lengths: (a) (0, 10.7, 11.8, 11.8, 11.8mm). (b) (0, 9.5, 11.8, 11.8, 11.8mm). (c) (0, 7.8, 11.8, 11.8, 11.8mm). (d) (0, 6.2, 11.8, 11.8, 11.8mm). (e) (0, 4.3, 11.8, 11.8, 11.8mm). (f) (11.8, 4.3, 11.8, 11.8, 11.8mm).
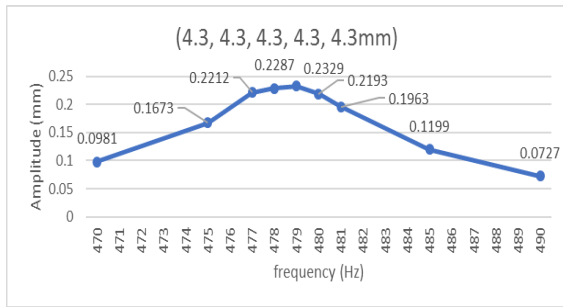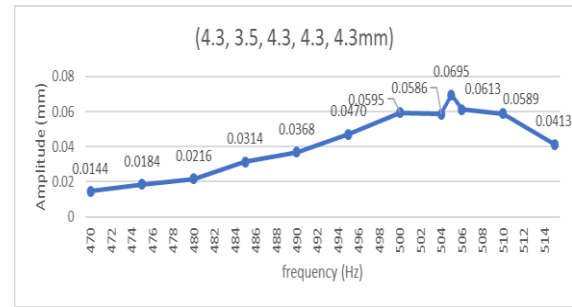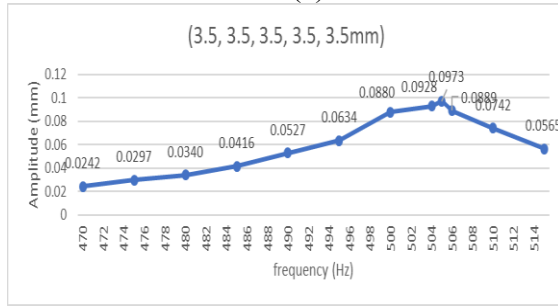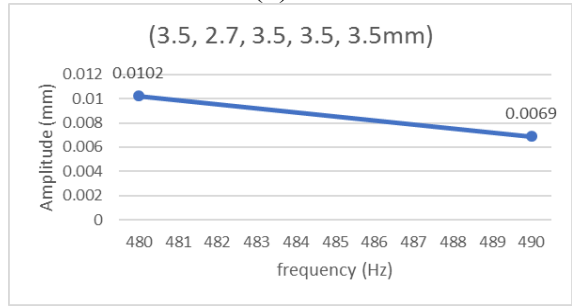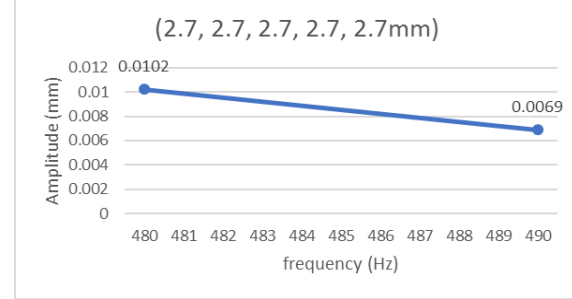
Fig. 79. Amplitude of the 2nd metal beam when the five rubber beams have the lengths:
(a) (4.3, 4.3, 4.3, 4.3, 4.3mm). (b) (4.3, 3.5, 4.3, 4.3, 4.3mm). (c) (3.5, 3.5, 3.5, 3.5,
3.5mm). (d) (3.5, 2.7, 3.5, 3.5, 3.5mm). (e) (2.7, 2.7, 2.7, 2.7, 2.7mm).

2. Experiment Set 2
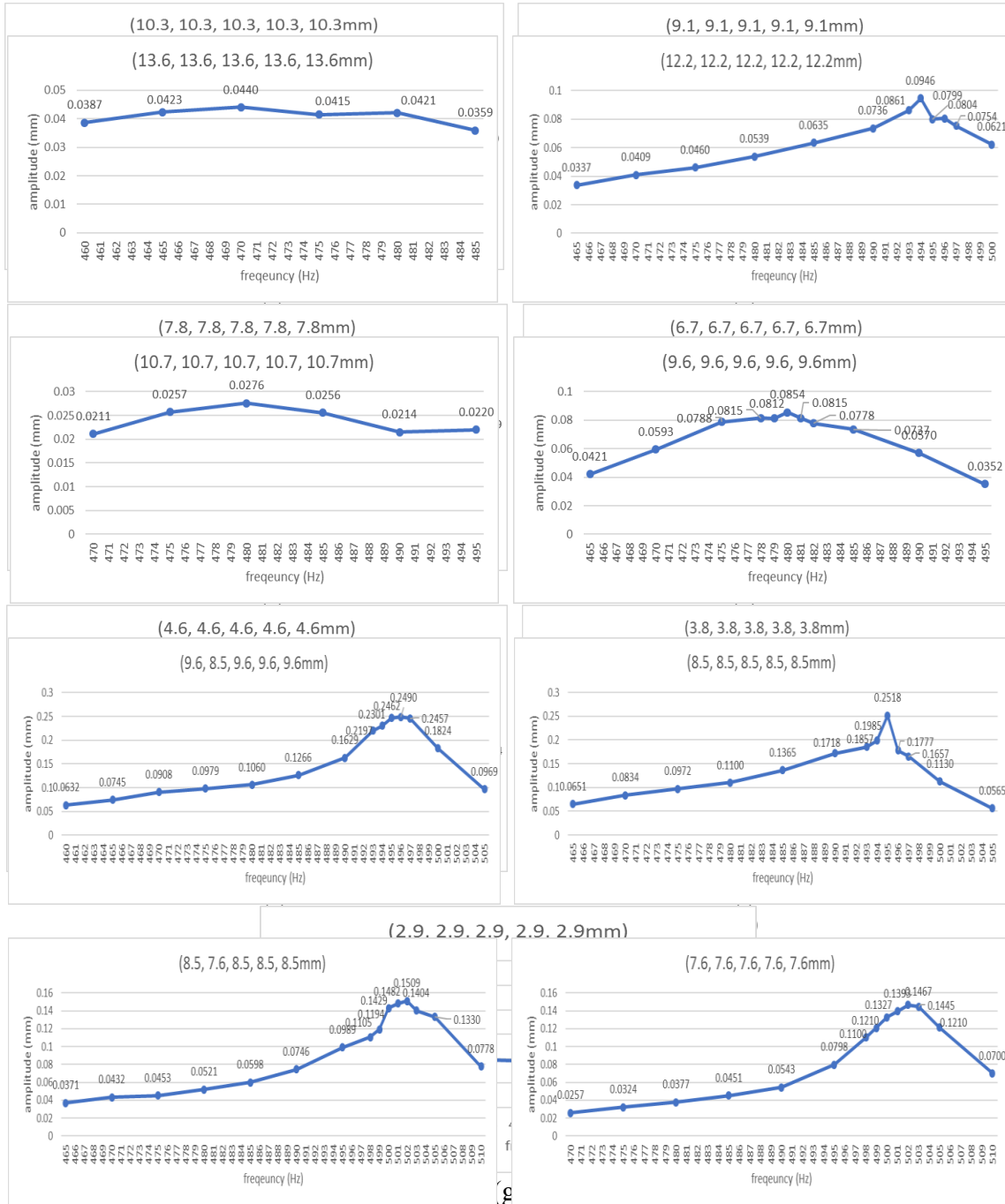
Fig. 80. Amplitude of the 2nd metal beam when the five rubber beams have the lengths: (a) (10.3, 10.3, 10.3, 10.3, 10.3mm). (b) (9.1, 9.1, 9.1, 9.1, 9.1mm). (c) (7.8, 7.8, 7.8, 7.8, 7.8mm). (d) (6.7, 6.7, 6.7, 6.7, 6.7mm). (e) (4.6, 4.6, 4.6, 4.6, 4.6mm). (f) (3.8, 3.8, 3.8, 3.8, 3.8mm). (g) (2.9, 2.9, 2.9, 2.9, 2.9mm).

Fig. 81. Amplitude of the 2nd metal beam when the five rubber beams have the lengths: (a) (13.6, 13.6, 13.6, 13.6, 13.6mm). (b) (12.2, 12.2, 12.2, 12.2, 12.2mm). (c) (10.7, 10.7, 10.7, 10.7, 10.7mm). (d) (9.6, 9.6, 9.6, 9.6, 9.6mm). (e) (9.6, 8.5, 9.6, 9.6, 9.6mm). (f) (8.5, 8.5, 8.5, 8.5, 8.5mm). (g) (8.5, 7.6, 8.5, 8.5, 8.5mm). (h) (7.6, 7.6, 7.6, 7.6, 7.6mm).

1 7 9

2. Experiment Set 3

(a)

(b)

(c)

(d)

(e)

(f)

(g)

(h)

Fig. 82. Amplitude of the 2nd metal beam when the five rubber beams have the lengths: (a) (7.6, 6.7, 7.6, 7.6, 7.6mm). (b) (6.7, 6.7, 6.7, 6.7, 6.7mm). (c) (6.7, 5.6, 6.7, 6.7, 6.7mm). (d) (5.6, 5.6, 5.6, 5.6, 5.6mm). (e) (5.6, 4.6, 5.6, 5.6, 5.6mm). (f) (4.6, 4.6, 4.6, 4.6, 4.6mm). (g) (4.6, 4.0, 4.6, 4.6, 4.6mm). (h) (4.0, 4.0, 4.0, 4.0, 4.0mm).
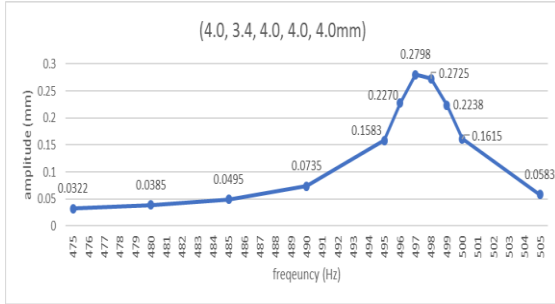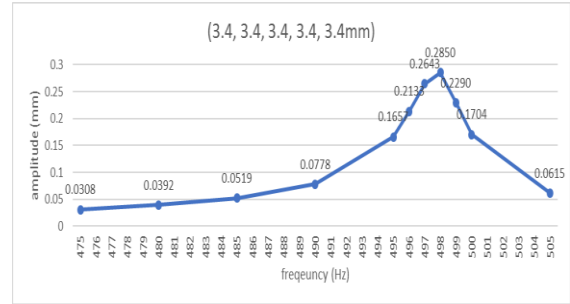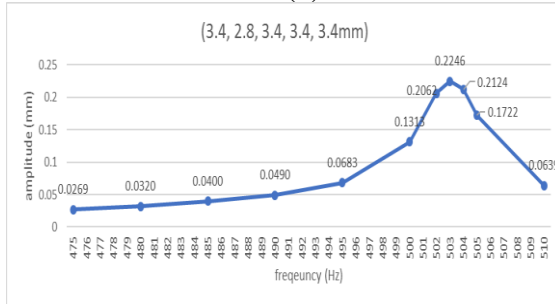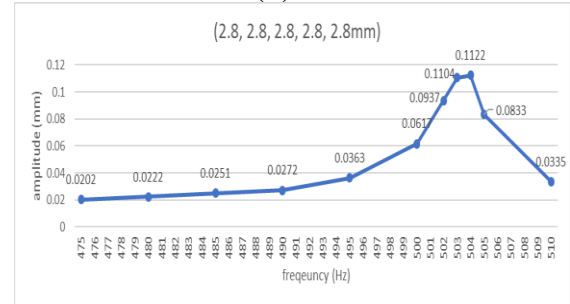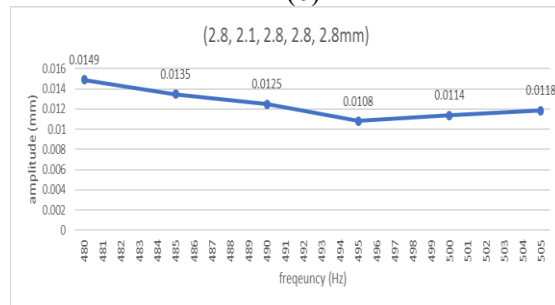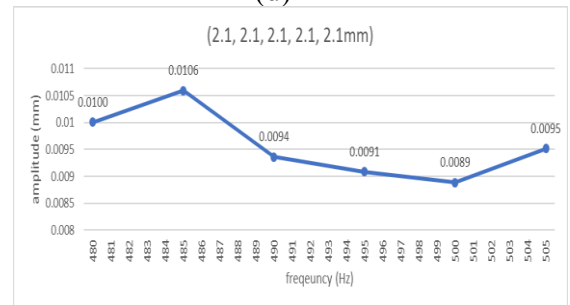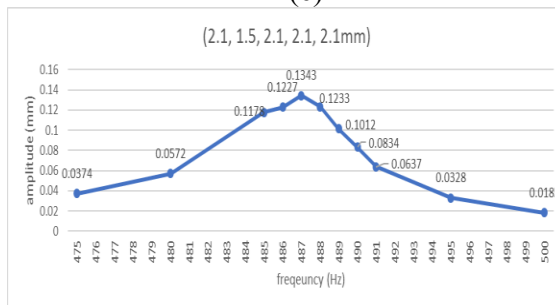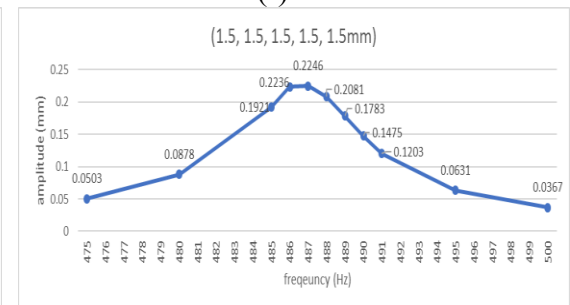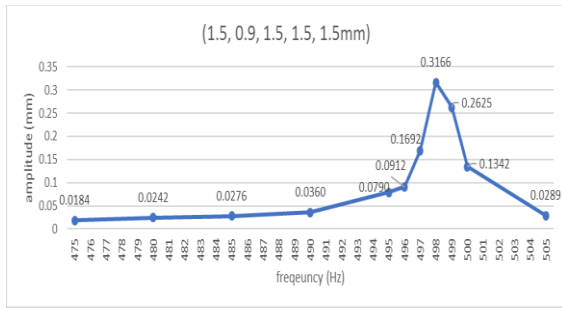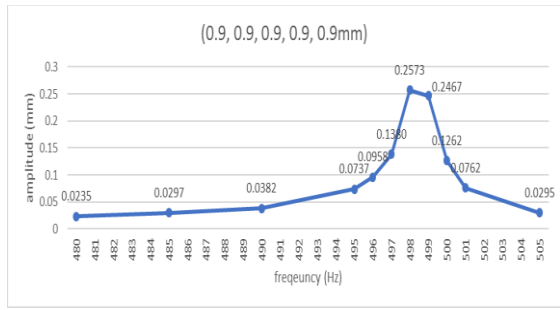
Fig. 83. Amplitude of the 2nd metal beam when the five rubber beams have the lengths:
(a) (4.0, 3.4, 4.0, 4.0, 4.0mm). (b) (3.4, 3.4, 3.4, 3.4, 3.4mm). (c) (3.4, 2.8, 3.4, 3.4,
3.4mm). (d) (2.8, 2.8, 2.8, 2.8, 2.8mm). (e) (2.8, 2.1, 2.8, 2.8, 2.8mm). (f) (2.1, 2.1, 2.1,
2.1, 2.1mm). (g) (2.1, 1.5, 2.1, 2.1, 2.1mm). (h) (1.5, 1.5, 1.5, 1.5, 1.5mm).

Fig. 84. Amplitude of the 2nd metal beam when the five rubber beams have the lengths: (a) (1.5, 0.9, 1.5, 1.5, 1.5m). (b) (0.9, 0.9, 0.9, 0.9, 0.9mm).